Title

Microvascular Hydrodynamics: Structure and Adaptation Principles

Author

QI, YUJIA

Publication Date

2022

Peer reviewed|Thesis/dissertation

UNIVERSITY OF CALIFORNIA

Los Angeles

Microvascular Hydrodynamics: Structure and Adaptation Principles

A dissertation submitted in partial satisfaction

of the requirements for the degree

Degree of Philosophy in Mechanical Engineering

by

Yujia Qi

2022

ABSTRACT OF THE DISSERTATION

Microvascular Hydrodynamics: Structure and Adaptation Principles

by

Yujia Qi
Degree of Philosophy in Mechanical Engineering
University of California, Los Angeles, 2022
Professor Marcus Roper, Co-Chair
Professor Andrea Bertozzi, Co-Chair

Microvasculature structures vary drastically from species to species, and from organs to organs. Different structures signify inclinations of distinct blood flow perfusion features: uniform, or localized? Robust, or efficient? Like the vertebrate tissues having preferred types of vasculature systems that emphasize different traits, in the course of my research, I chose two contrasting systems to be studied by virtue of their specific features: mammalian cerebral cortex microvasculature, and zebrafish embryo trunk microvasculature. For mammalian cerebral microvasculature, considering the distinguished hierarchical construction, and the complex, dense nature of the capillary bed perfusing brain tissue, a model that abstracts the structure while revealing the relationship of blood perfusion and network properties would be extremely helpful; in contrast, zebrafish embryo trunk microvasculature is by itself a simple structure, but being an embryo, its hemodynamic features still undergo developments, and the network would adapt accordingly, which provides an excellent model to study microvascular network adaptation.

Specifically, in different mammalian cortices, I found that the dense, parallel penetrating

vessels perfusing cerebral cortex – arterioles and venules, are consistently in imbalanced ratios. Whether and how arteriole-venule arrangement and ratio affect the efficiency of energy delivery to the cortex has never been asked before. I show by mathematical modeling and analysis of the mapped mouse sensory cortex that the perfusive efficiency of the network is predicted to be limited by low flow regions produced between pairs of arterioles or pairs of venules. Increasing either arteriole or venule density decreases the size of these low flow regions but increases their number, setting an optimal ratio between arterioles and venules that matches closely that observed across mammalian cortical vasculature. Low flow regions are reshaped in complex ways by changes in vascular conductance, creating geometric challenges for matching cortical perfusion with neuronal activity.

Within the zebrafish trunk, tuning of vessel radii ensures red blood cells are delivered at equal rates across tens of microvessels. How do vessels find optimal radii? Vessels are known to adapt their radii to maintain the shear stress from blood flow at the vessel wall at a set point. Yet models of adaptation purely on the basis of average shear stress have not, until now, been able to produce complex loopy networks that resemble real microvascular systems. The shear stress on real vessel endothelia peaks sharply when a red blood cell passes through the vessel. I show that if vessel shear stress set points are cued to the stress peaks, then stable shear-stress-based adaptation is possible. Model networks that respond to peak stresses alone can quantitatively reproduce the observed zebrafish trunk microvasculature, including its adaptive trajectory when hematocrit changes. My work reveals the potential for mechanotransduction alone to generate stable hydraulically tuned microvascular networks.

When parts of the zebrafish network – the anastomoses in the distant trunk that connects the artery and the vein directly – are amputated, a localization of blood flow at the zebrafish tail is observed in my adaptation model, which is verified through experiments. This discovery highlights a specific structure's function, which can only be identified under network adaptation, and shows the significance of taking adaptation into account when evaluating a vascular structure's hemodynamic functions.

The dissertation of Yujia Qi is approved.

Lihua Jin

Jeff D. Eldredge

Andrea Bertozzi, Committee Co-Chair

Marcus Roper, Committee Co-Chair

University of California, Los Angeles

2022

TABLE OF CONTENTS

1 Introduction **1**

1.1 Microvasculature Systems 1

1.2 Structure and Adaptation 2

1.2.1 Case Study: Mammalian Cerebral 3

1.2.2 Case Study: Zebrafish Trunk 5

2 Microvascular Structure in Cortex: Arterial-Venule Ratio Determines Cerebral Blood Flow Perfusion Efficiency **8**

2.1 Methodology 9

2.1.1 Observations of Low Flow Capillaries 10

2.1.2 Green's Function Method 15

2.1.3 Numerical Convergence Study 20

2.1.4 Modeling Vessel Arrangements 25

2.2 Results 26

2.2.1 Adding Arterioles Does Not Increase Tissue Perfusion: An Optimal Ratio of Arteriole-Venule Quantities 30

2.2.2 Penetrating Vessel Conductances Do Not Directly Control Perfusion . 34

2.3 Discussion 39

3 Microvascular Adaptation in Zebrafish Trunk: Hemodynamic-Regulation Allows Stable Growth of Microvascular Networks **48**

3.1 Methodology 50

3.1.1 Observations: Real Intersegmental Red Blood Cell Fluxes Are Uniform From Head to Tail 50
3.1.2 A Stable Peak Shear Stress Set Point Model 51
3.2 Results 60
3.2.1 PSS-activation Model Can Stably Adapts Realistic Networks 60
3.2.2 PSS-activation Model Creates Uniform Red Blood Cell Flux in Zebrafish Trunk 63
3.2.3 Uniform Perfusion Can Not Be Maintained When Hematocrit Decreases 65
3.2.4 Uniform Perfusion of the Zebrafish Trunk Is Dependent on Arterio-Venous Anastomoses 66
3.3 Discussion 71

4 Summary and Significance 75

References 79

LIST OF FIGURES

1.1 The hierarchical system of a real mouse brain vasculature. The color indicates the predicted pressure distribution. 4

1.2 The primary blood vessels of the vertebrate embryo [1]. 6

1.3 The trunk and tail of the zebrafish are perfused by a ladder-like network of microvessels, with inflow along the dorsal aorta (DA) and outflow along the posterior cardinal vein (PCV), along with rung-like system intersegmental arteries (SeAs) and veins (SeVs) linking the two vessels. (A) Composite angiogram of the trunk vessels in a 4 dpf embryo produced from images in the Zebrafish vascular atlas [2]. (B) Simplified wiring diagram of a section of the trunk. (C) DA and PCV are directly connected at the tail 7

2.1 Exemplary continuum model where penetrating vessels are treated as lines of sources and sinks, and the capillary bed is treated as porous media. Left: Arrangements of straight penetrating arterioles and venules in the model. Right: Schematic of coupling between penetrating vessels and porous medium - source strength on a penetrating vessel is matched to flux decreases along the vessel. . 9

2.2 Left: The low flow capillaries (vessels with less than 40% of median flux) at depth $z = 300\mu m$ of the mouse cortical vasculature shown in fig:problemA. Right panels: vessel geometry (upper) and flux histogram (lower) in the slice of mouse cortical vasculature. Fluxes are normalized so median = 1. 11

2.3 A synthetic network constructed using the method in [3], but with idealized straight penetrating arterioles and venules. Color indicates pressure from high (red) to low (blue). 12

2.4 Low flow capillaries (vessels with less than 40% of median flux) at depth $z = 300\mu m$ in a synthetic network built to model Fig. 2.2 with same penetrating vessel locations. Black dots: venules, red dots: arterioles. Same annotations are used in Fig. 2.13B as well. 13

2.5 In real and synthetic networks, low flow regions are 2 times less likely to be found near arterioles than would be expected by chance. Blue bar and red bar respectively show the portion of all capillaries or low-flow capillaries that are topologically closer to an arteriole than a venule. 14

2.6 Histogram of the portion of low flow capillaries closer to an arteriole to the portion of capillaries closer to an arteriole. In synthetic networks based on the mouse sensory cortex, low flow capillaries cluster near venules. 15

2.7 Schematic plot of the validation problem. A cubic box has a side length of 50, the penetrating vessels have length 20, and they are located in the middle of the depth. 21

2.8 Grid independence study. Red and blue lines represent the percentage differences between computations at grid sizes 20, 30, 40, ... as the grid along penetrating vessels increases (red), and as the number of Fourier modes is increased (blue). Convergence results support using N=100 source/sink points per vessel, and Nx= Ny =100 Fourier modes. 22

2.9 Comparison of pressures evaluated along y = 25 and y = 20 lines on the z = 21 plane between continuum (dots) and a regular cubic network (solid line) model shows excellent agreement between the two models, even at the penetrating vessels. Inset figure shows the pressure contour in the z = 21 plane. 23

2.10 The relative L2 error of pressure along the line y = 24, z = 21 in the continuum model compared to the pressure of isotropic random networks generated by Delaunay triangulation. In the inset figures, lines represent the pressure along the line from the continuum model; dots represent the network model's pressure. Decay in relative error appears algebraic. Importantly, with 20000 branch points in the random network, relative error is around 6%, and continuum pressure is close to identical to the network model (left inset). 24

2.11 The entropy of the arrangement of penetrating vessels in the real microvasculature is compared to a random distribution and two ordered distributions. 26

2.12 Entropy in different scales. The entropy of real penetrating vessels is consistent with their arrangements being random rather than ordered. 27

2.13 A continuum model predicts the same patterns of low flow regions as synthetic discrete networks, and reveals effects of arteriole-venule arrangements on the effectiveness of perfusion. A. Low flow regions (regions with less than 40% of median flux) on midplane are shown in blue for a random distribution of penetrating vessels with a 2-1 arteriole-venule ratio and show a large continuous poorly perfused area surrounded by arterioles. B. Predicted low flow regions match closely to a synthetic discrete and hierarchical network model, with the same penetrating vessel placements (shown in blue: capillaries in midplane carrying less than 40% of the median flux) C. Total low flow area ratio (x-axis) in continuum model predicts the total volume fraction of low perfused capillaries (y-axis) in a hierarchical discrete network model with same vessel arrangements. Each point represents a different random arteriole and venule arrangement. D. The depth in the modeled tissue where low flow regions are calculated affects the total low flow area but only weakly affects comparisons between different arrangements. Red curve: arrangement A, blue curve: arrangement E. Inset figures show how the low flow areas in arrangement A change with depth. E-F: effect of vessel arrangement. E: (Ordered) honeycomb arrangement of arterioles and venules with the same 2-1 arteriole-venule ratio as A. Low flow regions are more numerous but smaller. F. The histogram of fluxes for random (A) and ordered (E) arrangements of vessels. 28

2.14 Venules are arranged on a uniform square grid, and arterioles are added randomly one-by-one at sites marked with red dots. Blue regions show low flow after all red sites have been filled. 30

2.15 Fraction of tissue with low perfusion, for varying arteriole-venule ratio. Arrows show measured most numerous-least numerous penetrating vessel ratios for humans [4], Rhesus monkeys [5, 6], Sprague Dawley rats [7] and C57/BL6 male mice [8]. For primate brains, arterioles are more numerous, so the reported ratio is arterioles/venules; for rodent brains, venules are more numerous, and venule/arteriole ratio is reported. 31

2.16 Change of mean perfusion with the arteriole-venule ratio when the arterioles are set on the grid randomly one-by-one to vary arteriole-venule ratio. 32

2.17 Optimal arteriole-venule ratio is not sensitive to where the thresholds are set. . . 33

2.18 Optimal arrangements of vessels (top right panel) can produce perfusion uniformity that does not decrease as more arterioles are added. To construct an optimal network, arterioles are added sequentially by a greedy method, placing them at grid points with the lowest flow. Optimally arranged arterioles do not create large low flow regions (right) compared with non-optimized networks (left). C. Mean fluxes are larger for optimally arranged vessels (blue) than for non-optimal configurations (orange) but still saturate with limitingly large arteriole-venule ratios. D. Optimal arrangements (blue) of vessels produce perfusion uniformities that saturate as arteriole venule ratio is increased, unlike random configurations (orange). 35

2.19 The predicted distribution of mean flux on $z = 300\mu m$ plane when the conductance of a penetrating vessel (red; arteriole, blue; venule) is either increased ten-fold or sent to 0. Horizontal lines represent the mean flux before any change. 42

2.20 In real mouse vasculature, regulating arteriole conductances more precisely controls blood flow in capillaries than regulating venule conductances. 43

2.21 In a continuum model with more arterioles than venules, changes in arteriole conductance, but not changes in venule conductance, have unintuitive effects upon perfusion. A, B. Effect of blocking or increasing conductances of arterioles 19 or 16 (the numbering of arterioles follows Fig. 2.13A). Left panels: Colored regions represent areas where flow increased (yellow) or decreased (cyan) by more than 10%. Right panels: Low flow spots after conductance change (blue regions). C. The mean flux distribution after increasing the conductance of individual arterioles five-fold or block them individually. The blue horizontal line represents the mean flux before any conductance change. Mean flux is calculated on the midplane. D. Fraction of tissue in mid-plane that is well-perfused (greater than 40% of median flow) when arteriole conductances are individually increased five-fold or arterioles are blocked. The blue horizontal line represents the ratio of well-perfused area before any conductance change. 44

2.22 Exchanging arterioles and venules in Fig. 2.13A, and redoing the analysis from Fig. 2.21, it can be seen that their roles in setting low flow areas are reversed. A. Low flow regions before changing penetrating vessel conductances. B. The low flow area after dilating venule 16. C. The low flow area after blocking venule 16. D. The low flow area after blocking venule 19. Compare A, B, C, D to Fig. 2.13A, 2.21A2, 2.21B2, 2.21B1; the low flow areas in the corresponding figures are the same. 45

2.23 Two more examples of low flow areas and their regulation response. Arrangements of vessels do not affect conclusions about the different controllability of perfusion by arterioles versus venules. Shown: two different random arrangements of penetrating vessels with the same arteriole-venule ratio as Fig. 2.13A. For each arrangement, left panels show the low flow area before changing arteriole conductance, and right panels show the mean flux change after dilating or blocking one of all arterioles. Blue line shows the mean flux before any change. Note that for both arrangements, and just as in Fig. 2.21C, increasing some arteriole conductances decreases perfusion, while blocking many arterioles increases perfusion. 46

2.24 Counterpart to Fig. 2.21C, showing the effect of total inflow into the tissue (normalized by the baseline inflow) when arterioles are individually dilated or blocked. Previously, the L2-norm of q was used to quantify total perfusion through the tissue, before and after vessel conductances are perturbed. Similar results (i.e., unintuitive changes in flow) are obtained when instead plotting the effect of arteriole conductance change upon the total flow into the tissue through all penetrating arterioles. 47

3.1 In (A) RBC fluxes (normalized so that the median flux per vessel is 1) over distal, rostral, and mid-trunk SeAs among $N = 12$ 4 dpf individuals are plotted. Each data point is pooled from 4 SeAs, taken from blue: distal (tail), red: rostral (head), and yellow: mid-trunks. Although flows are variable, no region of the trunk receives consistently greater flows. (B) Pooling data from all fish, show no differences in fluxes between the three trunk regions. In comparison, a simulated model of the fish in which all SeAs are assigned the same radius (purple dots) would have monotonically decreasing RBC flux from head to tail, due to the pressure gradient in the DA. (C) Flow uniformity requires tuning of vessel radii. I took the constant (red boxes) and optimal fish radii (green boxes, calculated using the adaptation model, see Methodology), and perturbed the modeled radii of vessels by different percentages (10, 20, and 30 percent from left to right), measuring the head to tail ratio. Data shown comes from 100 replicates at each level of perturbation. The observed uniformity in real 4dpf fish (blue box) is found to be consistent with vessel radii being within 30% of their optimum. . . . 52

3.2 RBCs deform squeeze through vessel, dragging on the vessel walls (upper). The red blood cell inside of SeAs is modeled as a cylinder with spherical ends, and with fixed wall gap spacing $h = 0.1\mu m$, dividing the shear stress on the vessel wall into cell free (Poiseuille-profile) and cell touching (Couette-profile) regions (lower). 54

3.3 Shear stresses are measured on a single zebrafish SeA endothelial cell, based on my model of cell-cell hydrodynamics, and on 20s of RBC tracking data. Sharp spikes correspond to passages of a cell (inset shows 1.5s of data), and troughs to cell-free intervals. Only peak shear stresses exceed a typical threshold for shear stress induced cell remodeling (orange line, data taken from [9] 54

3.4 A model includes SeAs, SeVs, and DLAV produces uniform RBC flow in the trunk of the zebrafish. 57

3.5 Uniformization of red blood cell flux can be achieved by PSS model using a wide range of parameter values. 59

3.6 The chosen set of parameters gives a good fit for the vessel conductances with the experimental data. 60

3.7 PSS leads to a consistent decline in endothelial cell activation when vessel radius is increased, whether the inflow to the vessel is pressure or flow controlled (orange curve). By contrast, MSS-cues decrease in the vessel if its radius increases under constant flow (dashed blue), but increases under constant pressure (solid blue). 61

3.8 PSS-activation stabilizes vessel geometries in a single parallel loop network (top panel, schematic). The symmetric equilibrium is a saddle point under mean shear stress adaptation (bottom-left) – the network tends to evolve to a state with one vessel pruned to flow. For activation fraction mode, the symmetric equilibrium is a stable node (bottom-right). 62

3.9 Peak Shear Stress (PSS)-adaptation can robustly adapts a model zebrafish microvascular network with 12 SeAs to achieve uniform RBC flows. (A) Initial RBC fluxes (normalized so that median flux is 1) under 100 sets of random starting radii, with variance consistent with observed variances of vessels, give statistically decreasing RBC flux of SeAs from head to tail. (B) Effect of modeled adaptation in a single fish with random initial radii. Absent Zweifach-Fung effect RBC fluxes are strongly biased toward rostral vessel (orange), though inclusion of Zweifach-Fung effect leads to increased flow in some distal SeAs (red dashed). Evolving vessel radii under Eqn. 3.6, produces highly uniform RBC fluxes across all vessels (blue line). (C) Uniformization of RBC fluxes is due to interplay of radius tuning (blue curve) and the gradient of hematocrit, Ht, in the Dorsal Aorta that feeds each intersegmental vessel. Ht increases with distance along the DA due to plasma skimming by SeAs (orange curves). Insets show the experimental images of red blood cells in two DA segments closer to head or tail. Distal SeAs respond to elevated Ht by growing wider rostral SeAs, compensating for decreasing pressure and uniformizing flows. 64

3.10 RBC fluxes under decreasing overall hematocrit is simulated, starting with an initial hematocrit of $Ht_{\text{inflow}} = 0.12$ (blue circles), and under decreasing $Ht_{\text{inflow}} = 0.11, 0.105, 0.10, 0.095$ (blue-yellow gradient). As hematocrit decreases, RBC fluxes vanish in an increasing number of rostral SeAs. 66

3.11 When hematocrit in DA decreases below a critical threshold of 0.114, adaptation drives vessels to their minimum radii. Plasma skimming keeps Ht above this threshold in the distal DA (solid red) and SeAs (dashed red). Radius adaptation (blue curve) creates a rostral-caudal gradient of radii that realizes uniform flow. 67

3.12 The ratio of RBC fluxes (averaged over 30s) is calculated between the 3 most rostral and 3 most distal SeAs at each of 4-9dpf ($N = 4$ fish for each day). The median head to tail ratio decreases from day 4 to day 7, reaching 0 in 9-10 dpf, consistent with PSS-adaptation (orange line). For the PSS adaptation, the inflow hematocrit is based on date from [10]. 67

3.13 Localization of RBCs in distal vessels is observed in real zebrafish as they age from 4-12 dpf, during which hematocrit decreases 2.1-fold [10]. I superimpose a 30s sequence of phase contrast images (captured at 20fps) of 5 dpf (upper) and a 9 dpf (lower) fish, with mean intensity subtracted to remove the vessel background. RBC fluxes across RBCs are uniform at 5 dpf. At 9 dpf, fluxes are eliminated in rostral SeAs, but remain uniform in a subset of 7 caudal Se vessels. 68

3.14 Given random initial radii (taken from Fig. 3.9B), RBC fluxes (normalized to median is 1) is simulated under adaptation of vessel radii, with and without the DA-PCV anastomosis. If anastomosis is present, adaptation uniformizes flow (compare green and blue curves). Removal of the tail causes a sharp spike in flux in the distal SeA (orange dashed curve), that is increased by adaptation (red solid curve). 70

3.15 Localization of blood flow is seen in a 5dpf transgenic *Tg(fli1:eGFP; Gata1:ds-red)* zebrafish, 1 day post amputation (methods from [11]). GFP-labelled endothelial cells visualize microvessels. DsRed channel data from 60s of images is superimposed, captured at a frame rate of 33fps. Distal SeAs (B) have far greater RBC flux that rostral SeAs (A), due to a 1.87-fold increase in hematocrit. 70

3.16 As the tapering factor (the ratio of conductance between a DA segment and the DA-PCV anastomosis) increases, even though more portion of RBC flux goes into the SeA vessels instead of being shunted by the anastomosis (orange line), the head to tail red blood cell flux ratio would decrease (blue line). The ratio is closest to 1 when the tapering factor is 13. 71

LIST OF TABLES

CHAPTER 1

Introduction

1.1 Microvasculature Systems

The vascular system transports nutrients (such as amino acids and electrolytes), oxygen, carbon dioxide, and hormones between cells. It also plays a role in fighting disease, sustaining body temperature, maintaining the dynamic balance of pH in the body, and many other essential physiological processes. This important network system vital for all vertebrates is constructed with a two-level hierarchy: 1. macrovasculature, which consists of arteries and veins, is responsible for transporting blood from organ to organ for long distance, and 2. microvasculature, which consists of arterioles, venules, and capillaries, takes charge of regulating local blood flow perfusion and blood-tissue communication.

Compared with the macrovasculature systems, which are visible by the human eyes, microvasculature consists of a tremendous amount of minute vessels in order to efficiently perfuse blood through the entire tissue. For example, within a sample of $2mm^3$ in mouse cerebral vasculature (Fig. 1.1), there are over 30000 vessels, with 31 arterioles and 87 venules, the rest being capillaries. Furthermore, the arterioles' radii are below $11\mu m$, venules' radii are under $14\mu m$, while the capillaries' median radius is only $1.5\mu m$. These length scales are far beyond the human eye's ability. Although network systems being this small-scaled and close-packed pose great difficulties to experimentalists, collaborative efforts between physicists, bioengineers, and clinicians have allowed microvascular networks to be mapped with ever-increasing precision in the brain and other organs. In particular, penetrating vessels

(arterioles and venules in cerebral vasculature) have been mapped for regions of the mouse sensory cortex, and the NIH-funded BRAIN initiative promises to generate microvascular of the entire human brain microvasculature. In addition, vascular networks can now be created synthetically by 3D printing, as an important step to synthetic organ-building. Naturally, these experimental measurements take an enormous amount of effort, and they provide timely support to theoretical researches on the microvasculature system, which was considered too complex to be modeled and understood in the past. However, the large quantity of data for microvasculature does not guarantee a fundamental understanding of the network's structural principles, and gaining utility from these new data streams requires the development of tools for making data-fitted models of the microvascular networks, that are robust to the difficulty of measuring conductances or even connecting of finer vessels, and that can be used to understand normal and pathological functions.

My study focused on abstracting models based on the experimental data for mice cerebral circulatory systems, and for zebrafish embryo trunk blood perfusion. These models are not expected to include all physiological details (which is on one hand, impossible, since a number of non-Newtonian features of blood are still not well understood; on the other hand, confusing, if every element is taken into account) but make emphasis on understanding how specific network structures affect blood flow, and how microvascular structure adapts according to hemodynamic cues.

1.2 Structure and Adaptation

The spatial embedding and properties are extremely relevant to the function of distribution systems, which, needless to say, include circulatory systems. Different networks show different architectural features, and there are clear distinctions in how they balance tradeoffs in efficiency and robustness [12]. For mice and rats, the robustness of blood flow to the brain is crucial to the health of brain tissue, and the topology of the microvasculature plays an

important role in supporting such robustness. In mice brain, the characteristic of interconnected loops dominates the topology, and loops in pial arterioles can ensure an adequate supply of blood after the vascular occlusion, as shown by experiments by Pablo Blinder et al. [13] and Chris B Schaffer et al. [14]. Also, from the study of Keiichiro Maeda et al. [15], the genetically altered mice with augmented anastomoses in their surface vasculature had a more efficient collateral blood supply that can delay ischemic injury. Nevertheless, compared with mice brains, mycelial fungi, which live in soil and endure more rapid environmental changes, their topological graph metrics show an even larger amount of wiring redundancy that allows the fungi to adapt and survive [12].

Clearly, most realistic biological networks in nature contain loops and wiring redundancies. However, past studies on building vascular network adaption models failed in stably adapting networks with loops and instead produced tree (i.e., loopless) networks that minimize the energy cost of delivering fluid from a source to multiple sinks [16, 17]. These theoretical models use shear stress, which was shown repetitively in experiments to directly control vessel radii [18, 19, 20, 21, 9], as the cue to adaptation. As a result, whether and how shear stress takes charge of network adaptation is argued extensively between biologists and physicists. My study intends to settle the dispute – by creating a stable adaptation model that contains loops, uses shear stress as its signal to modulate vessel radii, and predicts realistic blood flow distribution shifts across the system under different circumstances, whether normal or pathological.

Based on their characteristic features (discussed in the following session), mammalian cortex and zebrafish embryo trunk are used to study microvasculature structure principles and adaptation principles, respectively.

1.2.1 Case Study: Mammalian Cerebral

The high energetic cost of neuronal firing creates a fundamental constraint on the number of synaptic circuits that can be simultaneously active [22]. Yet, the brain has no capacity to

store glucose, and must continuously meet its energy needs via the perfusion of oxygen and glucose in the cerebral vasculature [23, 24]. The high gray matter content of the cerebral cortex means that it has a high metabolic activity, and is particularly dependent on vascular supply [25].

The cerebral cortex is fed by a dense network of nearly parallel penetrating arterioles and venules, which are themselves fed by, and drain into, pial networks of arteries and veins (Fig. 1.1). Loops within the pial network ensure robust blood delivery even should a pial artery become occluded [14, 13], and loopiness in general is thought to endow transport networks with the ability to resist damage, and to respond to changes in demand [26, 27], though at the cost of increasing the transport cost of the network under conditions of constant flow [28].

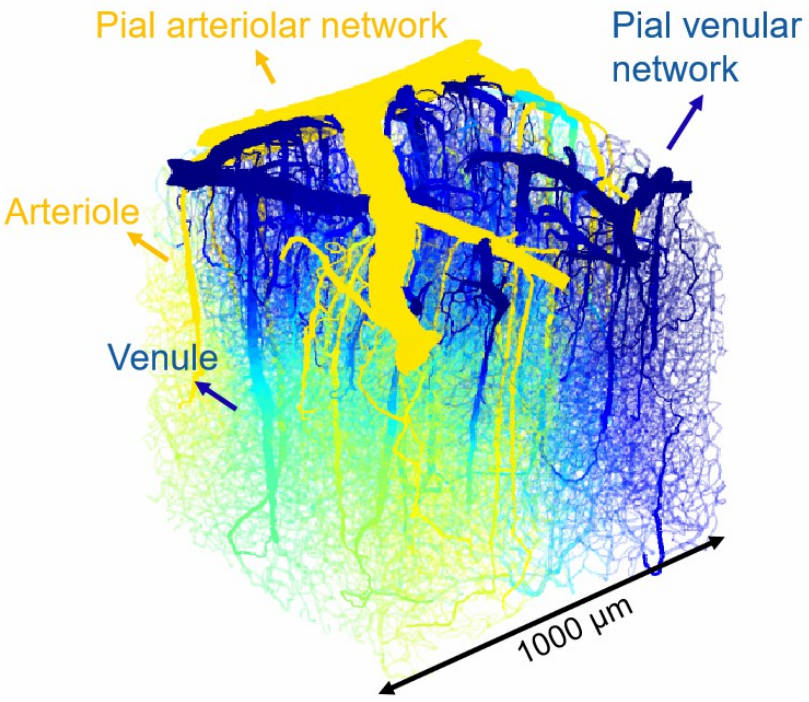

Figure 1.1: The hierarchical system of a real mouse brain vasculature. The color indicates the predicted pressure distribution.

From the pial network, the cortex is perfused by a dense set of penetrating arterioles and venules, along with an interconnecting network of capillaries. The penetrating network

is more vulnerable than the pial network to damage; if a penetrating arteriole or venule is blocked, the neurons it supplies may die and form a cyst [8]. Small volumes of the dense, multitudinous, penetrating network have been mapped by two-photon automated high-throughput histology [8]. Although based on its role as the supply network to an energy-intensive tissue, we would expect the penetrating network to be organized for effective perfusion, it is not clear what physical constraints exist on perfusion, and whether and how these constraints shape the network. In particular, I focus on explaining a conserved feature of mammalian cortices in Chapter 2: the arterioles and venules are not in a one-to-one ratio, but skew consistently for individual species: approximately 2.5:1 (arterioles:venules) for humans [4] and Rhesus monkeys [5], and 0.4:1 for rodents [8].

1.2.2 Case Study: Zebrafish Trunk

Animal microvascular networks perfuse tissues with oxygen and glucose and remove waste. Since red blood cells almost fill the finest vessels, how closely the vessel walls hug red blood cells strongly affects a vessel's conductance, and changes in vessel radius even at the order of tenths of microns can strongly alter vessel conductances and flows [29]. The ability of vessels within this network to find the right radii underlies the networks' ability to distribute blood flows among vessels efficiently.

Even after capillaries are formed, their radii still undergo an everlasting process of changing. The endothelial cells that form the capillary vessel wall constantly migrate and reshape [30], and as a result, dilate or constrict the capillary, or sometimes prune the capillary completely. In zebrafish, even the specification of intersegmental vessels as arteries or veins is not fixed, and endothelial cells can repurpose the vessel identity according to blood flow conditions, showing that genetic programs that direct network growth are not fully determinate [30]. Instead, shear stress cues promote vessel sprouting, specification, remodeling, and regression both during normal development [31, 32, 19, 30], and following injury to the network [33]. Shear-stress cues play similarly vital roles in directing vessel growth and

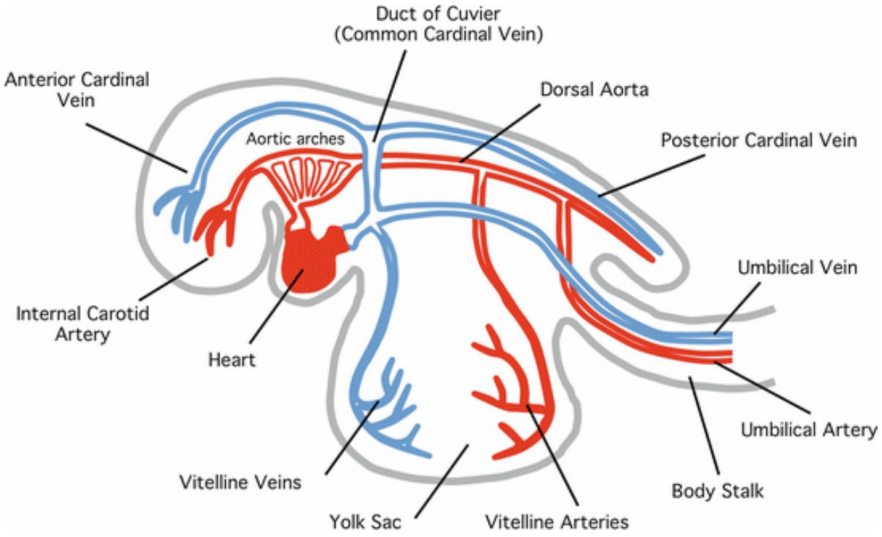

Figure 1.2: The primary blood vessels of the vertebrate embryo [1].

specification and vascular remodeling in other organisms [34, 9].

I chose zebrafish as my model system for vascular development because, 1. same as humans, zebrafish are vertebrate, and the primary network of blood vessels in the embryo is largely shared amongst vertebrates (Fig. 1.2) [1], since we share the same ancestors, 2. zebrafish embryos are transparent, which enables us to observe blood vessels and even blood cells clearly, thus experimental data on blood perfusion can be obtained rather easily, 3. zebrafish trunk microvasculature is a commonly used model system for vascular development [35], and lots of experiments on shear stress adaptation are done on zebrafish embryo [31, 32, 19, 30], and most importantly, 4. zebrafish embryo has a particularly simple structure for study.

Zebrafish embryo vasculature consisting of a parallel artery and vein pair, that, in the embryonic zebrafish are connected both directly by two anastomoses in the distal trunk, and indirectly via a rung-like network of intersegmental vessels (Fig. 1.3) [2]. During the observation of blood flow in the parallel intersegmental vessels (Fig. 1.3) of zebrafish embryo, I found a uniform red blood cell flux across the zebrafish trunk, which is in fact not trivial. To uniformly perfuse the trunk with blood, intersegmental vessel radii have to increase

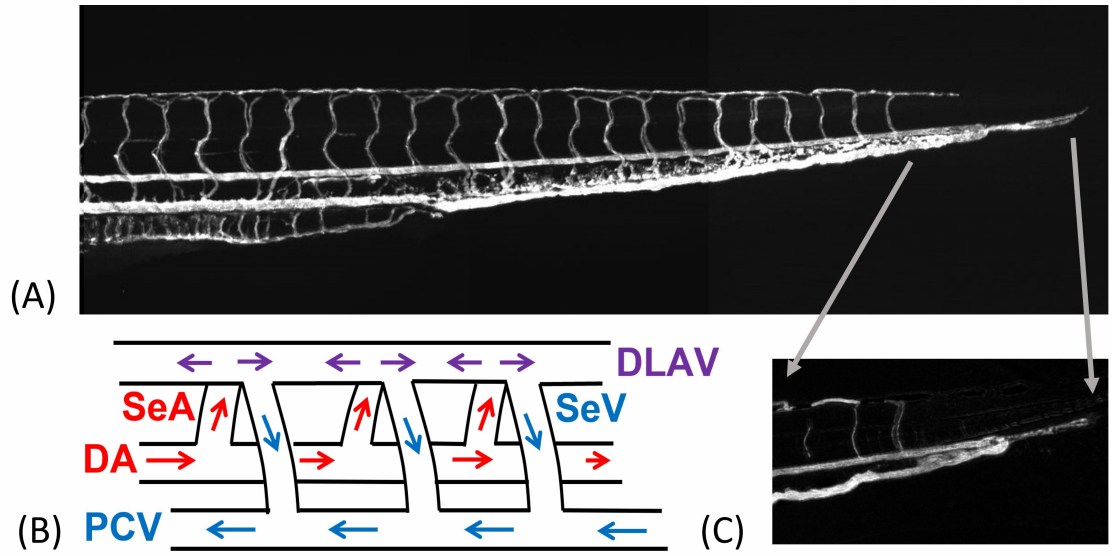

Figure 1.3: The trunk and tail of the zebrafish are perfused by a ladder-like network of microvessels, with inflow along the dorsal aorta (DA) and outflow along the posterior cardinal vein (PCV), along with rung-like system intersegmental arteries (SeAs) and veins (SeVs) linking the two vessels. (A) Composite angiogram of the trunk vessels in a 4 dpf embryo produced from images in the Zebrafish vascular atlas [2]. (B) Simplified wiring diagram of a section of the trunk. (C) DA and PCV are directly connected at the tail

systematically from the head to the tail of the fish [36] to counter the effect of the decreasing pressure; without this precise increase of conductances, the rostral intersegmental vessel would effectively short-circuit the trunk network, receiving greater flow than the most distal intersegmental vessel [36, 37]. What is even more fascinating, this uniform distribution of blood flow disappeared by day 7 after fertilization, along with the decreasing of the hematocrit. How do zebrafish capillaries find their radii to shift the blood flow distribution from uniform to localized under different hemodynamic situations? Chapter 3 will be focused on answering this question.

CHAPTER 2

Microvascular Structure in Cortex: Arterial-Venule Ratio Determines Cerebral Blood Flow Perfusion Efficiency

In the course of the analysis of the mice cerebral network structure, I develop mathematical modeling tools that hybridize network- and continuum- level modeling approaches, treating the arterioles and venules as networks embedded in a meshwork of capillaries, modeled here as a (continuum) porous medium, whose conductivity models the density and geometry of capillaries, without needing to represent each capillary explicitly (Fig. 2.1). The model provides a general tool for studying perfusion in networks where capillaries are too numerous to be completely mapped [38]. Mathematical modeling of both real and idealized cortical networks shows that far from being perfused uniformly, the cortex is strewn with regions of very low flow. These low flow regions are the result of the parallel penetrating vessel structures – between any pair of arterioles, or any pair of venules, there must be a 'dead zone' where flows almost cancel. Increasing the number of perfusing vessels increases the number of low-flow regions. Minimizing the influence of low flow spots sets an optimal arteriole-venule ratio that I find to be closely recapitulated in data from real mammalian cortices. Further, low flow regions complicate the regulation of metabolite delivery with neuronal activity, leading to unintuitive changes in perfusion when penetrating vessels dilate.

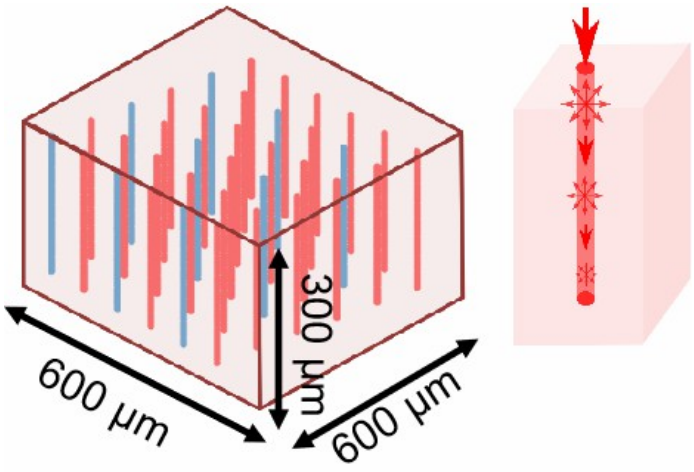

Figure 2.1: Exemplary continuum model where penetrating vessels are treated as lines of sources and sinks, and the capillary bed is treated as porous media. Left: Arrangements of straight penetrating arterioles and venules in the model. Right: Schematic of coupling between penetrating vessels and porous medium - source strength on a penetrating vessel is matched to flux decreases along the vessel.

2.1 Methodology

How can we develop a model to compute the whole cerebral vasculature system? Considering the large number of vessels, the most realistic way is to homogenize the capillaries and use a continuum approach to treat the capillary mesh as a porous media. However the cerebral vasculature is not comprised wholly by the fine capillary mesh that can be homogenized. It is a hierarchical system like in figure (Fig. 1.1) that supplies blood to the brain from pial arteries to descending arterioles, then through the capillary network and drains the blood from descending venule to the pial veins. So in the brain, vascular structures are a superposition of two components: at low scale, a mesh-like capillary component which becomes homogeneous and space-filling over a cut-off length of order of its characteristic length; at larger scale, quasi-fractal branched (tree-like) structures[39]. Thus, a continuum model with the hierarchy of the system taking into the consideration seems natural. Here, numerical methods based on a Green's function approach are presented, and relative to finite-difference methods, the Green's function approach reduces the number of unknowns in the

numerical formulation and allows rapid computations even for complex vascular geometries.

2.1.1 Observations of Low Flow Capillaries

Uniform perfusion – delivery of fluid or metabolites at the same rate to each part of a tissue – underlies the structure of biological transport systems from leaf veins [40] to cardiovascular networks [36]. Does the cerebral cortex (Fig. 1.1) achieve uniform perfusion? Using mapped networks of penetrating vessels, the capillaries that interconnect them, and inferred pressure distributions within arterioles and venules [8], the distribution of flows across all capillaries were analyzed.

2.1.1.1 Low Flow Capillaries in Real Mouse Vasculature

Flows were highly heterogeneous across mapped volumes of tissue (Fig. 2.2). At depth $z = 300\mu m$, fluxes in 24% of capillaries are less than 40% of the median capillary flux. (Median flux changes drastically with depth, but measuring over all depths, I observed 24%-29% of capillaries carrying less than 40% of median flux). These low flow capillaries were spread out over the entire plane but appeared to be concentrated near venules (Fig. 2.2), which in the mapped networks outnumber arterioles among penetrating vessels by a factor of 3:1.

2.1.1.2 Low Flow Capillaries in A Corresponding Synthetic Network

To study whether and why low flow spots are clustered around venules, and to bridge between real microvascular networks (Fig. 1.1) and continuum models (Fig. 2.1), a synthetic sensory-cortex vasculatures (Fig. 2.3) was generated.

The model networks are constraint to have straight arterioles and venules to make it easier to visualize and measure distances between low-flow capillaries and the penetrating vessels that feed them (Fig. 2.3). My method for generating synthetic vasculatures directly

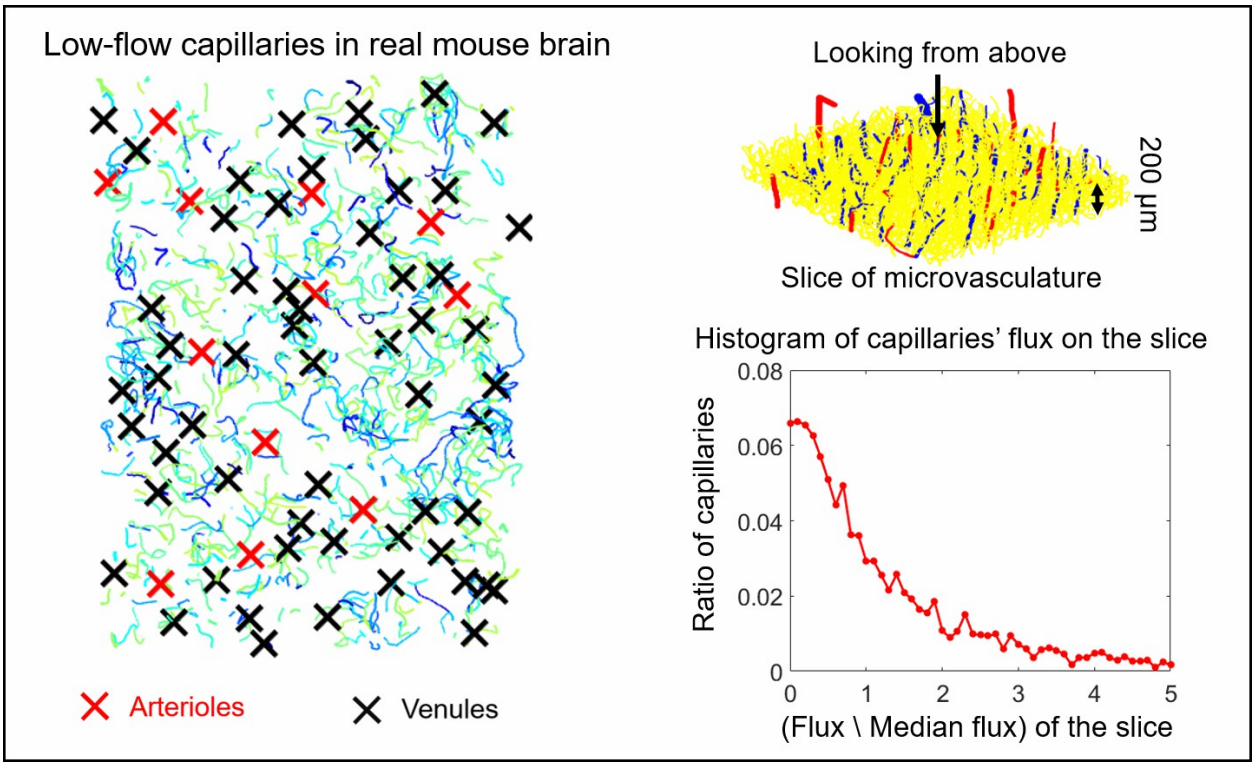

Figure 2.2: Left: The low flow capillaries (vessels with less than 40% of median flux) at depth $z = 300\mu m$ of the mouse cortical vasculature shown in fig:problemA. Right panels: vessel geometry (upper) and flux histogram (lower) in the slice of mouse cortical vasculature. Fluxes are normalized so median = 1.

follows [3]. Specifically, I start with straight, parallel penetrating vessels in the same domain as (Fig. 1.1). I connect these penetrating vessels pairwise at points distributed through the tissue. Then, the points connected to a single penetrating vessel are linked up into a tree with that vessel. The branch point locations and vessel radii within the tree are numerically optimized to obey Murray's law [3]. Conductances are calculated from radii using the same modified Hagen-Poiseuille law and pressure boundary conditions ($50torr$ pressure difference between arterioles and venules) as [8]. synthetic network radii are scaled so that synthetic networks had median vessel radii that matched data from mapped networks [8] (respectively $3.17\mu m$, $3.21\mu m$, and $1.26\mu m$ for arteriole, venule, and capillary segments), and chose the number of pairwise connections so that the number of vertices and median flux per edge in the synthetic networks (19998 and $716\mu m^3/s$) approximated a real network (21895 vertices,

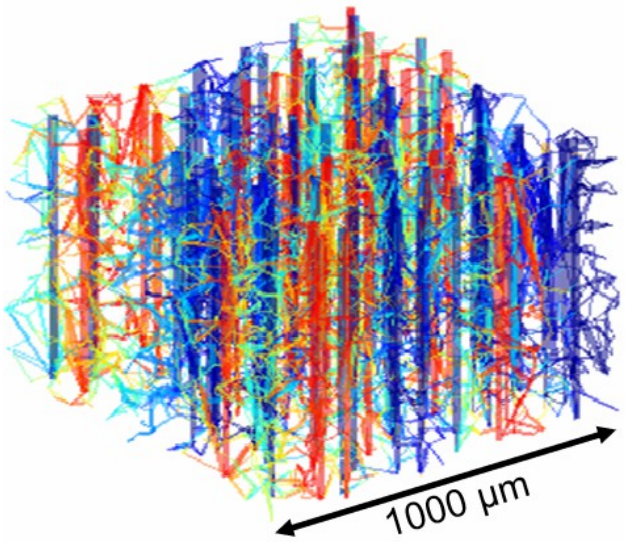

Figure 2.3: A synthetic network constructed using the method in [3], but with idealized straight penetrating arterioles and venules. Color indicates pressure from high (red) to low (blue).

median flux $980\mu m^3/s$). Just as in the real sensory cortex, model networks contained many low capillaries – in the $z = 300\mu m$ plane of the computational domain, flows in 26.8% of capillaries were less than 40% of median flux on the plane (Fig. 2.4). Again results were insensitive to the precise plane on which capillary flow rates were measured.

Low flow regions appear to be clustered near venules in both real (Fig. 2.2) and synthetic (Fig. 2.4) networks. But there are more venules than arterioles in the network, so even a random capillary is more likely to be near a venule than an arteriole. To prove that low flow capillaries are enriched near venules, I compare the proportion of low flow capillaries that are closer to an arteriole than to a venule (measuring distances along the network using Dijkstra's algorithm), with the proportion of randomly chosen capillaries that are closer to an arteriole than a venule (Fig. 2.5). In both the real vasculature and synthetic network low flow capillaries are around 2 times less likely to be found near arterioles than would be expected by chance.

Moving from real mouse data to synthetic networks allows us to probe the extent to which

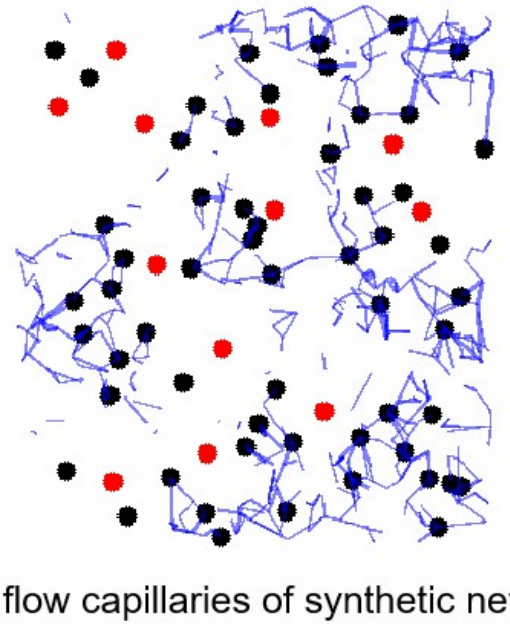

Figure 2.4: Low flow capillaries (vessels with less than 40% of median flux) at depth $z = 300\mu m$ in a synthetic network built to model Fig. 2.2 with same penetrating vessel locations. Black dots: venules, red dots: arterioles. Same annotations are used in Fig. 2.13B as well.

arrangements of penetrating vessels control the placement of low flow regions near venules. Replicate simulations in which venules and arterioles were permuted from the arrangement shown in Fig. 2.4 were implemented. I found that low flow capillaries were consistently 1.43 times less likely to be found near arterioles (Fig. 2.6). In synthetic networks based on the mouse sensory cortex, low flow capillaries cluster near venules. The arterioles and venules were permuted shown in Fig. 2.4 to generate new networks with the same numbers of arterioles and venules. For each permutation, low flow capillaries at depth z = 300 (capillaries with flow rates less than 40% of the median flow rate for the plane) are identified, and the fraction of low flow capillaries closer to an arteriole rather than a venule are found. The fraction was normalized by the fraction of all capillaries which are closer to an arteriole. I find that across all of the vessel arrangements, low flow capillaries are between 1 and 3 (median 1.4) times less likely to be close to an arteriole than would be expected by chance.

Although real sensory-cortex and synthetic microvasculatures exhibit regions of capillaries

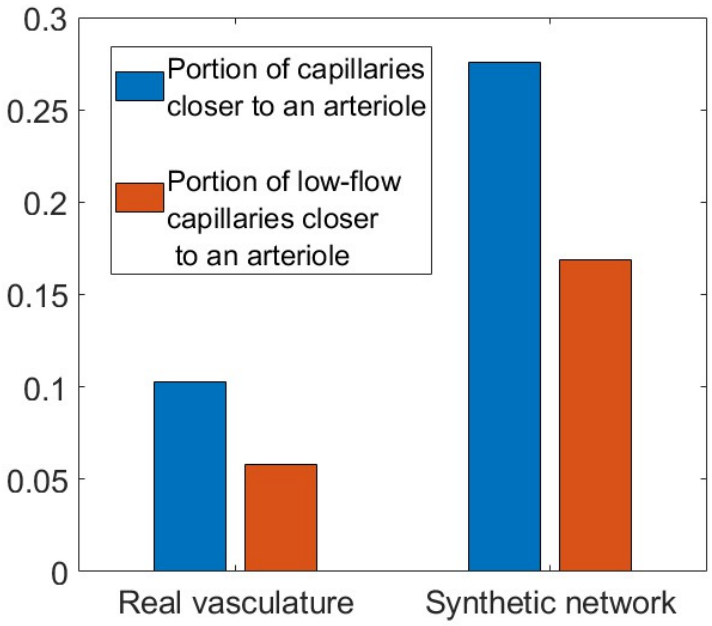

Figure 2.5: In real and synthetic networks, low flow regions are 2 times less likely to be found near arterioles than would be expected by chance. Blue bar and red bar respectively show the portion of all capillaries or low-flow capillaries that are topologically closer to an arteriole than a venule.

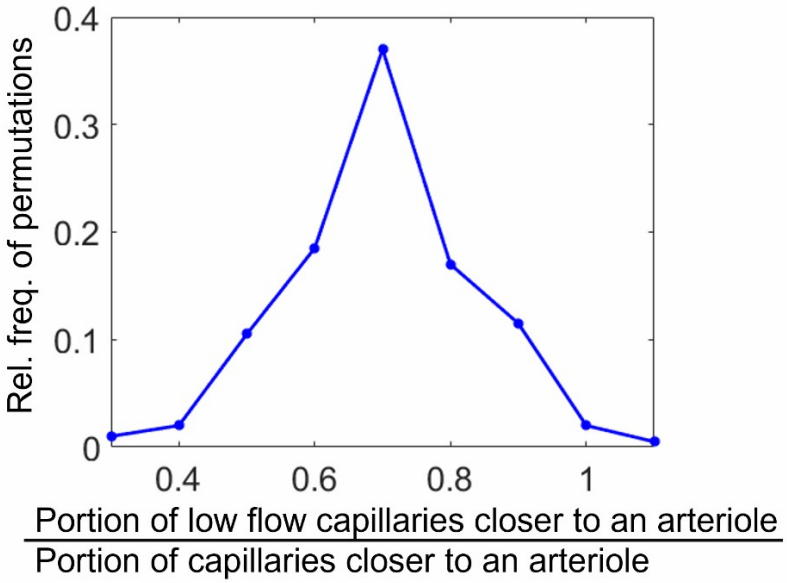

Figure 2.6: Histogram of the portion of low flow capillaries closer to an arteriole to the portion of capillaries closer to an arteriole. In synthetic networks based on the mouse sensory cortex, low flow capillaries cluster near venules.

with low flow, mechanistic understanding of what produces low flow regions requires study of networks that are simplified enough that vessel configurations and arteriole-venule ratios can be effortlessly varied. Accordingly, I built an even simpler continuum model (Fig. 2.1) with not only straight arterioles and venules, but in which the capillary network is modeled as a porous medium. The same penetrating vessel arrangements can be simulated both as continua and as hierarchical synthetic networks, allowing us to validate continuum networks using synthetic networks that are known to capture many of the geometric features of the real microvasculature [3].

2.1.2 Green's Function Method

In this method, I use a line of sources to represent the descending vessels, and use a porous media model to represent the capillary network. For each source, since the governing equation for the porous media, Darcy's Law, is linear, the green's function for each source and use a

linear combination to find the pressure field of the whole capillary network can be found. On the other hand, the pressure in the descending vessels should be consistent of the pressure field of the capillary network, and the strength of each source should be computed such that it is consistent of the lose of blood in the descending vessels. Finally, with the strength of each source, the pressures at the desired locations are computed. This method is computationally efficient because it reduced the 3D problem to the 1D problem of finding appropriate source terms for each descending vessel segment.

A Continuum model of the Capillary Bed The penetrating arterioles and venules are represented using a slender-body theory approach [41]; i.e., each penetrating vessel is treated as a line of linked sources or sinks that push blood into or draw blood out of a porous medium, representing the capillary network [42]. (Similar ideas have been used to simulate the oxygen transport to the tissue in [43], and in [44] where both the tissue and the capillaries are regarded as a porous media.) The source strengths represent the rate at which blood enters the capillary network at each point along an arteriole, while sink strengths represent the rate at which blood is drained from the capillary network into a venule. Sink and source distributions must be solved self-consistently with the flows within the capillary network.

Flows within the capillary network obey Darcy's law, so that the flow through unit area of capillary bed, $\boldsymbol{q}$ is proportional to the gradient of pressure, p:

$$\boldsymbol{q} = -\frac{\boldsymbol{K}}{\mu} \cdot \nabla p \ . \tag{2.1}$$

Here the permeability, $\boldsymbol{K}$, a rank 2 tensor, encodes at a continuum level the density and orientations of capillaries. I assume that the capillary network is isotropic and homogeneous, so $\boldsymbol{K} = K\mathbf{1}$ where K is a constant and $\mathbf{1}$ is the identity tensor. μ is the dynamic viscosity of the blood, and during the computation $\frac{\boldsymbol{K}}{\mu}$ is treated as a single parameter and call it the *conductivity* of the capillary bed. I set $K/\mu = 8\ \mathrm{Pa}^{-1}\mathrm{s}^{-1}\ \mu\mathrm{m}^{-4}$ to match the average conductivity in real sensory cortex data. The discrete networks in [8] is converted to an equivalent

porous medium by imposing unit pressure gradients throughout the domain sequentially in each of the x, y and z-directions, calculating the mean flux in 3 directions to obtain a 3 by 3 matrix. The off-diagonal entries of this matrix are close to zero, and $\frac{K}{\mu}$ is identified with the average of the 3 diagonal entries.

Since Darcy's Law is linear, I can build up p by solving for the pressure field for individual vessels. In the slender-body approximation, vessels are modeled by lines of point sources, so the solution for each vessel is built up in turn from the solution for a point source. Consider a single vessel with centerline $C = \{\boldsymbol{x} \ : \ \boldsymbol{x} = \boldsymbol{x_0}(s) \ , \ s_{min} < s < s_{max}\}$, where s is the arc length along C. Conservation of flux implies that the pressure field due to a single source of unit strength at $\boldsymbol{x_0}(s)$ (generally called the Green's function $G(\boldsymbol{x}, s)$) solves:

$$-\frac{K}{\mu}\nabla^2 G(\boldsymbol{x}, s) = \delta(\boldsymbol{x} - \boldsymbol{x_0}(s)) \ . \tag{2.2}$$

The computational domain is the box: $0 < x < W$, $0 < y < L$, $0 < z < H$, with z representing the distance from the cortical surface. Because only a small part of the cortex is simulated, periodic boundary conditions are implemented in the $x-$ and $y-$ directions, effectively stacking the network with replicates of itself in those directions to simulate a wide and thin sheet of penetrating vessels. In the simulations shown in this study, the model takes $W = L = 600\mu m$ and $H = 300\mu m$, comparable with the mapped tissue in fig:problemA. The penetrating vessels have length $300\mu m$.

No flow boundary conditions are set on the porous medium, i.e., $\frac{\partial p}{\partial z} = 0$ on the cortical surfaces $z = 0$, H, representing the confinement of flow to the modeled layer of tissue. Periodicity is achieved in x and y by Fourier expanding the solution in the $x-$ and $y-$directions: $\tilde{G}(x, y, z; s) = \sum_{k \in 2\pi\mathbb{Z}/L, l \in 2\pi\mathbb{Z}/W, \ (k,l) \neq 0} f_{k,l}(z) e^{ikx+ily}$, where G is obtained from $\tilde{G}$ by adding the zero wavenumber component, and I can rewrite Eqn (2.2) in terms of the functions $f_{k,l}$:

$$\left(k^2 + l^2 - \frac{d^2}{dz^2}\right) f_{k,l}(z) = \frac{\mu}{KWL} e^{-ikx_0 - ily_0} \delta(z - z_0) \tag{2.3}$$

Comparing individual Fourier terms in Eq.(2.3), ODEs for each $f_{k,l}$ are obtained, which when combined with the boundary conditions $f'_{k,l}(0) = f'_{k,l}(H) = 0$ yield:

$$f_{k,l}(z) = \begin{cases} A\cosh Jz, \text{ for } z < z_0 \\ B\cosh J(z-H), \text{ for } z > z_0 \end{cases} \tag{2.4}$$

where $J = \sqrt{k^2 + l^2}$ and A and B are calculated such that the solution is continuous at $z = z_0$ but its derivative has a jump of $\frac{\mu}{KWL} e^{-ikx_0 - ily_0}$ at $z = z_0$:

$$\begin{cases} A\cosh Jz_0 = B\cosh J(z_0 - H) \\ J(A\sinh Jz_0 - B\sinh J(z_0 - H)) = \dfrac{\mu}{KWL} e^{-ikx_0 - ily_0} \end{cases} \tag{2.5}$$

When $k = l = 0$ the solution of (2.3) for a single source or sink diverges. The 0-wavenumber solution for the entire set of sources and sinks is derived by solving directly for the average pressure $\langle p(z)\rangle = \frac{1}{WH}\int_0^W \int_0^L p\, dxdy$ and an average net flux: $\langle Q(z)\rangle = \frac{1}{WH}\int_0^L \int_0^W \alpha dxdy$, where α is the strengh of the sources or sinks. Averaging the mass-conservation law for the entire x and y domain, I obtain:

$$-\frac{K}{\mu}\frac{d^2}{dz^2}\langle p(z)\rangle = \langle Q(z)\rangle \tag{2.6}$$

which may be integrated to obtain:

$$\langle p(z)\rangle = -\frac{\mu}{K}\int_0^z \int_0^\xi \langle Q(z')\rangle dz' d\xi + p_0 \ , \tag{2.7}$$

for some unknown constant p_0. Written in this form, the solution automatically satisfies no flow $\frac{d\langle p\rangle}{dz} = 0$ at $z = 0$. To satisfy no flow at $z = H$ it requires

$$\int_0^H \langle Q(z')\rangle dz' = 0 \quad \text{or} \quad \int_0^H \int_0^L \int_0^W \alpha dxdydz = 0 \ , \tag{2.8}$$

in other words, sources and sinks are balanced within the domain. The overall pressure field is obtained by attaching the zero-wavelength solution $\langle p(z)\rangle$ to the Fourier series.

In a domain containing n vessels with center-lines $\boldsymbol{x}_i(s)$, $i = 1, 2, \ldots n$, each parameterized by arc-length $s_{min} < s < s_{max}$ and with source or sink distribution $\alpha_i(s)$, a pressure field can be derived$p(\boldsymbol{x}) = \sum_{j=1}^{n} \int_{s_{min}}^{s_{max}} \tilde{G}(\boldsymbol{x}, \boldsymbol{x}_j(s'))\alpha_j(s')\, ds' + \langle p(z)\rangle$. The source strengths, $\alpha_i(s)$, are found by requiring consistency with the flows in each penetrating vessel (Fig. 2.1, right). The pressure on each penetrating vessel may be evaluate:

$$p(\boldsymbol{x}_i(s)) = \sum_{j=1}^{n} \int_{s_{min}}^{s_{max}} \tilde{G}(\boldsymbol{x}_i(s), \boldsymbol{x}_j(s'))\alpha_j(s')\, ds' + \langle p(z_i(s))\rangle \tag{2.9}$$

The strength of the source or sink should be equal to the loss (respectively gain) of blood along each penetrating vessel (Fig. 2.1). The amount of blood leaving (or entering) unit length of a penetrating vessel must be equal to the rate of change of blood flow through the vessel. Hence if the conductivity of a penetrating vessel is denoted by $k(s)$ then:

$$\alpha_i(s) = -\frac{d}{ds}\left(k_i(s)\frac{dp(\boldsymbol{x_i}(s))}{ds}\right) \tag{2.10}$$

where $-k_i(s)\frac{dp(\boldsymbol{x_i}(s))}{ds}$ is the flow along the vessel at $\boldsymbol{x_i(s)}$, and I set $k(s) = 90,000\ \mathrm{Pa}^{-1}\mathrm{s}^{-1}\mu\mathrm{m}^{-4}$ to match [8].

I assume that pressures are known at the top of each penetrating vessel: $p(\boldsymbol{x}_i(s_{min})) = P_i$ (P_i = 100mm Hg for arterioles and 50 mmHg for venules) representing their respective connections to the arterial and venous networks, while imposing no flux boundary conditions at their distal ends: $\frac{dp}{ds}(\boldsymbol{x}_i(s_{max})) = 0$. Eqs. (2.9) and (2.10) are numerically solved together. If each penetrating vessel is discretized by m points, $s = s^j$ $j = 1, \ldots m$, then there are $2mn + 1$ unknowns, namely: $p_i^j = p(\boldsymbol{x}_i(s^j))$, $\alpha_i^j \equiv \alpha_i(s^j)$, and the constant p_0 in the 0-wavenumber solution (Eq. 2.7). (2.9) provides mn linear constraints, (2.10) and its boundary conditions, an additional mn linear constraints, and (2.8), the condition of balanced sources

and sinks, provides the final linear constraint. Thus, a single matrix solve is sufficient to find all of the unknowns. Once the source strengths α_i are solved for, the pressure field can be quickly computed across the entire domain using FFTs (fast Fourier transforms). Building and solving the continuum model for a single configuration of penetrating vessels requires approximately 4 minutes on a notebook computer, compared with 70 minutes to create and solve a synthetic network, and this immense acceleration allows us to use the continuum model to analyze a wide space of vessel ratios and arrangements. Numerical convergence studies were performed to determine how many discretization points are needed to model each vessel, and how many Fourier modes are necessary to represent the associated Greens functions.

2.1.3 Numerical Convergence Study

I test the convergence of the slender-body model, to determine how many discretization points (point sources or sinks) are needed to accurately represent each penetrating vessel, and how many Fourier modes are required to represent the associated Green's functions.

Numerical tests are performed on a model tissue that is perfused by three straight penetrating vessels – one arteriole and two venules (Fig. 2.7). I assume that all unknowns have been non-dimensionalized so that the computational domain is rendered by a 50x50x50 box, vessel lengths are all set equal to 20, vessel conductivities are k=10, the porous medium conductivity, $K/\mu = 1$, and that the pressure at the top of the arteriole is P=10, while at the top of the venules P=-10. It' also assumed that at their deepest points, the flow through each penetrating vessel must vanish. The porous medium model for the capillary bed has vanishing flux at z=0, 50, so that blood does not flow from the cortex into neighboring tissues, and periodic boundary conditions are imposed in both x- and y- directions, so that the domain is effectively extended to infinity in each of these directions by side-by-side copies of the penetrating vessels.

Numerical convergence was tested for, in the sense of increasing the number of Fourier

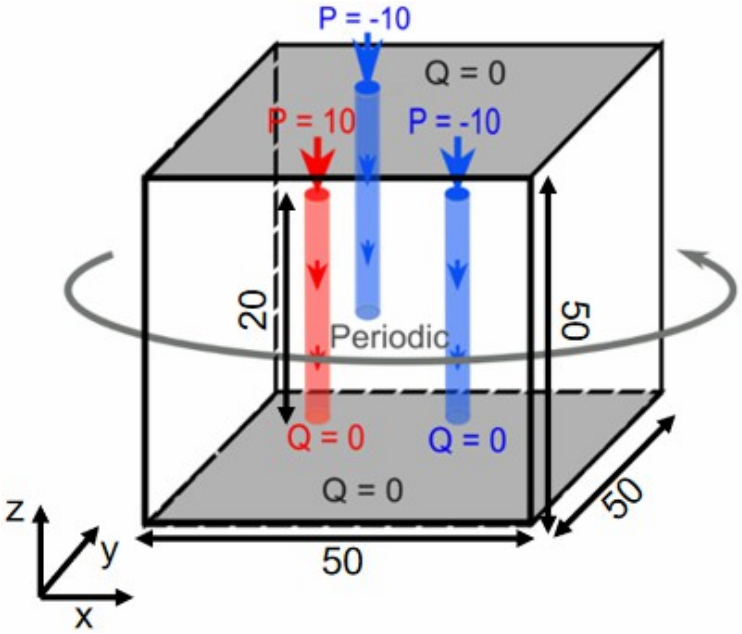

Figure 2.7: Schematic plot of the validation problem. A cubic box has a side length of 50, the penetrating vessels have length 20, and they are located in the middle of the depth.

modes or discretization points used for each vessel – that is, I check that the continuum solution solves Eqs. (2.9) and (2.10). At the same time, I compare the continuum solution with two different network models for the capillary network; one in which the capillary mesh is a uniform grid of vessels with identical conductances and one in which it is represented by a highly disordered network of vessels with identical radii but different lengths.

For the continuum model, the slender-body theory approach is used to compute the source and sink distributions and then the pressures everywhere: i.e., Eqs. (2.9) and (2.10) are formulated as a linear algebra problem that can be solved by a single matrix division, performed using mldivide in Matlab (Mathworks, Natick, MA).

I first analyze the numerical convergence of the slender-body method. Both the number of points N, used to discretize the source distribution, and the number of Fourier modes Nx, Ny in x and y are varied, respectively, used to reconstruct the Green's function. Because the Green's function is singular at the location of the source, the convergence of the Fourier series is algebraic, but Nx, Ny, N 100 are sufficient to keep numerical error less than 0.1 (Fig.

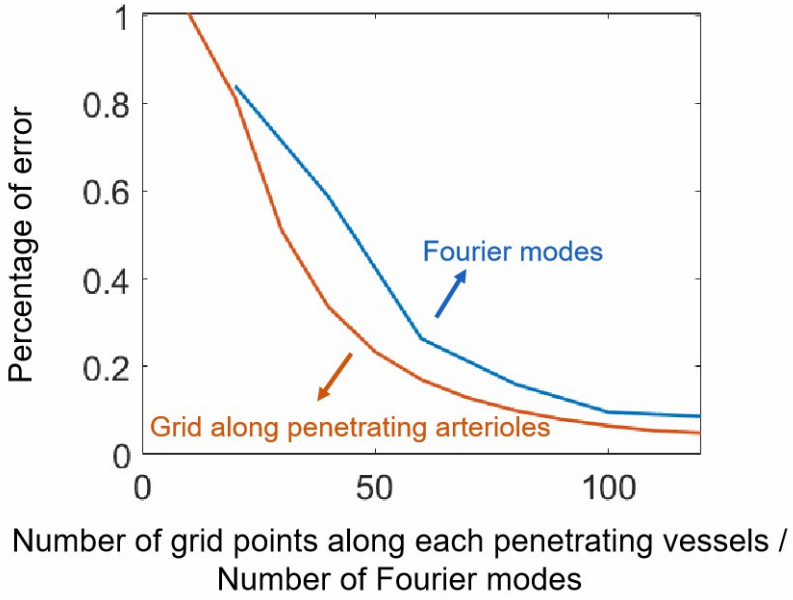

Figure 2.8: Grid independence study. Red and blue lines represent the percentage differences between computations at grid sizes 20, 30, 40, ... as the grid along penetrating vessels increases (red), and as the number of Fourier modes is increased (blue). Convergence results support using N=100 source/sink points per vessel, and Nx= Ny =100 Fourier modes.

2.8).

I then test how closely the continuum model approximates the flows in discrete regular, and disordered networks with the same permeability. For a regular capillary mesh, I link the vessels together by a cubic mesh of evenly spaced capillaries, each parallel to one of the x-, y- or z- axes. Periodic boundary conditions are realized by identifying meshpoints on the face x=0, with meshpoints at x=50, and similarly identifying points at y=0 with meshpoints at y=50. The total number of capillaries is regulated in the network through the grid spacing. To visualize the fidelity of the continuum model to the discrete network model, the pressure is evaluated along several lines y= constant, at height z = 21. Pressures are in good agreement along y = 20 and even along y = 25, which passes through two of the penetrating vessels (Fig. 2.9). Importantly, moving further away from the penetrating vessels, all pressure curves converge to the same constant baseline pressure (Fig. 2.9).

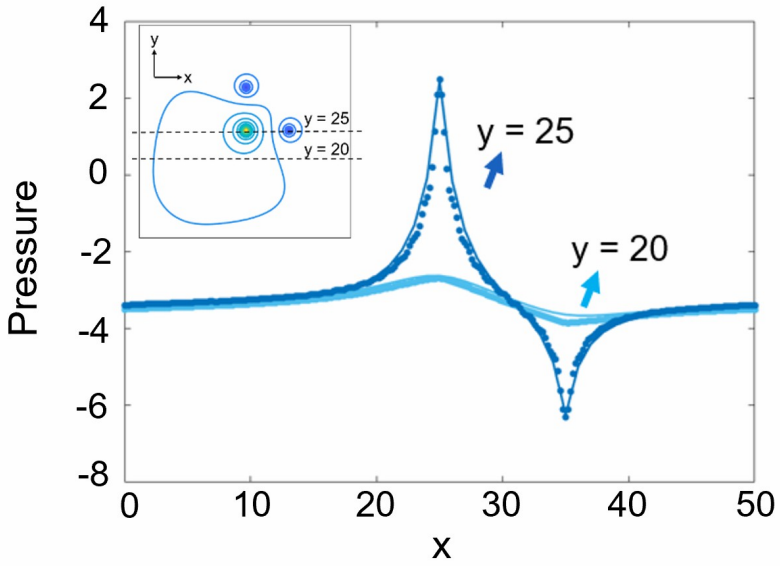

Figure 2.9: Comparison of pressures evaluated along y = 25 and y = 20 lines on the z = 21 plane between continuum (dots) and a regular cubic network (solid line) model shows excellent agreement between the two models, even at the penetrating vessels. Inset figure shows the pressure contour in the z = 21 plane.

To compare the continuum model with a disordered discrete network, I generated random networks by adding random points to the 3D domain and connecting them using Delaunay triangulation. The pressure from both the continuum model and the random network model is evaluated along the line y = 24, z=21. As expected, the relative L2 error of the pressure decreases while the number of random points using to generate network increases (Fig. 2.10), and the pressure of the random network converges to the pressure of the continuum model. Importantly, the relative error is around 6% with 30,000 total nodes in the capillary network – comparable to the number seen in real data sets. Moreover, the modeled pressure converges more quickly than the modeled conductance. At this number of points, the continuum permeability of the discrete network (obtained by calculating the permeability of the capillary network across boxes of side length 5), still has a CV close to 1. The convergence of the pressure field is likely to result from the smoothing that occurs when I invert the incompressibility equation Eq. (2.2) to compute pressures. Taken together with the comparisons

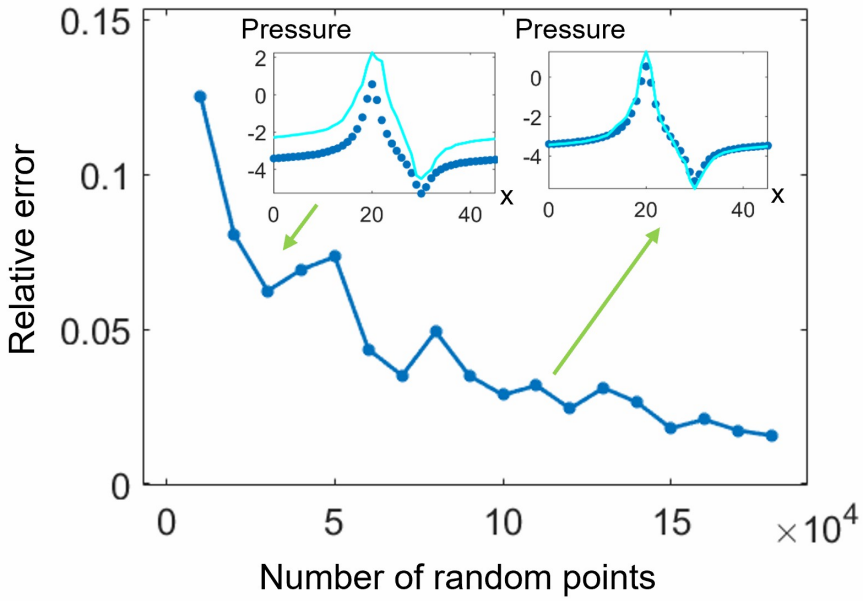

Figure 2.10: The relative L2 error of pressure along the line y = 24, z = 21 in the continuum model compared to the pressure of isotropic random networks generated by Delaunay triangulation. In the inset figures, lines represent the pressure along the line from the continuum model; dots represent the network model's pressure. Decay in relative error appears algebraic. Importantly, with 20000 branch points in the random network, relative error is around 6%, and continuum pressure is close to identical to the network model (left inset).

with hierarchical synthetic networks presented in the following results, these data suggest that the continuum model can be successfully used to approximate flows where capillaries have some level of heterogeneity in their diameters or densities.

2.1.4 Modeling Vessel Arrangements

The degree of randomness in vessel arrangements can affect the size of low flow regions, so it is essential to the modeling to set the correct level of disorder in vessel placement. I measured the entropy of the number of penetrating vessels within a given distance to any penetrating vessel in the real mouse sensory cortex (Fig. 2.11).

The entropy of real penetrating vessels is consistent with their arrangements being random rather than ordered.

I compared the entropy of the penetrating vessels in the real mouse sensory cortex microvasculature (top left) with simulated arrangements of the penetrating vessels; one completely random arrangement (top right), and for comparison, two ordered arrangements (bottom panels). The entropy of an arrangement of vessels at separation L is calculated by finding, for each vessel, the number of L-neighbors it has (i.e. counting other vessels within distance L). The distribution of L-neighbors, P, is found by normalizing the histogram of L-neighbors, divided into 10 equal-sized bins, and the entropy is calculated as $-\Sigma P log_2 P$. The entropy of the real microvasculature is comparable to the random and far exceeds ordered distributions at intermediate and large length scales (Fig. 2.12). At small length scales, the low entropy of the real vasculature shows short-range ordering–likely due to short-range exclusion of vessels from the same spaces, which enforce a minimum separation between vessels. Real vessel arrangements have higher entropy even than random networks, except at the smallest scales (spacings less than $\sim 200 \mu$m), presumably because in real networks, vessels are not allowed to be on top of each other, while the random distribution has no such restriction. Thus, the short range ordering of vessel arrangements is modeled by placing all of penetrating vessels on sites within a lattice, which sets a minimum vessel spacing of

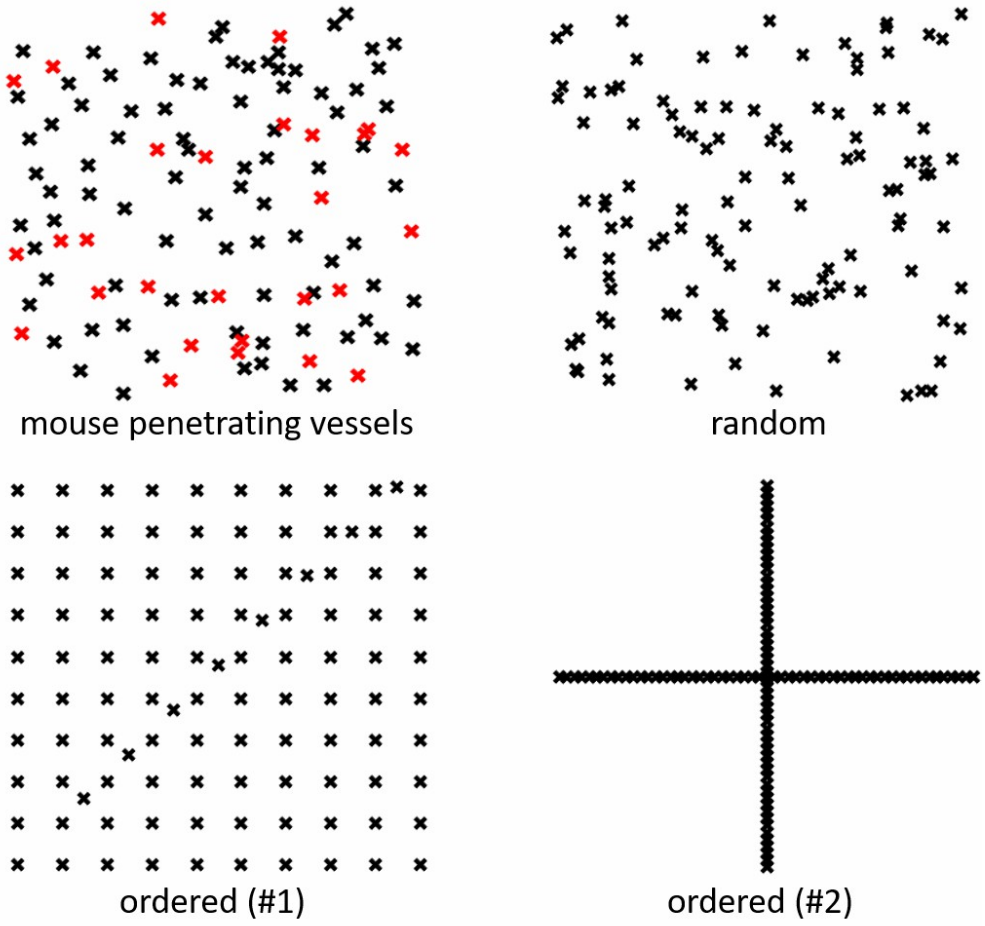

Figure 2.11: The entropy of the arrangement of penetrating vessels in the real microvasculature is compared to a random distribution and two ordered distributions.

100μm.

2.2 Results

To explore the effect of low flow regions upon the overall perfusion efficiency of a tissue, vascular networks in cubical domains containing 12 venules and 24 arterioles (Fig. 2.1) are modeled. Initially random configurations of vessels (representative data shown in Fig. 2.13A) are considered. I validated results from the continuum model against synthetic hierarchical networks, finding that continuum and network models agree in the shape and location of low

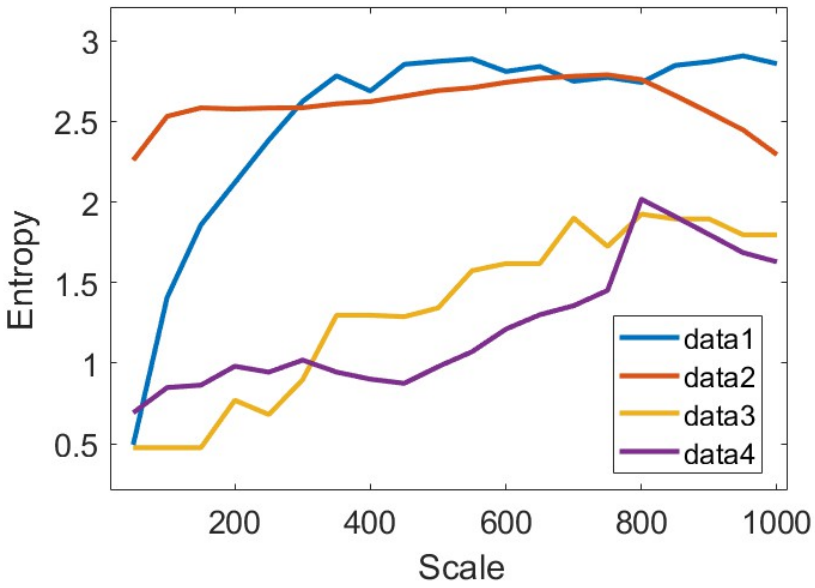

Figure 2.12: Entropy in different scales. The entropy of real penetrating vessels is consistent with their arrangements being random rather than ordered.

flow regions (comparing Fig. 2.13A, Fig. 2.13B, and that the resultant fractions of poorly perfused tissue are strongly correlated between models (Fig. 2.13C).

The uniformity of perfusion in the midplane of the domain ($z = 150\mu m$) are measured from histograms of the flow sampled at every grid point (Fig. 2.13F). Fluxes in the midplane are non-uniform ($CV = 0.9044$ for random vessel arrangement), and a main driver of this non-uniformity is low flow regions – 15.4% of grid points carried less than 40% of the median flow. Similar flow non-uniformity was seen at all depths through the tissue (Fig. 2.13D): low flow regions shrink with depth, but their locations and shapes stay roughly the same (Fig. 2.13D: inset).

In my simulations, low flow regions emerge between pairs of arterioles or pairs of venules, where source or sink flows cancel (Fig. 2.13A). Such cancellations are inevitable within a continuum model: In this plane of the sample, the flow of blood is close to planar (in fact, I find that $\int (|q_x| + |q_y|)\, dx\, dy \div \int |q_z|\, dx\, dy \approx 12$), and the number of stagnation points can be approximately count, that is, the number of points at which the blood flow goes

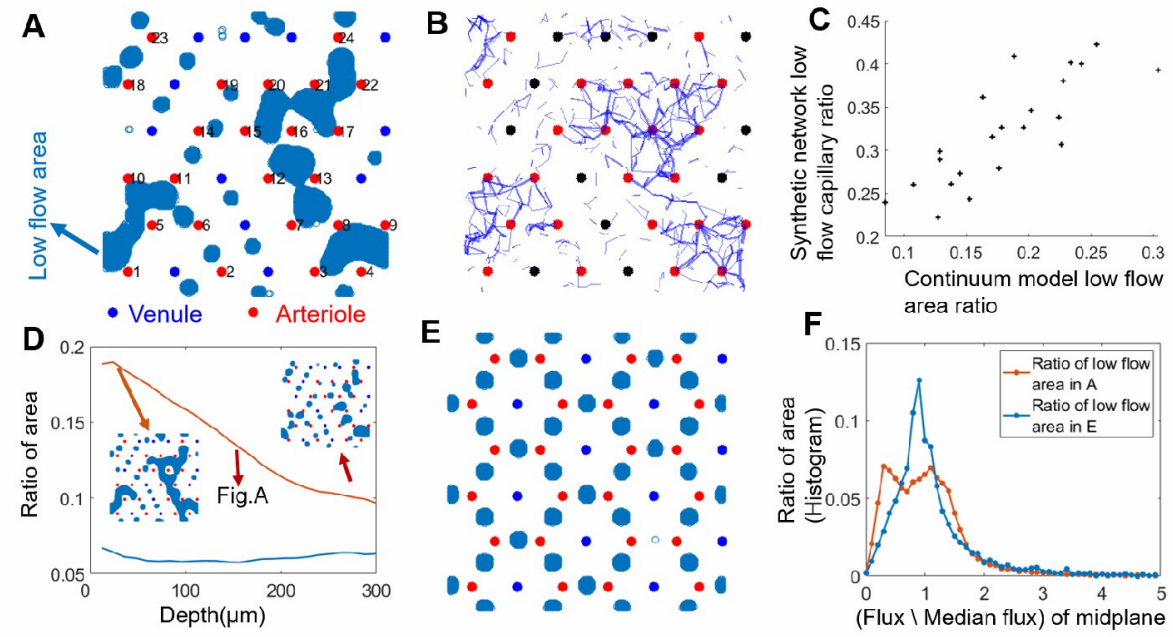

Figure 2.13: A continuum model predicts the same patterns of low flow regions as synthetic discrete networks, and reveals effects of arteriole-venule arrangements on the effectiveness of perfusion. A. Low flow regions (regions with less than 40% of median flux) on midplane are shown in blue for a random distribution of penetrating vessels with a 2-1 arteriole-venule ratio and show a large continuous poorly perfused area surrounded by arterioles. B. Predicted low flow regions match closely to a synthetic discrete and hierarchical network model, with the same penetrating vessel placements (shown in blue: capillaries in midplane carrying less than 40% of the median flux) C. Total low flow area ratio (x-axis) in continuum model predicts the total volume fraction of low perfused capillaries (y-axis) in a hierarchical discrete network model with same vessel arrangements. Each point represents a different random arteriole and venule arrangement. D. The depth in the modeled tissue where low flow regions are calculated affects the total low flow area but only weakly affects comparisons between different arrangements. Red curve: arrangement A, blue curve: arrangement E. Inset figures show how the low flow areas in arrangement A change with depth. E-F: effect of vessel arrangement. E: (Ordered) honeycomb arrangement of arterioles and venules with the same 2-1 arteriole-venule ratio as A. Low flow regions are more numerous but smaller. F. The histogram of fluxes for random (A) and ordered (E) arrangements of vessels.

exactly to 0, using index theory. Because of incompressibility, these stagnation points are all saddlepoints of the vector field given by $\boldsymbol{q}$. Recall [45] that if $\mathcal{C}$ is any differentiable closed contour enclosing a region of a 2D vector field that is differentiable except at a finite set of sources or sinks, then if ϕ is the angle made between $\boldsymbol{q}$ and the $x-$axis:

$$\frac{1}{2\pi}\left[\phi\right]_{\mathcal{C}} = \#\text{ sources} + \#\text{ sinks} - \#\text{saddle points}\ . \tag{2.11}$$

If I let $\mathcal{C}$ enclose the entire periodic subdomain: $0 < x < W$, $0 < y < H$, then opposite pairs of edges in the integral cancel sending the left-hand side of (2.11) to 0. Accordingly, I find that the number of stagnation points is simply equal to the total number of penetrating vessels of any kind. Since each stagnation point in the vector field must be located in a low flow region, then under the continuum model, it is impossible to completely eliminate low flow regions by rearranging vessels.

However, the size of the low flow regions surrounding stagnation points affects the overall uniformity of perfusion and is sensitive to the vessels' arrangement. I compared my results for random arrays to ordered arrays (e.g. Fig. 2.13E). In the shown honeycomb array, small low flow spots are arranged between every pair of neighboring arterioles (Fig. 2.13E). Although there still exist 36 low flow regions (one for each stagnation point), they cover a smaller fraction of the perfused tissue both in the representative plane (7%) and at all other depths (Fig. 2.13D), and the overall non-uniformity is less (Fig. 2.13F, $CV = 0.8545$).

Comparing Fig. 2.13 A, E, it can be seen why disordered arrangements of vessels have larger low flow regions. If the vessels are arranged randomly, then since arterioles outnumber venules, tissue regions that contain only arterioles in their interior and on their boundary are found. Arterioles in the interior of such a region are screened by the arterioles on its boundary and supply much less blood, creating a low flow region.

2.2.1 Adding Arterioles Does Not Increase Tissue Perfusion: An Optimal Ratio of Arteriole-Venule Quantities

Because low-flow regions emerge in regions of tissue containing only arterioles or venules, increasing the number of penetrating vessels may not improve the overall perfusion of tissue. To test the effect of the number of arterioles on cortex perfusion, I placed venules on a regular grid, and then added arterioles randomly, also at grid points to ensure a minimum spacing between vessels (Fig. 2.14 shows the total set of available sites).

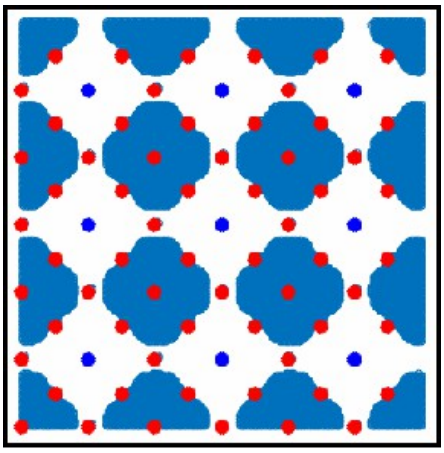

Figure 2.14: Venules are arranged on a uniform square grid, and arterioles are added randomly one-by-one at sites marked with red dots. Blue regions show low flow after all red sites have been filled.

Bboth the total perfusion $\left(\int ||\boldsymbol{q}||^2 \, dxdy\right)^{1/2}$ and the uniformity (fraction of tissue receiving more than 40% of the median flow) were calculated in the mid-plane after each arteriole is added.

When I first start adding arterioles to the network, the overall uniformity of flow increases with the number of vessels, as adding arterioles initially eliminates the low flow regions that form between groups of venules (Fig. 2.15, inset).

However, once the ratio of arterioles to venules exceeds 3, further increasing the number of venules starts to decrease the perfusion uniformity, as regions of tissue bordered by arterioles begin to emerge. At the same arteriole-venule ratios the flux into the tissue saturates (Fig.

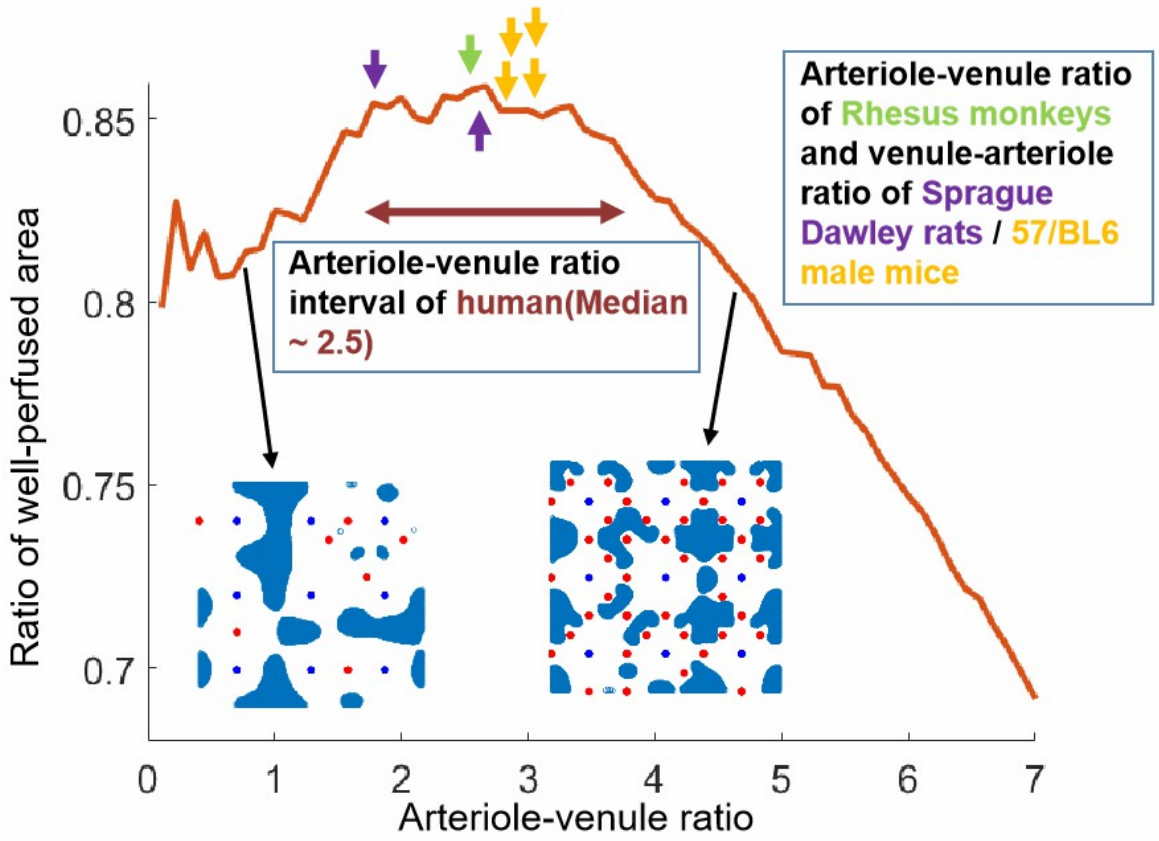

Figure 2.15: Fraction of tissue with low perfusion, for varying arteriole-venule ratio. Arrows show measured most numerous-least numerous penetrating vessel ratios for humans [4], Rhesus monkeys [5, 6], Sprague Dawley rats [7] and C57/BL6 male mice [8]. For primate brains, arterioles are more numerous, so the reported ratio is arterioles/venules; for rodent brains, venules are more numerous, and venule/arteriole ratio is reported.

2.16). Fluxes saturate because pressure conditions are imposed on the ends of arterioles, so arterioles that are added within existing low flow regions do not experience pressure drops large enough to act as significant sources within the porous medium.

Results are insensitive to the threshold at which low flow is identified and to the precise configuration of vessels (three other simulated sequences of increasing arteriole-venule ratio, each with different thresholds, are shown in Fig. 2.17). The optimal ratio of arterioles to venules is weakly dependent upon the vessel arrangement and upon the threshold used to set low flow. As the previous text, low flow regions are defined to be regions receiving less than

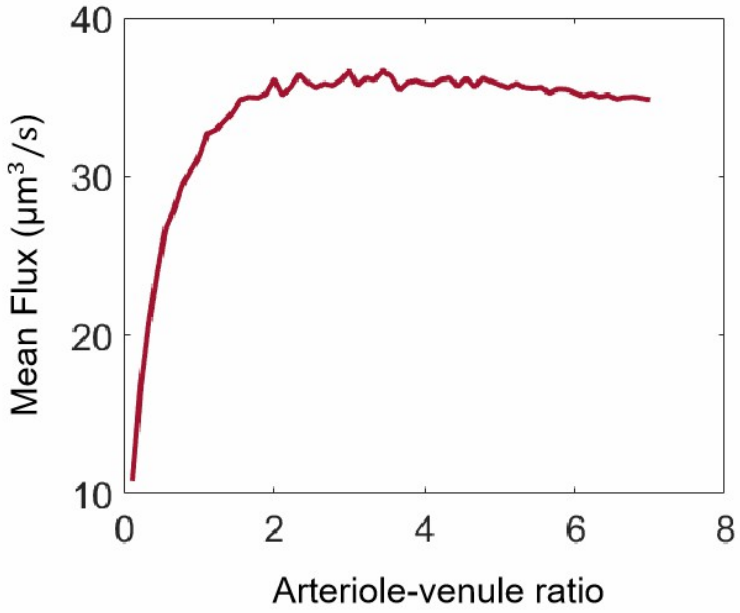

Figure 2.16: Change of mean perfusion with the arteriole-venule ratio when the arterioles are set on the grid randomly one-by-one to vary arteriole-venule ratio.

40% of the median flow taken over the entire cross-section. Results on the optimal arteriole-venule ratio are not sensitive to my choice of a 40% threshold. The calculation shown in Fig. 2.15 is recapitulated, with a different set of vessel arrangements, and using a threshold of 20% (red), 40% (blue), or 60% (yellow) of the median to identify which grid points have low flow. The amount of tissue labeled as well perfused depends on the threshold, but the optimal ratio is always at around 2.3 for this arrangement. When many arrangements were sampled, optimal ratios between 2.3 and 2.6 were obtained.

The modeled ratio (2.6) at which both fluxes into the tissue saturate and the perfusion uniformity starts to decrease quantitatively match the arteriole-venule ratios measured in real primate cortices: including humans; median 2.5 (interquartile range: 1.75-3.7) [4], and Rhesus monkeys; median 2.58 [5]. In mouse or rat brains, there are more venules than arterioles. However, in my calculations, the roles of arterioles and venules can be reversed without affecting the size or number of low flow regions. So another set of optimal configurations exist in which the *venule-arteriole* ratio should be close to 2.6. Indeed the normal ratio of the

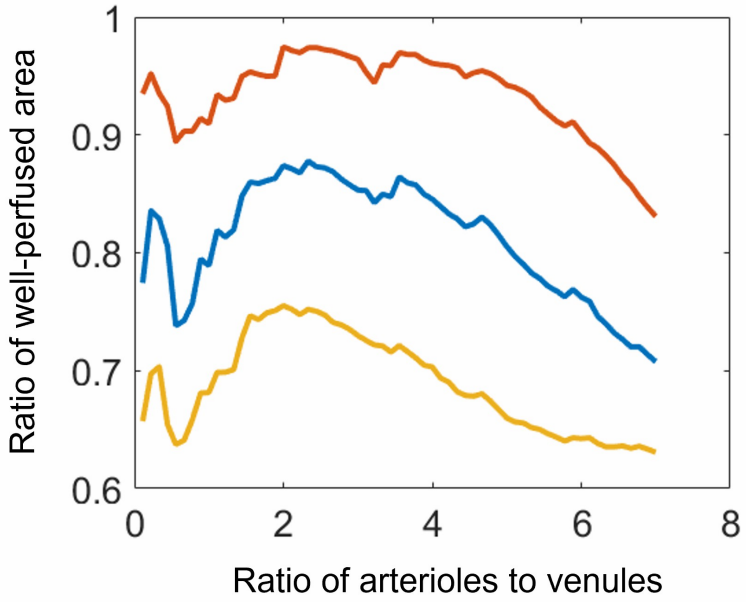

Figure 2.17: Optimal arteriole-venule ratio is not sensitive to where the thresholds are set.

two vessels in mice and rat cortical networks is 2.6-3 [6, 8]. So in both primates and rodents, the most-numerous to least-numerous ratio is very close to optimal for maximizing uniform perfusion (Fig. 2.15). By contrast, when considering microvasculatures outside of the cortex, such as the cat lung, microvessels are not parallel, and, unsurprisingly, the venule-arteriole ratio (1.25) diverges from the predicted optimum [46].

Why would cortical micro-networks have arteriole-venule ratios that optimize perfusion uniformity? Recent studies of the trunk microvasculature of embryonic zebrafish show that the conductances of intersegmental vessels are optimized to ensure uniform flow between vessels, and hence achieve uniform perfusion of the trunk [37, 36]. Perfusion uniformity implies that every tissue receives the same flux of blood, and so may provide a general organizing principle for the arrangement and numbers of vessels in microvascular networks, including in the cortex. Alternatively, arterioles and venules require blood and energy to maintain, and deny space to gray matter; the governing tradeoff for arteriole-venule ratios may be the diminishing returns in total blood supply from increasing the number of arterioles.

Throughout this study (and consistent with mapped networks, Fig. 2.12), a random arrangement of penetrating vessels have been assumed. Yet ordered arrangements of vessels may improve perfusion (Fig. 2.13D-F). I explored the extent to which non-random arrangements outperform random arrangements, by starting with the same lattice of venules (Fig. 2.18A), and varying the arteriole-venule ratio by placing arterioles sequentially and according to a greedy optimization in which each new arteriole was added at the grid point with lowest flow while maintaining minimum distance from all other vessels in the network. This algorithm places arterioles regularly around the Voronoi boundaries between the venules (Fig. 2.18B), avoiding creating any convex regions that contain only arterioles. Under the optimal arrangement, both mean flux and uniformity converge to a limit, rather than selecting for a specific arteriole-venule ratio. Nonetheless, real penetrating vessels have statistically random configurations, at least on large enough length-scales (Fig. 2.12). Indeed, penetrating vessels form nearly simultaneously [47], so optimal arrangements that arise from steering vessels to existing regions of low perfusion aren't possible. Yet, the plateauing of total perfusion (Fig. 2.18C) and perfusive uniformity (Fig. 2.18D) with increasing arteriole-venule ratios means that even under optimal arrangement, if the cost (e.g., from loss of space available to gray matter) of adding additional vessels were included, there would still be an optimal ratio of venules to arterioles.

2.2.2 Penetrating Vessel Conductances Do Not Directly Control Perfusion

In cortical microvascular networks, conductances of penetrating vessels and capillaries dynamically respond to neuronal activity [48, 49]. High neuronal activity requires increased cerebral blood flow (CBF) to meet the tissue's increased glucose requirements [24, 50] (though oxygen demands may also stimulate blood flow responses [51]). Increases in CBF are achieved by the dilation of arteries, arterioles [52, 53], and capillaries [54, 55]. Meigel et al. [56] showed theoretically that the hierarchy of vessel radii in the mouse sensory cortex ensures that the glucose delivered by a particular vessel to the surrounding tissue typically increases when

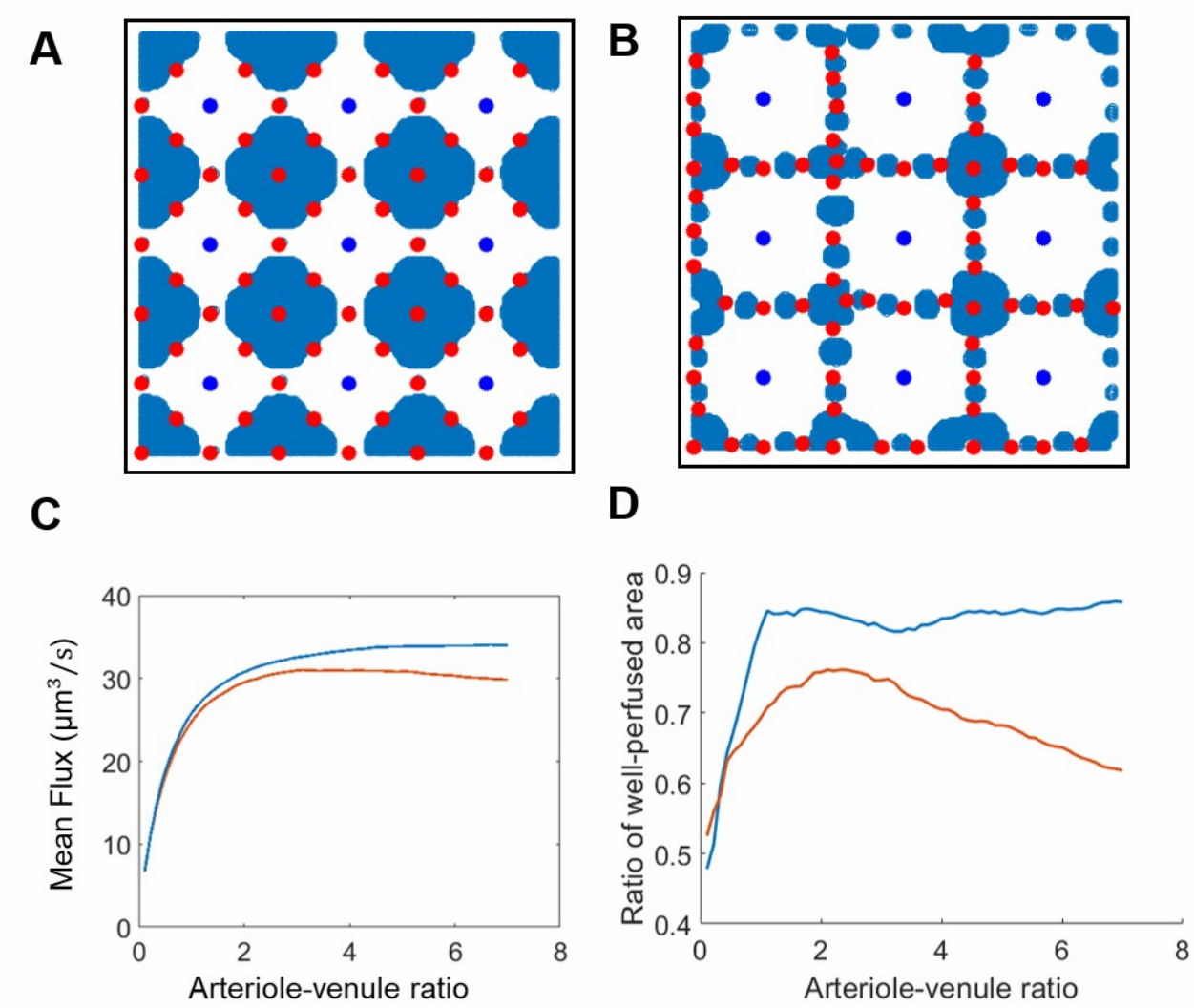

Figure 2.18: Optimal arrangements of vessels (top right panel) can produce perfusion uniformity that does not decrease as more arterioles are added. To construct an optimal network, arterioles are added sequentially by a greedy method, placing them at grid points with the lowest flow. Optimally arranged arterioles do not create large low flow regions (right) compared with non-optimized networks (left). C. Mean fluxes are larger for optimally arranged vessels (blue) than for non-optimal configurations (orange) but still saturate with limitingly large arteriole-venule ratios. D. Optimal arrangements (blue) of vessels produce perfusion uniformities that saturate as arteriole venule ratio is increased, unlike random configurations (orange).

that vessel's conductance increases. However, their analysis did not explore interactions between vessels – specifically how overall tissue perfusion may be affected by conductance changes. I hypothesized that since increasing vessel conductances can change the location of low-flow spots within the tissue, regions of tissue not immediately perfused by the affected arteriole may lose perfusion.

I first performed a perturbation analysis of penetrating vessels using the real mouse vasculature in [8], individually dilating them (increasing their conductances 10-fold) to model vessel dilation or blocking them (setting their conductances to 0) to model ischemic damage within the mapped mouse sensory cortex (venule-arteriole ratio: 2.88). Ten-fold conductance increases were chosen because reported arteriole diameters ranged from 5μm, comparable to a mouse red blood cell, to 12 μm, a regime in which even small changes in vessel diameter can greatly affect conductances [36]. However, my results were qualitatively the same under smaller increases in conductance. In the mouse sensory cortex, venules outnumber arterioles, so low-flow regions are typically bounded by venules (Fig. 2.2). I found then that increasing any arteriole conductance increased flow in the arteriole, consistent with [56], and also increased global perfusion. Similarly, blocking an arteriole consistently reduced global perfusion (Fig. 2.19).

Conductance changes in the more numerous venules, by contrast, led to unpredictable effects. Surprisingly, increasing venule conductance *decreased* mean perfusion for 78 (of 127) venules, while blocking the venule *increased* mean perfusion for 49 venules. For 32 venules, either increasing the conductance or blocking the venule decreased mean flux. Low flow regions tend to form around whichever vessel is more numerous, and the movement of these regions causes nearby vessels to have less precise control over perfusion. Hence the less numerous vessels control perfusion more precisely, or equivalently, fluxes are more robust to changes in conductance, e.g., due to injury, among the more numerous of the penetrating vessels. Similar results were obtained using other samples of real mouse brain vasculature (Fig. 2.20).

To test the hypothesis that low flow regions determine the response of perfusion to vessel conductance changes, conductances are perturbed in continuum models of the cortex. (Mean fluxes in the continuum model (Fig. 2.16, Fig. 2.21C), are numerically much smaller than for the network model (Fig. 2.19) because they are essentially volume averaged, i.e. multiplied by the volume fraction occupied by capillaries, $\phi = 0.86\% - 1.53\%$). For representative comparisons, Fig. 2.21A shows the different effects of individually increasing conductances five-fold in two arterioles (nos. 19 and 16, according to Fig. 2.13A). When arteriole 19, surrounded by a mix of arterioles and venules, is dilated, capillaries in the pathway from the arteriole to the surrounding venules receive increased flow (Fig. 2.21A, upper-left). Other arterioles perfuse less flux into the tissue because of a global increase in average pressures, but the total perfusion increases (Fig. 2.21C). Compared to Fig. 2.13A, the total area of the low-flow region slightly increases while preserving roughly the same shape (Fig. 2.21A, upper-right). Conversely when arteriole 16, surrounded by arterioles, and in the middle of a low-flow region, is dilated, the flux to surrounding capillaries actually decreases (Fig. 2.21A, lower). In other words, dilating the arteriole in the middle of a low flow region may have counterintuitive effects upon perfusion. I systematically and individually dilated each of the 24 arterioles in Fig. 2.13A. For most arterioles, increasing conductance increased mean perfusion (Fig. 2.21C), however mean perfusion decreased when 4 out of 24 arterioles dilate (arteriole 9, 13, 16, 21 labeled in Fig. 2.13A). Although arteriole dilation is usually thought of as a method to achieve a localized increase in perfusion [56, 8], I found that in over half of cases, dilating an arteriole actually created more uniform perfusion, reducing the total low flow area (Fig. 2.21D).

I then studied the effect on perfusion of blocking the same arterioles, representing ischemic damage to the network, similar to that induced in mouse brains using optically mediated occlusion [57]. In separate simulations, arterioles 19 and 16 from Fig. 2.13A were blocked, and the conductance of the blocked arteriole was set to 0. Since arteriole 19 sits on the boundary of a low-flow region, its blocking removed the previous stagnation points between

it and the other arterioles, allowing blood in the low-flow region to flow out to surrounding venules (Fig. 2.21B, upper-left). A lower global pressure also ensures the other arterioles have a larger pressure drop and perfuse more, hence mean perfusion and overall perfusion uniformity increased (fraction of tissue with more than 40% median blood flow increased from 84.56% to 93.85%) (Fig. 2.21D). More importantly, there is no large low-flow area formed near the blocked arteriole 19 (Fig. 2.21B, upper-right). Conversely, when arteriole 16, inside a low-flow region, is blocked (Fig. 2.21B, lower), the surrounding arterioles formed new stagnation points and caused a large continuous area of low flow region around the blocked arteriole. However the mean perfusion and perfusion-uniformity still increased due to the lowered global pressure. Systematically blocking every arteriole in separate simulations, I find that blocking any arteriole increased mean perfusion and perfusion uniformity (Fig. 2.21C,D), but that the largest increases in perfusion uniformity occurred when an arteriole on the boundary of a low-flow region was blocked (numbers on plot identify arterioles from which data was taken). Because of the linearity of the underlying equations, dilating or blocking venules would have similarly unpredictable effects in modeled tissues in which venules outnumber arterioles, as can be seen if arterioles and venules are swapped in the model (Fig. 2.22).

To expose the limits on flow controllability, the change in mean perfusion from dilating a vessel to the change in mean perfusion from blocking the same vessel are compared. For 20 of the arterioles, mean perfusion increased whether the vessel was dilated or blocked. Similar results were obtained when different arrangements of vessels were perturbed in the same way (Fig. 2.23) or when the total inflow into the tissue was plotted instead of the mean perfusion (Fig. 2.24).

2.3 Discussion

I present a computationally efficient method for representing the perfusion of blood through tissues via continuum-level modeling. Assuming a uniform permeability within the capillary bed, I can use a slender-body approximation; replacing penetrating vessels by lines of sources or sinks that fill or drain a continuum model of the capillary bed. This approximation reduces the PDE solution to finding the strengths of sources and sinks along each penetrating vessel. I chose this approach because, in many real situations, complete maps of the microvascular network do not extend below the arteriole level [58], and the structure of the capillary bed between arterioles and venules can only be assumed. In the few networks where comprehensive capillary level mapping has been performed, such as the mouse sensory cortex, the permeability of the capillary bed has some spatial heterogeneity – a CV of 0.8423 was found when I partitioned the domain into boxes of size 2.86×10^{-3} mm^3. Nonetheless, the continuum model agreed in most quantitative respects with synthetic networks that are known to model the conductance hierarchies and connectivities of the real sensory cortex microvasculature. Furthermore, my theory can be extended to model spatially heterogeneous conductances by replacing the known Green's function for point sources by source terms within the porous medium equations, and solving for source strengths self-consistently with fluxes, a problem with a rich set of PDE precedents [59, 60].

With so many sources and sinks distributed through the tissue, it may be unsurprising to see points where flows cancel to produce regions of low flow. Because of the approximately two-dimensional nature of flows in the mid-plane, it can be expected, based on index theory, that the number of these points will simply increase with the number of penetrating arterioles. However, regions of low flow tend to be delimited by groups of penetrating vessels of the same type (either all arterioles, or all venules) setting the sizes of low flow regions, and selecting for an optimal ratio (~ 2.6) of arterioles to venules or conversely, that is remarkably close to the ratios seen in real cortical microvasculatures.

I have not sought to establish whether or not low-flow areas obstruct the transfer of oxygen and metabolites to the tissue, since both may diffuse some distance (the Krogh length [61]) through the tissue. Indeed, in the mouse sensory cortex, the typical spacing of penetrating arterioles is comparable to twice the Krogh length of oxygen $\approx 130\mu$m [62, 61]. In my model, tissue and blood flow have already been integrated into a single continuum, so little modification of the model would be needed to include the transport and diffusion of metabolites. Here, however, I have focused only on perfusive flows, including analyzing the complex effect that changing the conductance of a vessel in a low-flow spot has on the nearby flows. The structural constraints that emerge from this analysis may explain why there is no particular association between penetrating vessels and the neuronal columns they supply [5, 8], and why vessel dilation is never restricted to a single penetrating arteriole [63].

Maximizing perfusion or perfusion uniformity selects for an optimal ratio of most numerous penetrating vessels to least numerous; this ratio can be obtained by having more arterioles than venules (as in primates) or conversely (as in rodents). Do physical constraints also determine which vessel type is more abundant? In Fig. 2.19 and Fig. 2.20, I modeled blocking venules and arterioles in two real mouse brain vasculature systems. Since arterioles are the less numerous penetrating vessels, dilating or blocking an arteriole directly changes blood flow fluxes. By contrast, fluxes are relatively robust to changes in venule conductance. Intriguing hypotheses emerge from this – ischemic damage tends to arise from occlusions within the arterial network, likely due to its vessels being narrower than the venous network, or because dislodged plaques or thrombi encounter arteries before they encounter veins [62]. In long-lived primates, selection may be for networks that are more robust to micro-occlusions that affect arteriole conductances (i.e., there is selection for more numerous arterioles), while in mice that do not live long enough to accumulate this damage, more precise control over perfusion (i.e., less numerous arterioles) may be selected for [56]. In model tissues with more numerous arterioles, I predict striking robustness of perfusion to occlusion of arterioles, which may link to the variable pathophysiology of ischemic events

[64, 65]. Conversely, in experiments with rodent brains, blockage of arterioles invariably leads to cyst formation [6, 62], but so does blockage of venules[6], and I must consider how closely the simple model of removing vessels approximates the damage produced when vessels are blocked experimentally. Nonetheless, the models emphasize the importance of the baseline distribution of low-flow regions when evaluating a microvascular network's tolerance to aging and injury-related damage [66].

The model predicts perfusion heterogeneities caused by the topology of penetrating vessels and their effects on blood flow regulation during cerebral functional activities. Past experiments support my prediction of extreme heterogeneity of CBF [67, 68] as well as the shift in heterogeneity during neuronal activation. However, these experimental studies mainly focused on the heterogeneity of blood flow across individual capillaries and interpreted it as either having unclear physiological significance [69] or classified it as a form of capillary dysfunction [70], and provided little data on the spatial patterns of heterogeneity that could reveal the physical inevitability of low flow regions. Fenstermacher et al. recognized alternating columns of high and low flow rates [71], but speculated that the microvascular flow columns corresponded to cortical neural columns, which was ruled out by [8]. As for perfusion regulation, Yaseen et al. found a global redistribution of CBF in penetrating vessels during a localized functional activation, and stated "it is not well understood how CBF redistributes on a microvascular level in response to localized functional activity" [72]. My theory suggests that these questions may be answered by analyzing spatial patterns of heterogeneity prior to, and CBF redistribution during, neural activity.

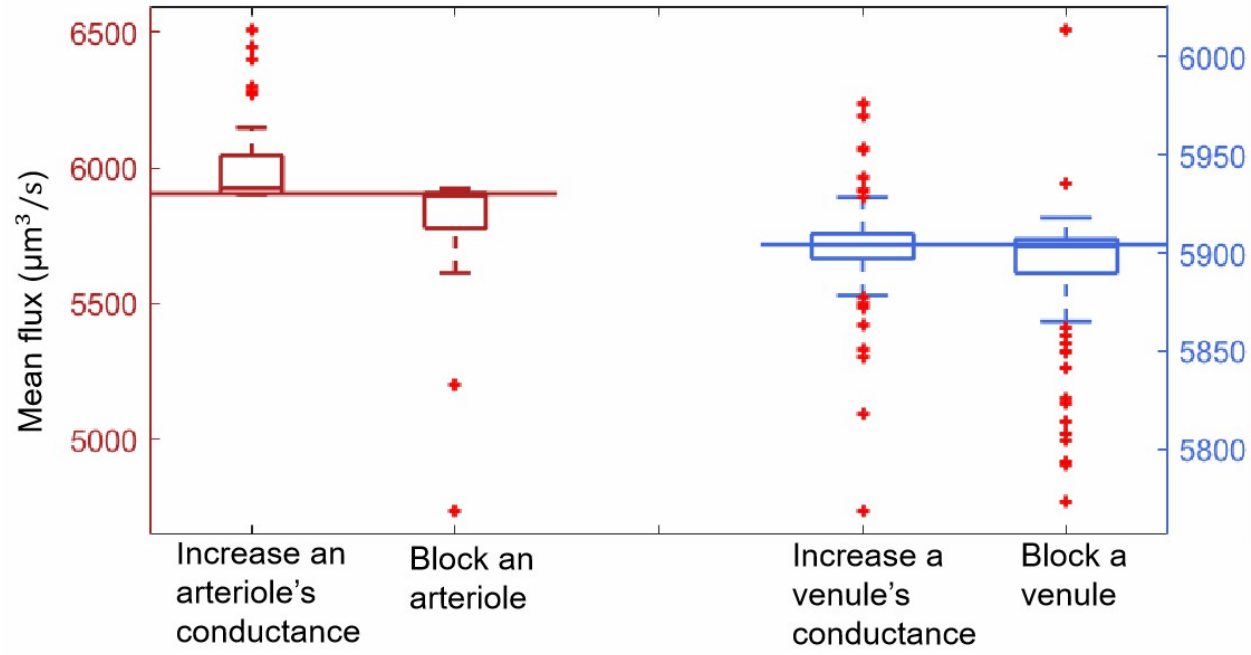

Figure 2.19: The predicted distribution of mean flux on $z = 300\mu m$ plane when the conductance of a penetrating vessel (red; arteriole, blue; venule) is either increased ten-fold or sent to 0. Horizontal lines represent the mean flux before any change.

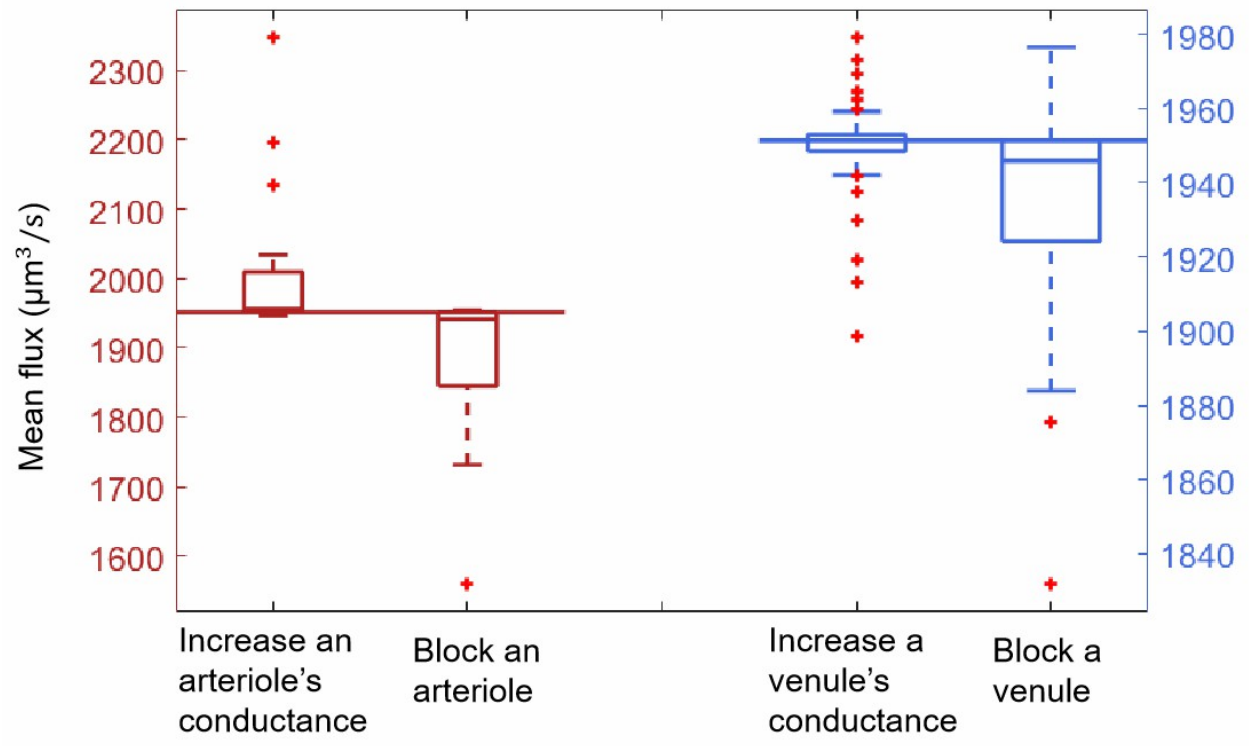

Figure 2.20: In real mouse vasculature, regulating arteriole conductances more precisely controls blood flow in capillaries than regulating venule conductances.

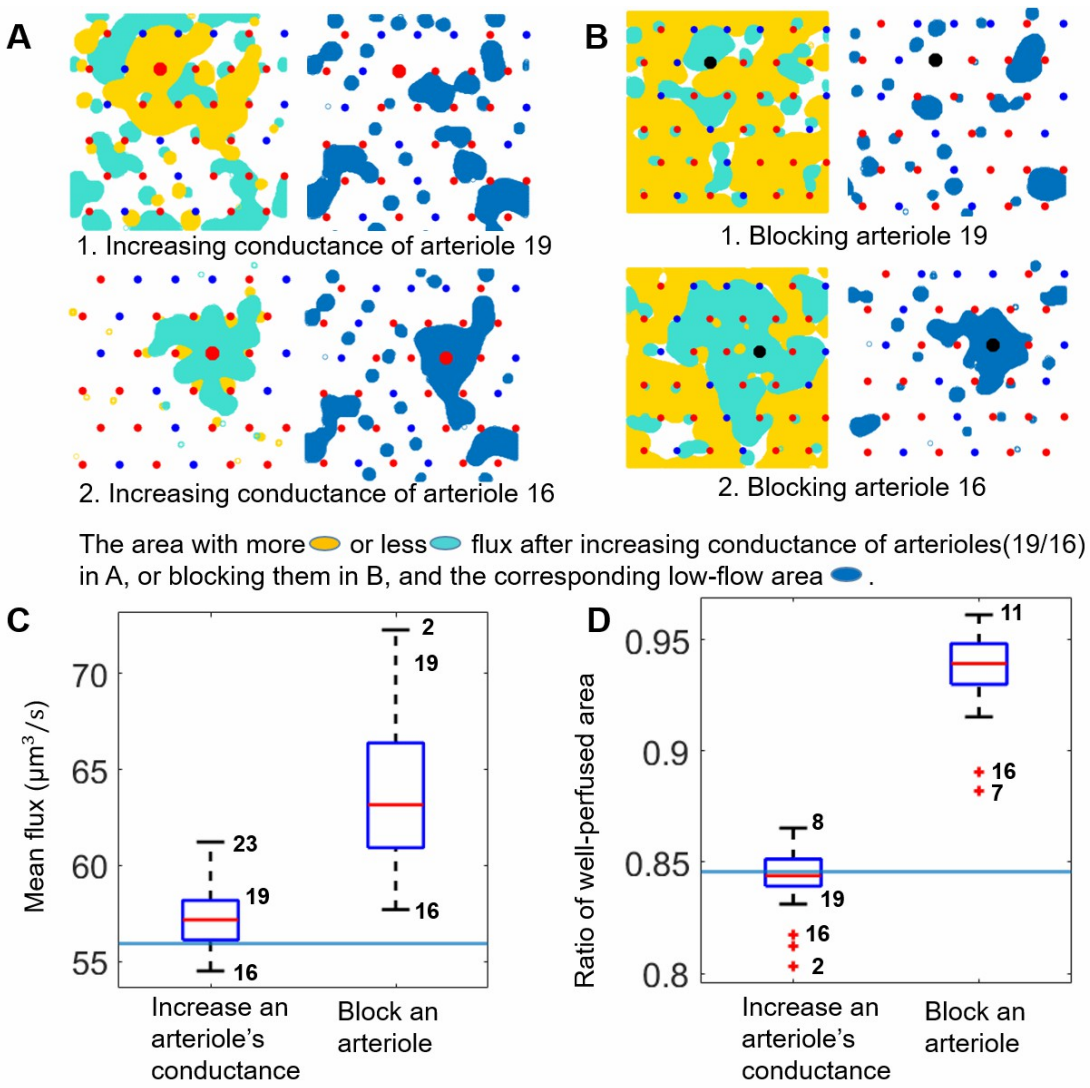

Figure 2.21: In a continuum model with more arterioles than venules, changes in arteriole conductance, but not changes in venule conductance, have unintuitive effects upon perfusion. A, B. Effect of blocking or increasing conductances of arterioles 19 or 16 (the numbering of arterioles follows Fig. 2.13A). Left panels: Colored regions represent areas where flow increased (yellow) or decreased (cyan) by more than 10%. Right panels: Low flow spots after conductance change (blue regions). C. The mean flux distribution after increasing the conductance of individual arterioles five-fold or block them individually. The blue horizontal line represents the mean flux before any conductance change. Mean flux is calculated on the midplane. D. Fraction of tissue in mid-plane that is well-perfused (greater than 40% of median flow) when arteriole conductances are individually increased five-fold or arterioles are blocked. The blue horizontal line represents the ratio of well-perfused area before any conductance change.

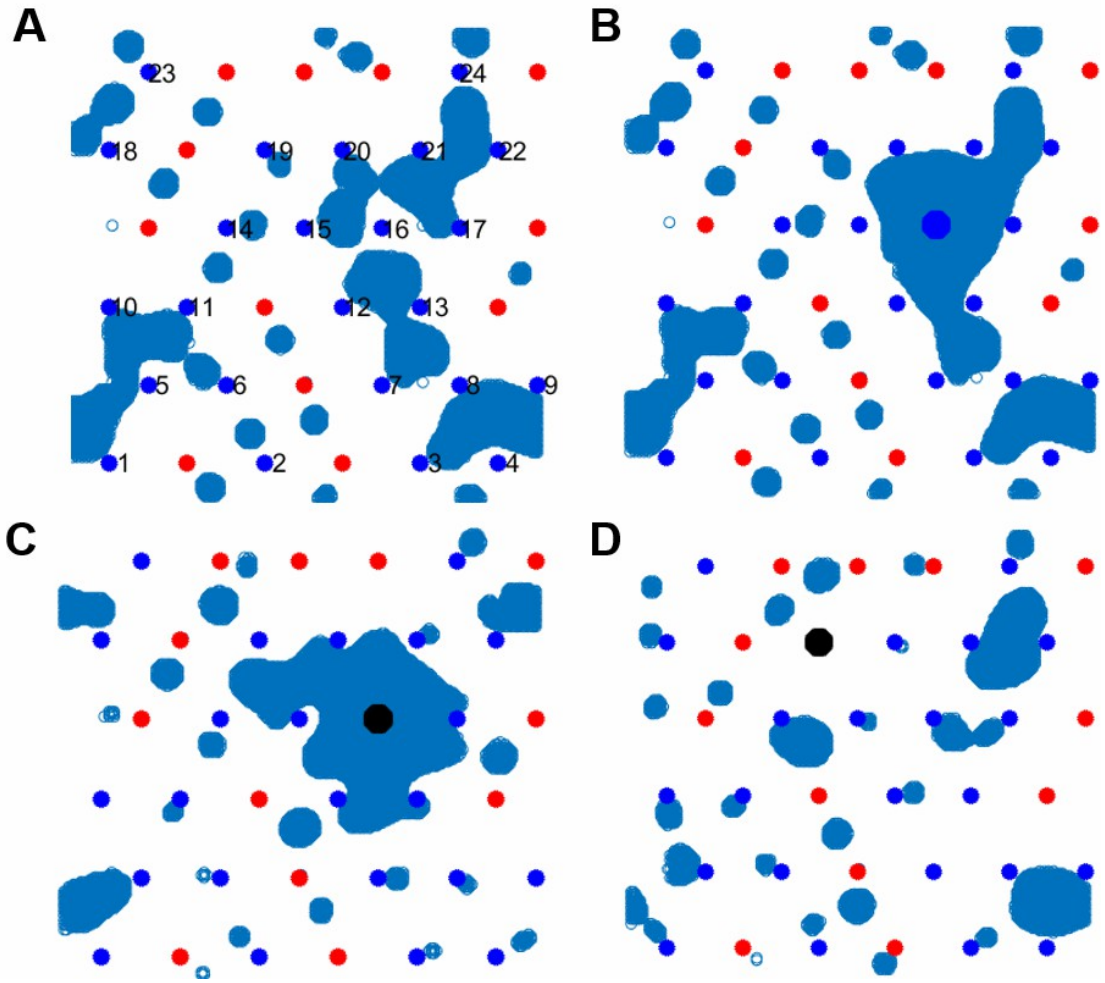

Figure 2.22: Exchanging arterioles and venules in Fig. 2.13A, and redoing the analysis from Fig. 2.21, it can be seen that their roles in setting low flow areas are reversed. A. Low flow regions before changing penetrating vessel conductances. B. The low flow area after dilating venule 16. C. The low flow area after blocking venule 16. D. The low flow area after blocking venule 19. Compare A, B, C, D to Fig. 2.13A, 2.21A2, 2.21B2, 2.21B1; the low flow areas in the corresponding figures are the same.

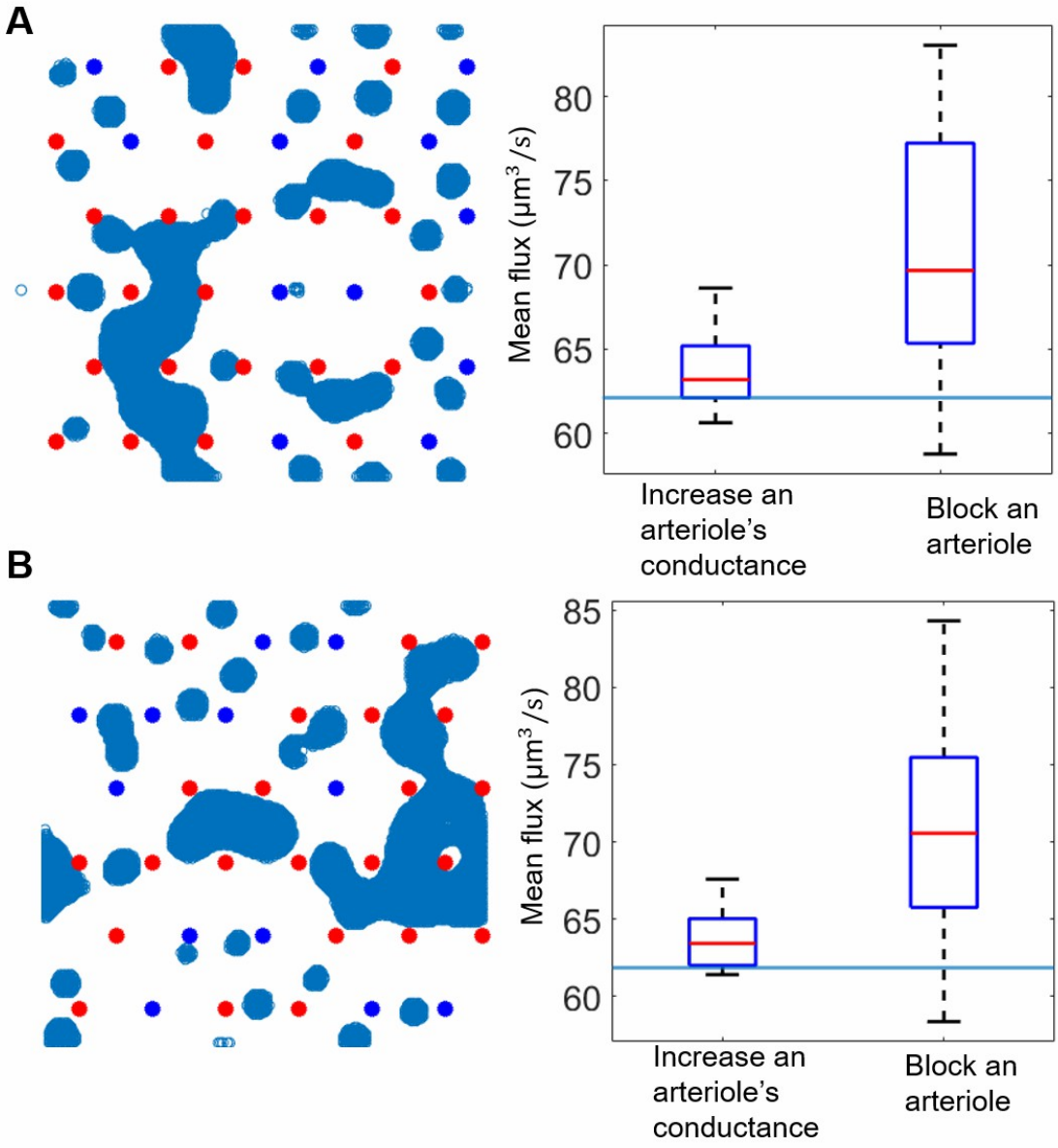

Figure 2.23: Two more examples of low flow areas and their regulation response. Arrangements of vessels do not affect conclusions about the different controllability of perfusion by arterioles versus venules. Shown: two different random arrangements of penetrating vessels with the same arteriole-venule ratio as Fig. 2.13A. For each arrangement, left panels show the low flow area before changing arteriole conductance, and right panels show the mean flux change after dilating or blocking one of all arterioles. Blue line shows the mean flux before any change. Note that for both arrangements, and just as in Fig. 2.21C, increasing some arteriole conductances decreases perfusion, while blocking many arterioles increases perfusion.

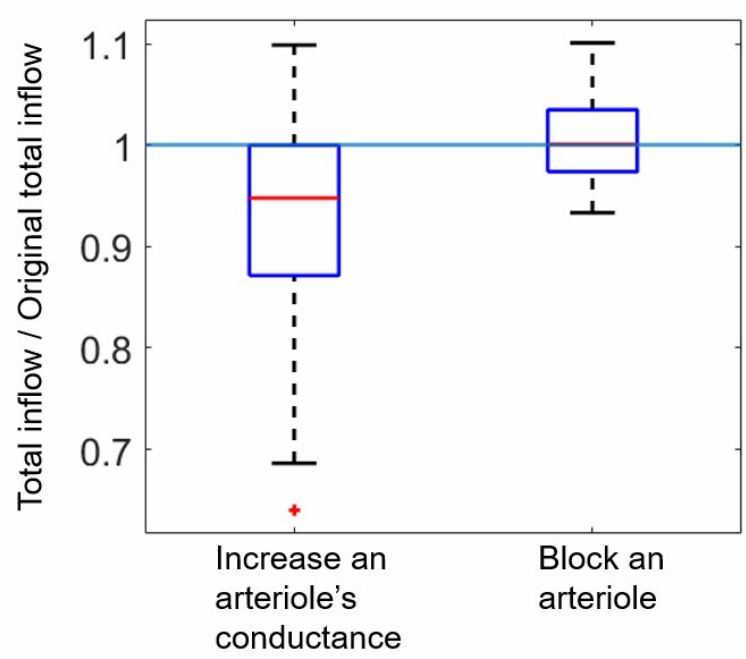

Figure 2.24: Counterpart to Fig. 2.21C, showing the effect of total inflow into the tissue (normalized by the baseline inflow) when arterioles are individually dilated or blocked. Previously, the L2-norm of q was used to quantify total perfusion through the tissue, before and after vessel conductances are perturbed. Similar results (i.e., unintuitive changes in flow) are obtained when instead plotting the effect of arteriole conductance change upon the total flow into the tissue through all penetrating arterioles.

CHAPTER 3

Microvascular Adaptation in Zebrafish Trunk: Hemodynamic-Regulation Allows Stable Growth of Microvascular Networks

Like other organisms, the development of vessels within the zebrafish is conditional on blood flow, including angiogenesis [73], specification of vessels as veins or arteries [9], and radius setting [19]. Among the endothelial cells lining blood vessels, cell migration [18] and shape and size finding [19] are shear stress responsive, providing a mechanism by which vessels may adapt their radii according to the flows that they carry. In particular, experimental evidence supports a fluid set point model, whereby vessel radii change over time to achieve a set point [20, 21]. Since fluid set points are controlled by VEGFR3 expression, different vessels may encode different set points [9].

Considerable theoretical work has tackled the question of how much of the complex geometries of real vascular networks can be recapitulated by models of shear-stress mechanotransduction. Intriguingly, a network that minimizes the cost of transport of flow between a single source and one or more sinks given constrained total volume has the same shear stress in each vessel [21], and shear-stress adaptation can produce tree (i.e., loopless) networks that minimize the energy cost of delivering fluid from a source to multiple sinks [17]. When combined with system growth, a model of adaptation to reach a fluid set point is highly competitive with other global optimization methods [74]. In this study, I am motivated by two issues with past models of fluid set points: First, shear stress set point models, as they

have previously been analyzed, are incompatible with loopy networks, tending to produce structural instabilities, in which parallel vessels are pruned down to simple paths [16]. Second, microvascular networks have not been shown to minimize the cost of transport but are consistent with other forms of optimization, for example, maximizing flow uniformity [37, 36].

A simple example shows the difficulty of programming robust network adaptation via shear stress set points. Consider the different radius adaptation trajectories of a single vessel linking a source to a sink, under two scenarios: (1) the flow through the vessel is held constant, or (2) the pressure difference between source and sink is held constant. In case (1), if the vessel radius increases, the shear stress will decrease. If, as is commonly assumed, vessel radius increase is triggered when shear stresses exceed the set point [17], the radius of the vessel will converge to a fixed value. Conversely, in case (2), increasing the vessel's radius also increases the flow it carries, so increasing the radius of the vessel increases the shear stress on the vessel wall. Hence, set point triggered growth will continue indefinitely. Accordingly, previous models for network adaptation have emphasized flow unsteadiness, due to fluctuations in the strengths of the sinks fed by the network [27, 26] or switching on and off of flows through individual small vessels [17, 75]. However, in the embryonic zebrafish, there is no evidence of widespread closing of intersegmental vessels. Conversely, [16] stabilized model networks by incorporating vascular responses to oxygen and glucose supply along with shear stresses, and by modeling communications between vessels. However, unlike shear stress induced remodeling, the underlying cellular mechanisms remain unclear. Indeed, at the stage of development considered here, the thickness of the embryo is less than the Krogh length scale, so blood flows are not indispensable to oxygen transport.

In common with other animal microvascular networks, the diameters of the finest vessels in the zebrafish trunk are comparable and even slightly smaller than the diameters of the red blood cells transported through them. Thus the model of blood as a Newtonian (or even, as a homogeneous non-Newtonian fluid, whose viscosity depends on vessel radius [76]) misses the

reality that shear stresses in real vessels are highly time-dependent, even under conditions of steady blood flow. An endothelial cell experiences the largest wall shear stress at the moment that a red blood cell passes. In this research, an adaptation model is built from the hypothesis that cells respond to the peak shear stresses rather than average shear stress. I first analyze the mathematical properties of a model based only upon peak shear stresses, showing that peak shear stress responsive networks are stable and able to maintain loops. Peak shear stress adaptation is shown to naturally produce features of flow-uniformizing networks. This first set of results is applicable to any animal vascular system that responds to peak rather than average shear stresses. Then, peak shear stress adaptation is applied to the embryonic zebrafish trunk microvasculature. I find that the peak shear stress model successfully produces uniform flows across intersegmental vessels, and that, consistent with experiments, flow uniformity is temporarily lost during a period (7-14 days post fertilization) of decline in hematocrit. Finally, my model also highlights the indispensability of the direct anastomosis of artery and vein to allow the network to adapt to reach uniform flow, which is confirmed experimentally by measuring intersegmental vessel flows following an amputation of the anastomosis-containing distal trunk.

3.1 Methodology

3.1.1 Observations: Real Intersegmental Red Blood Cell Fluxes Are Uniform From Head to Tail

The red blood cell (RBC) flow through each intersegmental artery (SeA) is measured in $N = 12$ 4 days post fertilization (dpf) embryonic zebrafish by hand counting the total number of cells passing pre-defined stations in each SeA. Zebrafish embryos were cultured in standard E3 medium supplemented with 0.05% methylene blue solution at 28.5°C, and staged from 4-7 dpf, with neutralized 0.02% tricaine solution(Sigma, MO) and mounted in 1-2% low melting agarose (Sigma-Aldrich, MO) for imaging. Each SeA vessel was recorded for

40s at 50 frames-per-second, under 10× magnification phase contrast, using a Zyla sCMOS camera on a Zeiss Axio Imager A2 microscope. For 4 dpf fish, the uniformity of RBC flux is reported in Fig. 1. Consistent with previous measurements [36], I find that at 4 dpf, although there is significant variability in flows between different intersegmental vessels (Fig. 3.1 A,B), there is no systematic bias of flow toward either head or tail (Fig. 3.1 C).

To achieve a uniform RBC flow in SeAs, SeA radii have to increase from head to tail, to compensate for the decreasing pressure along the Dorsal Aorta (DA). How tightly microvascular radii must be tuned to achieve uniform flow was tested. When each SeA vessel is assigned the same radius, I predict that the head (proximal) SeA vessels will receive a flow that is 1.65 greater than the tail (distal) vessels (Fig. 3.1 B, purple dots). This value is many folds less than previous calculations [36], due to the evening-out effects of the Zweifach-Fung effect, discussed below, but are significantly greater than that observed in real zebrafish (median ratio for 12 fish: 1.0634, Fig. 3.1 C, boxes). Mechanotransductive adaptation of SeA radii (see next segment) produces a head-to-tail ratio of 1.13, much closer to the experimental data. I probed how close real SeA radii are to optimal values that uniformly partition RBC fluxes among all SeA by starting either with all radii equal or with each vessel assigned its optimal radius calculated using [37], and then perturbing the radii by different random, relative amounts. It was found that fluxes in real fish are consistent with all vessels being within 30% of their optimal radii (Fig. 3.1 C).

3.1.2 A Stable Peak Shear Stress Set Point Model

I built a model in which vessel remodeling is regulated by the fraction of time endothelial cells exceed a threshold comparable to the peak shear stress. The flow in each vessel is modeled as follow: blood flow in microvascular vessels is laminar [77, 78], but unsteady, due to the changing pressure in the artery that feeds them. In zebrafish, Womersley numbers, measuring fluid acceleration, are low [36], and this assumption is made in all of my modeled networks. The hydraulic conductances of the vessels is modeled in the absence of RBCs using

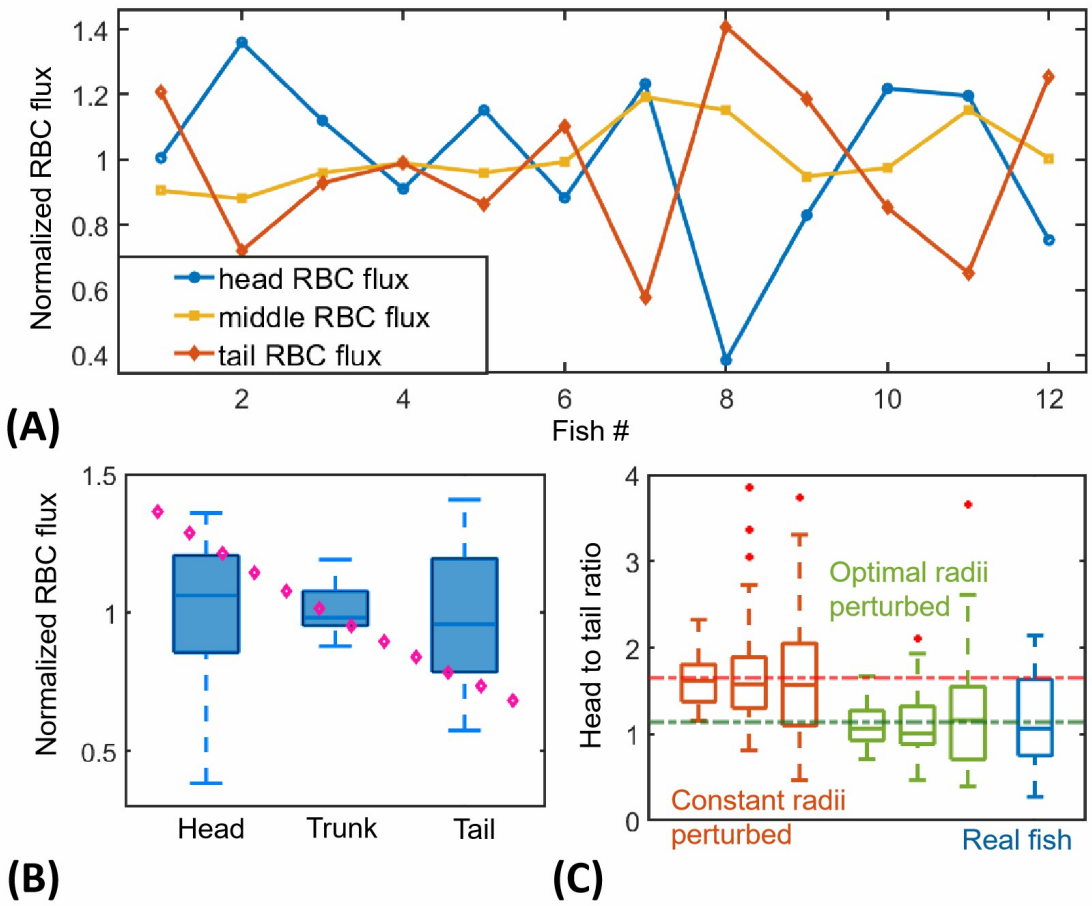

Figure 3.1: In (A) RBC fluxes (normalized so that the median flux per vessel is 1) over distal, rostral, and mid-trunk SeAs among $N = 12$ 4 dpf individuals are plotted. Each data point is pooled from 4 SeAs, taken from blue: distal (tail), red: rostral (head), and yellow: mid-trunks. Although flows are variable, no region of the trunk receives consistently greater flows. (B) Pooling data from all fish, show no differences in fluxes between the three trunk regions. In comparison, a simulated model of the fish in which all SeAs are assigned the same radius (purple dots) would have monotonically decreasing RBC flux from head to tail, due to the pressure gradient in the DA. (C) Flow uniformity requires tuning of vessel radii. I took the constant (red boxes) and optimal fish radii (green boxes, calculated using the adaptation model, see Methodology), and perturbed the modeled radii of vessels by different percentages (10, 20, and 30 percent from left to right), measuring the head to tail ratio. Data shown comes from 100 replicates at each level of perturbation. The observed uniformity in real 4dpf fish (blue box) is found to be consistent with vessel radii being within 30% of their optimum.

the Hagen-Poiseuille law [79]. Inclusion of RBCs introduces two non-Newtonian effects to my model: 1, RBC occlusion of vessels increases their flow resistance and leads to time-varying wall shear stresses that peak when an RBC passes. 2, At vessel bifurcations, RBCs are governed by the Zweifach-Fung effect; they do not divide in the ratio of the flow rates but are more likely to enter larger vessels [80].

Since RBCs move in single file in the microvessels, each vessel can be divided into segments containing RBCs or not (Fig. 3.2, lower), with respective shear stresses τ_{PSS} and τ_{NSS} (PSS stands for peak shear stress and NSS for null shear stress). For segments without RBCs, I assume the velocity profile is Poiseuille (parabolic). RBCs become highly deformed during their single-file passage through a vessel (Fig. 3.2): a moving red blood cell is separated from the vessel wall by a thin lubricating layer, thickness h, of plasma. It is assumed that h is set by a combination of elastohydrodynamics [29], and cell-cell interactions [81], and does not vary from vessel to vessel. The shear stresses in the two regions are respectively related to the mean velocity of flow, U_i, by formulae:

$$\tau_{\mathrm{NSS},i} = \frac{4\mu U_i}{r_i} \quad , \quad \tau_{\mathrm{PSS},i} = \frac{\mu U_i}{h} \ , \tag{3.1}$$

with r_i the vessel radius, $\mu = 1e-6g/(\mu m \cdot s)$ the dynamic viscosity of the plasma. I chose $h = 0.1\mu$m to produce shear stresses comparable to the set point of 5dynes/cm^2, identified in [9]. With Eqn. 3.1, a profile of the shear stress in one of the SeA vessels was obtained using experimental flow data Fig. 3.3.

For a SeA vessel i, of length L, containing n_i RBCs, and with total pressure drop ΔP_i, balancing forces gives:

$$\tau_{\mathrm{PSS},i} n_i (2\pi r_i l_i) + \tau_{\mathrm{NSS},i} (2\pi r_i (L - n_i l_i)) = \Delta P_i \pi r_i^2 \tag{3.2}$$

where l_i is the (deformed) length of each RBC, and n_i can be related to vessel hematocrit Ht_i by: $n_i = Ht_i \cdot \pi r_i^2 L/(4/3 \cdot \pi R^3)$. $R = 3\mu m$ is used as the volumetric radius of a pre-deformed

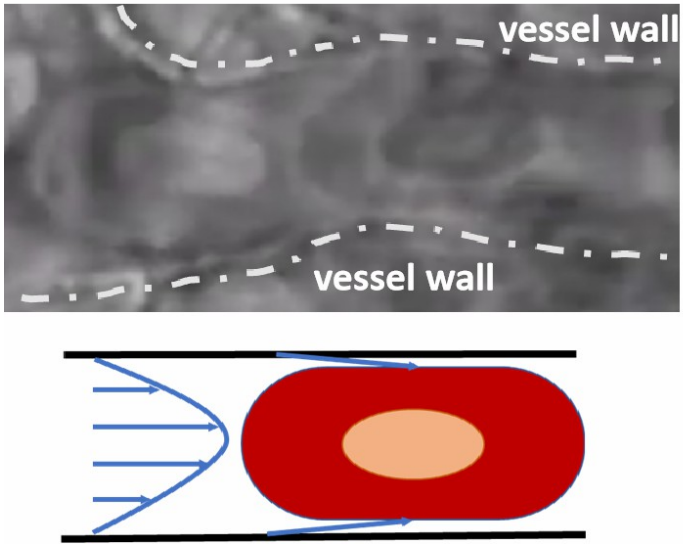

Figure 3.2: RBCs deform squeeze through vessel, dragging on the vessel walls (upper). The red blood cell inside of SeAs is modeled as a cylinder with spherical ends, and with fixed wall gap spacing $h = 0.1\mu m$, dividing the shear stress on the vessel wall into cell free (Poiseuille-profile) and cell touching (Couette-profile) regions (lower).

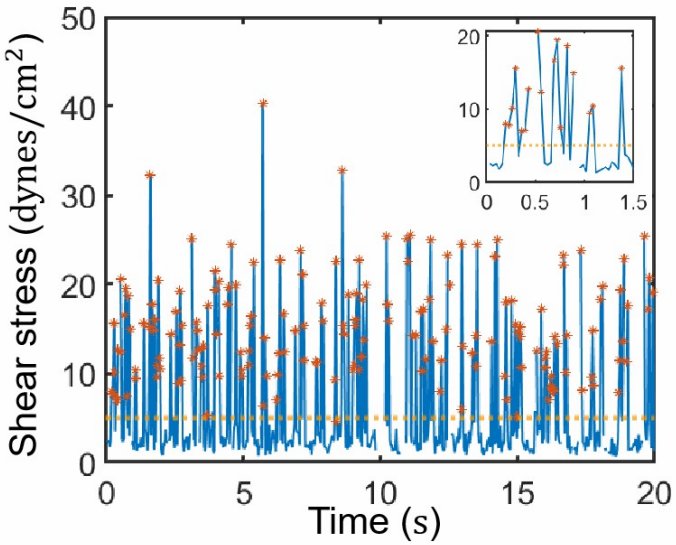

Figure 3.3: Shear stresses are measured on a single zebrafish SeA endothelial cell, based on my model of cell-cell hydrodynamics, and on 20s of RBC tracking data. Sharp spikes correspond to passages of a cell (inset shows 1.5s of data), and troughs to cell-free intervals. Only peak shear stresses exceed a typical threshold for shear stress induced cell remodeling (orange line, data taken from [9]

red blood cell. Undeformed zebrafish RBCs are ellipsoidal, with central bulges containing the cell nucleus. The precise shape of the contact region will require on the elasticity of the cell, and its orientation. I model the salient features in a semiquantitative way, by cells as spherical when undeformed, stretching into cylinders with spherical caps, when squeezing through narrow vessels. Assuming $r_i \gg h$ so gap thickness need not be considered when calculating RBC shape, the length of the cylindrical portion becomes $l_i = \frac{4}{3r_i^2}(R^3 - r_i^3)$. Assembling Eqns. 3.2 and 3.1, the wall shear stress is calculated during cell passage:

$$\tau_{\mathrm{PSS},i} = \mu \frac{U_i}{h} = \Delta P_i / \left(\frac{2n_i l_i}{r_i} + \frac{8(L - n_i l_i)h}{r_i^2} \right) \tag{3.3}$$

while the mean shear stress of the entire vessel is:

$$\tau_{\mathrm{MSS},i} = \frac{\Delta P_i \pi r_i^2}{2\pi r_i L} = \frac{\Delta P r_i}{2L} \ . \tag{3.4}$$

As with earlier models, vessel radii is assumed adapt to shear stress cues. In previous models, this shear stress cue has been assumed to be the mean shear stress, τ_{MSS}. I use such a model as a point of comparison with my models, in which peak shear stresses, τ_{PSS} instead regulate adaptation. Specifically my model for MSS-guided adaptation is:

$$\frac{dr_i}{dt} = C \left(\tau_{\mathrm{MSS},i} - \overline{\tau}_{\mathrm{MSS,i}} \right) \left(r_i - r_{\min} \right) \ . \tag{3.5}$$

where C is a constant representing the rate of adaptation, whose sign determines whether vessel radius increases ($C > 0$) or decreases ($C < 0$), when the shear stress set point $\overline{\tau}_{\mathrm{MSS}}$ is exceeded. The factor $r_i - r_{\min}$ establishes a minimum vessel radius which I set $r_{\min} = R/2$. Eqn. 3.5 is used as a null model, to be compared with a model in which peak shear stresses regulate vessel radius. Since shear stresses peak sharply during the passage of a cell, I assume that shear stress set points for each endothelial cell are exceeded when a RBC passes over it (Fig. 3.3), stress-activating the endothelial cell, and a vessel's remodeling is regulated by the

fraction of endothelial cells that are in direct contact with RBCs. Specifically I hypothesize that:

$$\frac{dr_i}{dt} = C_1(f_i - \bar{f})(r_i - r_{\min}) \ . \tag{3.6}$$

Again, C_1 is the rate of adaptation, which I assume to be positive, f_i is the fraction of stress-activated cells and $\bar{f}$ is the target fraction. Each SeA vessel is assigned the same target activation $\bar{f}$. Since τ_{PSS} is assumed to exceed the shear stress set point (Fig. 3.3), the activation fraction f_i is related to the number and length of RBCs within the vessel:

$$f_i = \frac{n_i l_i}{L} = Ht_i(1 - r_{\min}^3/R^3) \ . \tag{3.7}$$

Given the vessel radii r_i, I first calculate the equilibrium number of RBCs, and thus the fraction of PSS-activated cells, f_i in each vessel by relaxation. First, with an initial partitioning of RBCs between vessels, I can use Eqn. 3.2 to find vessel conductances, and compute the flows of whole blood into and out of each vessel by conserving flow at each bifurcation point. Assuming that each vessel is well-mixed, the flux of RBCs out of a vessel is set equal to $F_{i,\mathrm{out}}dt$ where $F_{i,\mathrm{out}} = Ht_iQ_i$ is the RBC flow rate, Q_i is the flux of whole blood, and dt is the relaxation time step. The flux into the vessel is $F_{i,\mathrm{in}}dt$, computed from the flows and hematocrit of the vessel feeding into i. For idealized networks (viz. the pair of parallel vessels, branching tree and symmetric grid networks), I assume that red blood cells divide in proportion to the blood flows at each bifurcation, hence $F_{i,\mathrm{in}} = Ht_{\mathrm{in}}Q_i$, Ht_{in} being the hematocrit in the upstream vessel before the bifurcation. In the zebrafish trunk, SeAs divert blood from a much larger vessel – the Dorsal Aorta (DA). Red blood cells are less likely to enter SeAs than it would be expected based on the ratio of flows, which is known as the Zweifach-Fung effect. A Zweifach-Fung factor is assigned, C_{ZF}, at every branching point: $F_{i,\mathrm{in}} = C_{\mathrm{ZF}}Ht_{\mathrm{in}}Q_i$. Then, the number of RBCs is updated, n_i, in each Se vessel based on the difference of $F_{i,\mathrm{in}}$ and $F_{i,\mathrm{out}}$, and the number of RBCs in DA vessels is updated using the conservation of RBC numbers at each bifurcation. I then recompute conductances and flows

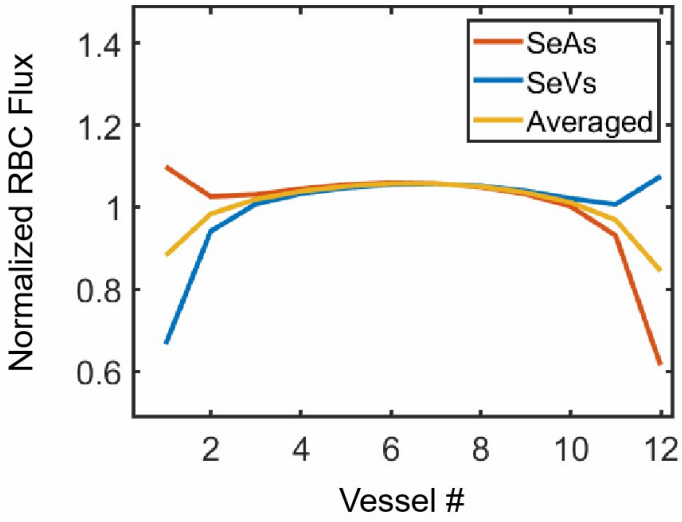

Figure 3.4: A model includes SeAs, SeVs, and DLAV produces uniform RBC flow in the trunk of the zebrafish.

using Eqn. 3.2, continuing until all hematocrits and flows have converged. Once flows and hematocrits have been computed, I update vessel radii, using an explicit discretization of Eqn. 3.6, and then recompute all hematocrits and flows. In the simulations show here, I either see convergence: $f_i \to \bar{f}$, or $r_i \to r_{\min}$, and $\frac{dr_i}{dt}$ is monitored for convergence. For the zebrafish trunk vasculature model, the network has a ladder like topology, with SeAs and SeVs (rungs) spanning between the DA and PCV (rails, Fig. 1.3). For simplicity, the network is treated as totally symmetric, neglecting the Dorsal Longitudinal Anastomotic Vessel (DLAV), which divides the flow out of each SeA between two or even more SeVs. Hence, I need model only the the arteries, and each SeA is connected to an outlet with pressure $p_0 = 0$. In a more detailed network model (Fig. 3.4), including all the intersegmental vessels and Dorsal Longitudinal Anastomotic Vessel (DLAV), the normalized RBC flux remains uniform in the middle of the trunk. The SeVs and DLAV vessels undergo the same adaptation process as the SeA vessels, and no-flow-through boundary conditions are used on both ends of the DLAV. While the boundary effect of the DLAV makes the first SeV and the last SeA have less flow, the averaged normalized RBC flux of pairs of SeA and SeV is within 1.05 and 0.85.

A pressure boundary condition $p_1 = 0.1844 mmHg$ is applied at the network inlet [82], and inflow is assigned $Ht_{\text{inflow}} = 0.2$. All SeAs are assigned the same target fraction, $\bar{f} = 0.05$, and the same Zweifach-Fung effect factor $C_{\text{ZF}} = 0.5$. My results are broadly insensitive to the particular parameters chosen (Fig. 3.5). I tested the flow uniformity using a wide range of parameters, and verified that the PSS model can produce stable zebrafish vasculatures whose flow remains uniform when tuning the inflow hematocrit (Fig. 3.5 A), number of SeAs (Fig. 3.5 B), thickness h of the plasma layer surrounding RBCs (Fig. 3.5 C), and target fraction (Fig. 3.5 D). When testing the effect of tuning each parameter, other parameters stay their default values, which are Ht = 0.2, vessel number = 12, h = 0.1m, target fraction = 0.05, and ZF factor = 0.5. Because my PSS model is sensitive to vessel hematocrit, changing of Zweifach-Fung factor has an effect on the flow uniformity, but any ZF factor that is less than 1 gives better uniformity than ZF factor = 1, which corresponds to not having Zweifach-Fung effect. When ZF factor = 1, after adaptation, every vessel still has the same hematocrit, as a result the radii of SeAs are also a constant, and the adaptation method is nullified (Fig. 3.5 F).

In addition, the chosen set of parameters gives a good fit for the vessel conductances with the experimental data [83] (Fig. 3.6). Using PSS model adaptation, flow conductances of SeA vessels obtained from Eqn. 3.2 (Fig. 3.6, blue dots) are much closer to the empirical law [83] (Fig. 3.6, blue line) than vessels given hematocrit directly without finding hematocrit using adaptation (Fig. 3.6, yellow, purple and green lines), which indicates similar distributions of hematocrit in vessels with different radii in real and PSS modeled systems.

DA and PCV are also directly connected at the tail (Fig. 1.3, C). Based on previous measurements [36], I assign this tail connection a conductance of one tenth of a normal DA segment.

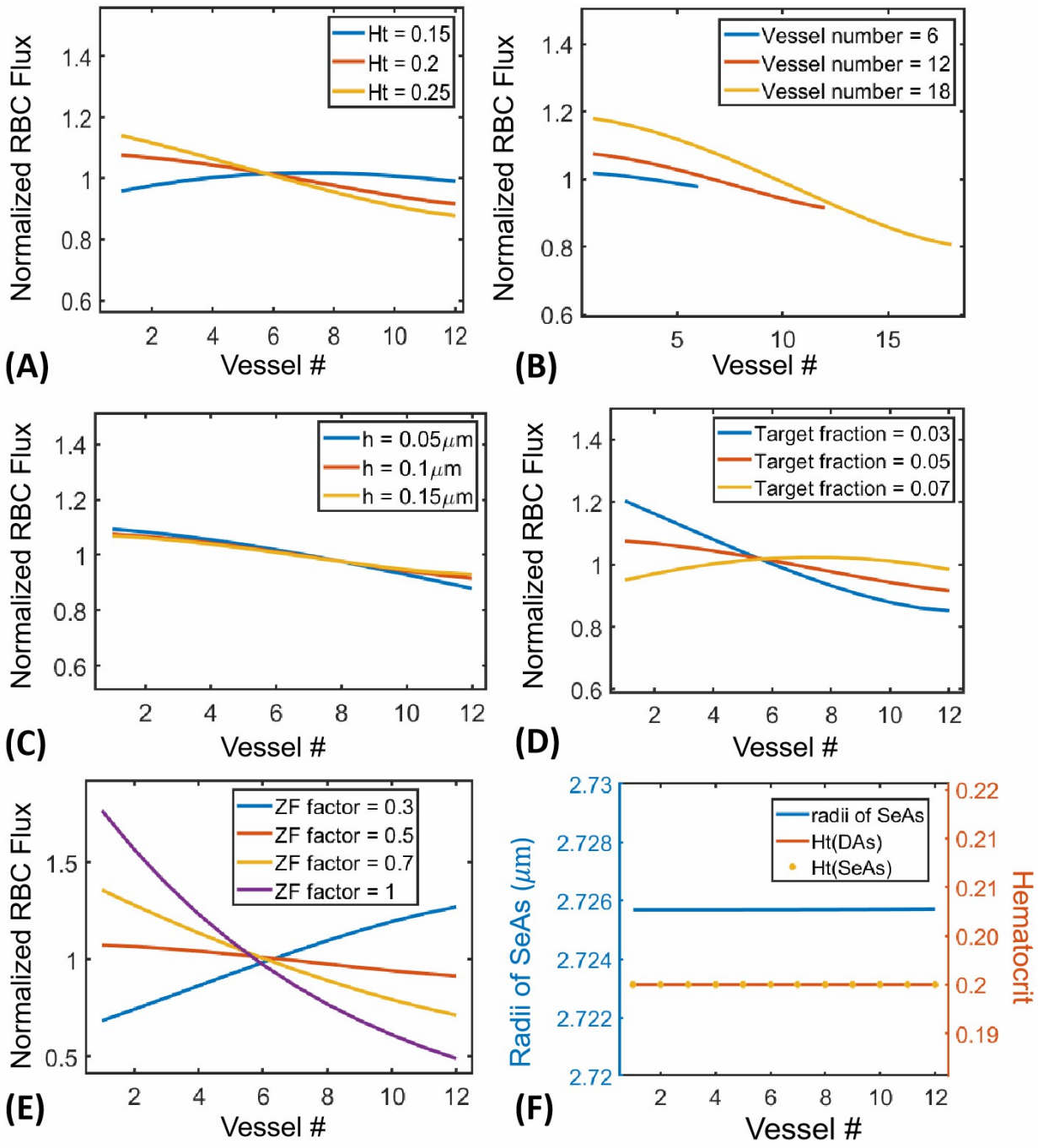

Figure 3.5: Uniformization of red blood cell flux can be achieved by PSS model using a wide range of parameter values.

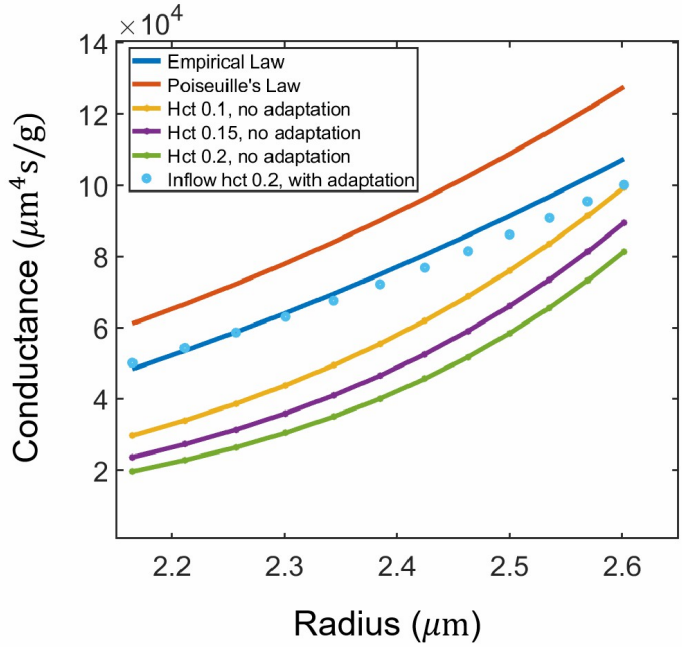

Figure 3.6: The chosen set of parameters gives a good fit for the vessel conductances with the experimental data.

3.2 Results

3.2.1 PSS-activation Model Can Stably Adapts Realistic Networks

For a single vessel of radius r, containing n RBCs, I plot the mean shear stress τ_{MSS} according to Eq. 3.4 as a function of r, if the radius is changed while holding 1, the total flow or 2, the total pressure drop, constant. If flow rates are constant then τ_{MSS} decreases with the vessel radius, whereas if pressure drop is held constant, then flow rate increases in direction proportion to radius (Fig. 3.7, blue dashed and solid curves respectively). No single model of the form Eqn. 3.5 can stabilize vessel radii under both classes of boundary condition: for example if $C > 0$ the vessel radius would converge under constant flow boundary conditions, but not if the pressure drop is constant. Conversely, changing the sign of C would stabilize the fixed pressure scenario, while destabilizing the fixed flow scenario.

The same instability is manifested when two vessels are arranged in a simple parallel

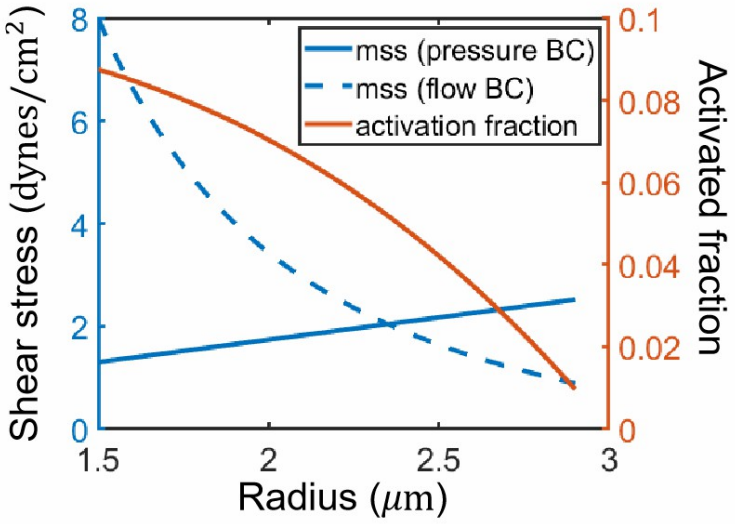

Figure 3.7: PSS leads to a consistent decline in endothelial cell activation when vessel radius is increased, whether the inflow to the vessel is pressure or flow controlled (orange curve). By contrast, MSS-cues decrease in the vessel if its radius increases under constant flow (dashed blue), but increases under constant pressure (solid blue).

network (Fig. 3.8, top) with constant inflow into the network (if pressure drop is held constant, then vessel radius adaptation is independent). If the same target MSS is assigned, $\overline{\tau}_{\mathrm{MSS}}$, to each vessel, there is one symmetric equilibrium with both vessels unpruned i.e. $r_i = r^* > r_{min}$, but this equilibrium is a saddle point under Eqn. 3.5, under a broad class of conductance-radius relationships. If the conductances of the two vessels are κ_i, then each receives a portion $\frac{Q\kappa_i}{\kappa_1+\kappa_2}$ of the total inflow, and has MSS $\tau_i = \frac{Qr_i}{2(\kappa_1+\kappa_2)}$. Hence, at the equilibrium point, the Jacobian of Eqn. 3.5 is:

$$
\begin{aligned}
J &= C\left(r^* - r_{min}\right)\begin{bmatrix} \frac{\partial \tau_1}{\partial r_1} & \frac{\partial \tau_1}{\partial r_2} \\ \frac{\partial \tau_2}{\partial r_1} & \frac{\partial \tau_2}{\partial r_2} \end{bmatrix} \\
&= \frac{CQ\left(r^* - r_{min}\right)}{2(\kappa_1+\kappa_2)^2}\begin{bmatrix} \kappa_1+\kappa_2 - r_1\frac{d\kappa_1}{dr_1} & -r_1\frac{d\kappa_2}{dr_2} \\ -r_2\frac{d\kappa_1}{dr_1} & \kappa_1+\kappa_2 - r_2\frac{d\kappa_2}{dr_2} \end{bmatrix},
\end{aligned}
\tag{3.8}
$$

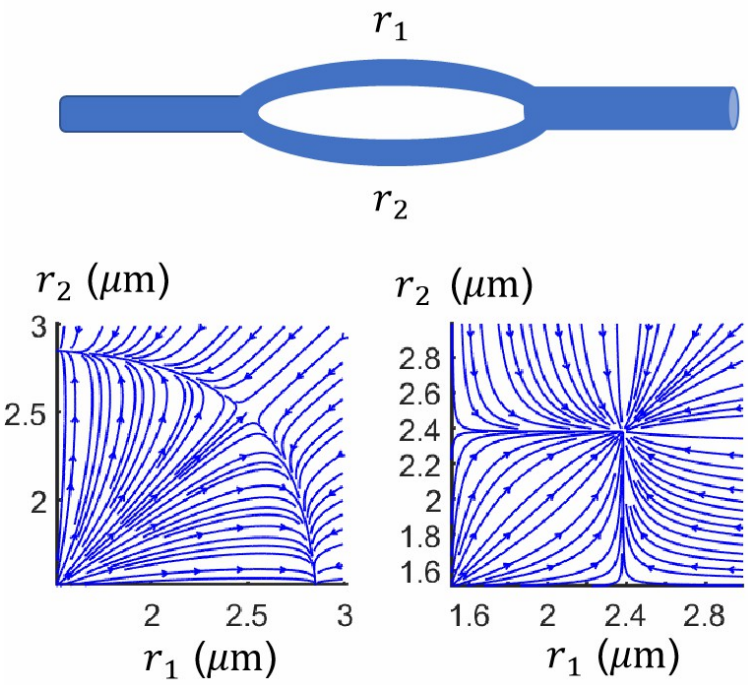

Figure 3.8: PSS-activation stabilizes vessel geometries in a single parallel loop network (top panel, schematic). The symmetric equilibrium is a saddle point under mean shear stress adaptation (bottom-left) – the network tends to evolve to a state with one vessel pruned to flow. For activation fraction mode, the symmetric equilibrium is a stable node (bottom-right).

Hence;

$$\det J = \frac{C^2 Q^2 (r^* - r_{min})^2}{4(\kappa_1 + \kappa_2)^3} \left(\kappa_1 - r_1 \frac{d\kappa_1}{dr_1} + \kappa_2 - r_2 \frac{d\kappa_2}{dr_2} \right) \tag{3.9}$$

In my, and in previous conductance models, κ is an increasing, convex function of r, with $\kappa(0) = 0$. Hence $\kappa_i - r_i \frac{d\kappa_i}{dr_i} < 0$. Hence, independently of the sign of C, $\det J < 0$ making the equilibrium a saddle point. In my model, any perturbation of the network from the equilibrium leads to one of the two vessels being pruned (Fig. 3.8, bottom-left).

I calculated the shear stresses in a real zebrafish vessel (Fig. 3.3 shows the inferred stress, given by Eq. 3.1, for a representative endothelial cell). The pulses of high shear stress mark the passage of a RBC past the cell: it can be seen that only during these pulses are stresses larger than thresholds typically identified for cellular remodeling (e.g. 5 dynes/cm^2

in [84]). It is therefore proposed that vessel remodeling is activated by the fraction of cells at peak shear stress, or, equivalently, the fraction of time each cell spends at peak shear stress (Eqn. 3.6). Setting an activation threshold that exceeds the shear stress in normal plasma flow, I find the fraction of PSS activated cells, f, decreases monotonically with vessel radius, both under conditions of constrained flow and of constrained pressure drop (Fig. 3.7, orange curve), so that vessels remodeling according to Eqn. 3.6 will converge in radius under constant pressure or constant flow boundary conditions. Parallel vessels evolve to an equilibrium point where both of the vessels have the same conductances and flows (Fig. 3.8, bottom-right).

3.2.2 PSS-activation Model Creates Uniform Red Blood Cell Flux in Zebrafish Trunk

Can Eqn. 3.6 create a realistic zebrafish trunk vasculature? First, each SeA was assigned a random radius between 2 and 3 μm. I assigned each SeA the same target fraction of PSS-activated cells: $\bar{f}$, and evolved SeA vessel radii according to Eqn. 3.6. In the absence of vessel radius adaptation, it shows a 3 fold decrease in flux from head (rostral) to tail (distal) SeAs (Fig. 3.9 A).

The amount of flow heterogeneity is smaller than reported in [37], because of the addition of the Zweifach-Fung effect in my model, but much larger than see in real zebrafish (Fig. 3.1 A,B). Fig. 3.9 B, C show the trajectories of vessel radii and flows. Assigned initially random radii, flows tend to decrease from head to tail, whether or not the Zweifach-Fung effect is modeled (Fig. 3.9 B, red and orange curves). When allowed to adapt according to Eqn. 3.6, SeA radii adapt to increase from head to tail (Fig. 3.9 C). Since all RBC transits activate cells, vessel radii are directly regulated by hematocrit, which increases from head to tail (Fig. 3.9 C, orange curves and insets), due to skimming of plasma from the DA by rostral SeAs. Distal vessels grow widest in response to having highest RBC contact, compensating for the decreasing DA pressure, and producing an almost uniform partitioning

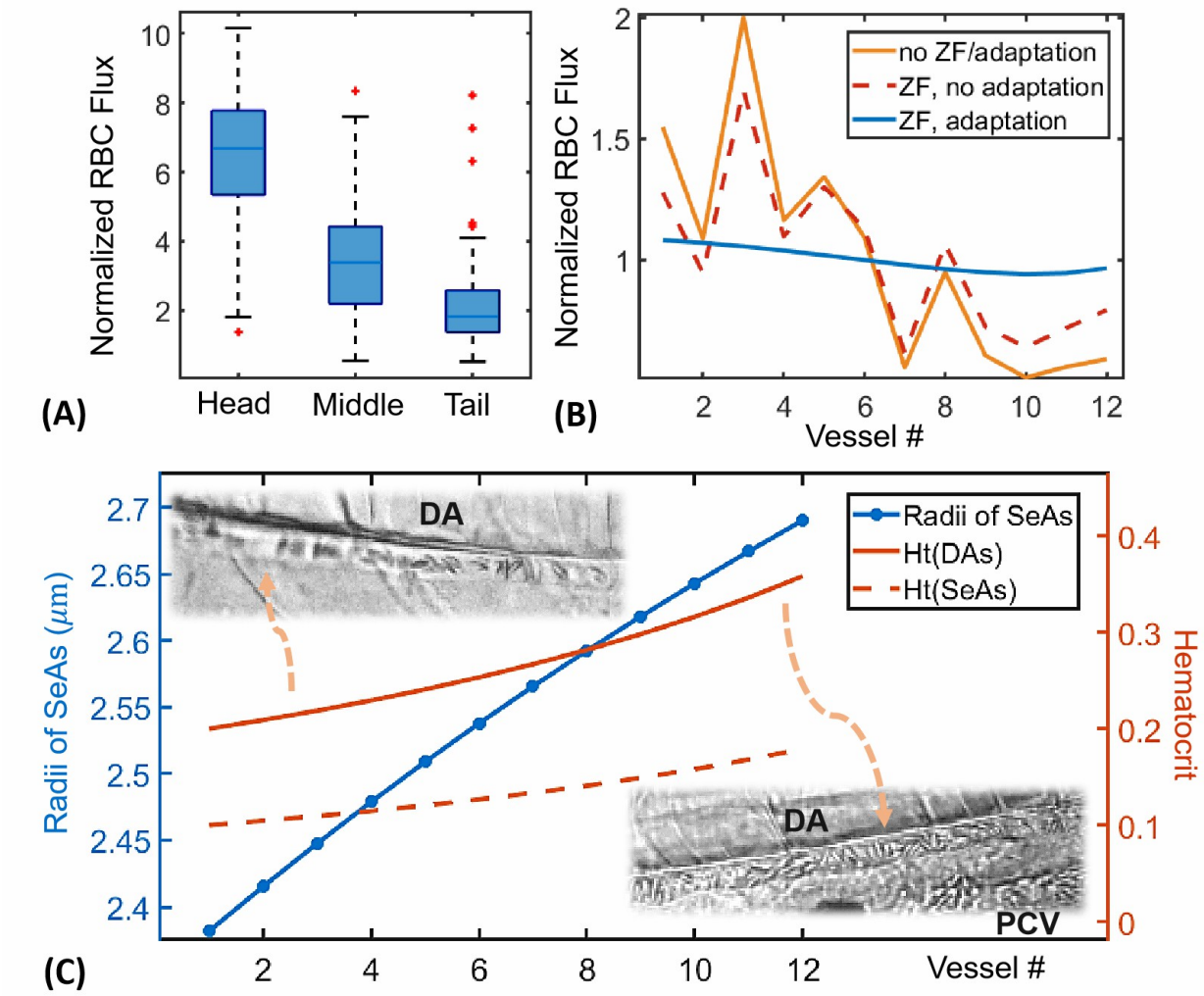

Figure 3.9: Peak Shear Stress (PSS)-adaptation can robustly adapts a model zebrafish microvascular network with 12 SeAs to achieve uniform RBC flows. (A) Initial RBC fluxes (normalized so that median flux is 1) under 100 sets of random starting radii, with variance consistent with observed variances of vessels, give statistically decreasing RBC flux of SeAs from head to tail. (B) Effect of modeled adaptation in a single fish with random initial radii. Absent Zweifach-Fung effect RBC fluxes are strongly biased toward rostral vessel (orange), though inclusion of Zweifach-Fung effect leads to increased flow in some distal SeAs (red dashed). Evolving vessel radii under Eqn. 3.6, produces highly uniform RBC fluxes across all vessels (blue line). (C) Uniformization of RBC fluxes is due to interplay of radius tuning (blue curve) and the gradient of hematocrit, Ht, in the Dorsal Aorta that feeds each intersegmental vessel. Ht increases with distance along the DA due to plasma skimming by SeAs (orange curves). Insets show the experimental images of red blood cells in two DA segments closer to head or tail. Distal SeAs respond to elevated Ht by growing wider rostral SeAs, compensating for decreasing pressure and uniformizing flows.

of RBC fluxes (Fig. 3.9 B). For the parameters chosen in Fig. 3.9, the ratio of fluxes in the 3 head-most SeAs to fluxes in the 3 tail-most SeAs is 1.1, which is close to the observed value at 4 dpf (1.06). A systematic analysis of how this ratio depends on all of the parameters in my model was perfomed: inflow hematocrit, number of SeAs, thickess of the plasma layer surrounding RBCs, target fraction, and the Zweifach-Fung ratio C_{ZF}, and similar levels of flow uniformization over a wide range of parameter values are found (Fig. 3.5).

3.2.3 Uniform Perfusion Can Not Be Maintained When Hematocrit Decreases

Although shear stress set points based on PSS are robust to the geometry of the network, vessel radii are affected by trunk hematocrit. During normal zebrafish development, there is a 3.5-fold decrease in hematocrit between 7 dpf and 15 dpf [10], potentially due to the transition from short-lived primitive red blood cells to mature, oxygen-carrying red blood cells [85]. If hematocrit in a vessel decreases then according to Eqns. 3.6, 3.7 its radius will decrease to maintain the fraction of cells in contact with RBCs. But it may not be possible for a vessel to reach the target value of f before the radius reaches $r_{\min}$, cutting off the flow of RBCs into the vessel. Having the lowest hematocrit, SeA #1 is the most vulnerable to fail to achieve $\overline{f}$ (Fig. 3.9 C, orange dash). The hematocrit in SeA #1 is always $Ht_1 = Ht_{\mathrm{inflow}} C_{\mathrm{ZF}}$ after convergence, based on my model for Zweifach-Fung effect. For the vessel to reach its target fraction of PSS activated cells, based on Eqn.3.7 there must have: $Ht_{\mathrm{inflow}} C_{\mathrm{ZF}}(1-r_{min}^3/R^3) > \bar{f}$, which I interpret as a constraint upon $Ht_{\mathrm{inflow}} > Ht_{\min} = 0.114$ with the parameters in my model here. When the hematocrit drops below this threshold, RBC flow ceases in SeA #1. Since the SeA continues to skim plasma the DA supply to SeA #2 operates with higher hematocrit, but RBC flow ceases in SeA #2 when $\frac{Q_{\mathrm{inflow}} Ht_{\mathrm{inflow}}}{Q_{\mathrm{inflow}} - Q_1}$ drops below $Ht_{\min}$. This analysis is validated through numerical experiments: slowly decreasing Ht_{inflow} in Eqn. 3.6, with the SeAs initially assigned uniform initial radii $2.5\mu m$. I initialize $Ht_{\mathrm{inflow}} = 0.12 > Ht_{\min}$, for which the activation fraction model gives near uniform flow (Fig. 3.10, blue circles).

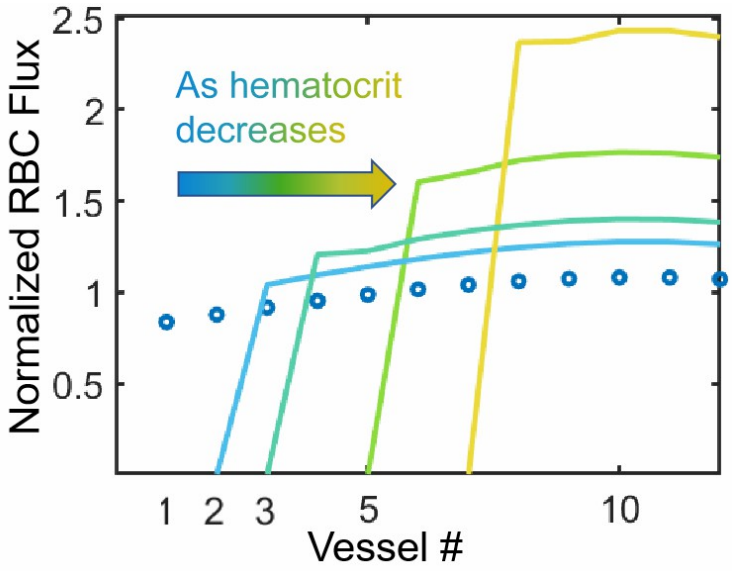

Figure 3.10: RBC fluxes under decreasing overall hematocrit is simulated, starting with an initial hematocrit of $Ht_{\text{inflow}} = 0.12$ (blue circles), and under decreasing $Ht_{\text{inflow}} = 0.11, 0.105, 0.10, 0.095$ (blue-yellow gradient). As hematocrit decreases, RBC fluxes vanish in an increasing number of rostral SeAs.

Decreasing Ht_{inflow} to $0.11 < Ht_{\text{min}}$, eliminates RBC flows in the first two SeAs (Fig. 3.10, left most line). Plasma skimming in the first two SeAs keeps means that the DA hematocrit reaching the third SeA (0.116) exceeds $Ht_{\text{min}} = 0.114$, so the third and subsequent SeAs all remain uniformly perfused (Fig. 3.10, left most line, Fig. 3.11).

All SeAs narrow from 2.4-2.7 μm radius, to around 1.5-1.9 μm radius. As I continue to decrease hematocrit more rostral SeAs lose their RBC flux and become plasma skimmers (Fig. 3.10, colored curves). My predicted pattern is observed in real zebrafish (Fig. 3.12, 3.13).

3.2.4 Uniform Perfusion of the Zebrafish Trunk Is Dependent on Arterio-Venous Anastomoses

The higher hematocrit of more distal SeAs is a key factor in maintaining uniform perfusion across the trunk, and depends on RBCs being able to remain in the DA, rather than passing

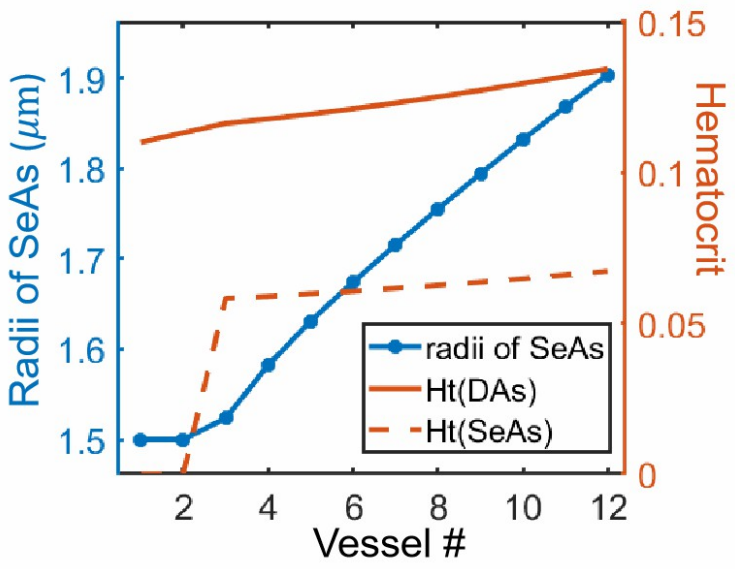

Figure 3.11: When hematocrit in DA decreases below a critical threshold of 0.114, adaptation drives vessels to their minimum radii. Plasma skimming keeps Ht above this threshold in the distal DA (solid red) and SeAs (dashed red). Radius adaptation (blue curve) creates a rostral-caudal gradient of radii that realizes uniform flow.

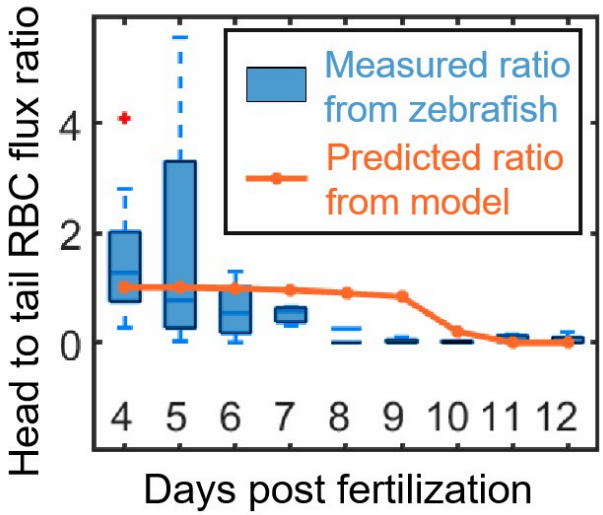

Figure 3.12: The ratio of RBC fluxes (averaged over 30s) is calculated between the 3 most rostral and 3 most distal SeAs at each of 4-9dpf ($N = 4$ fish for each day). The median head to tail ratio decreases from day 4 to day 7, reaching 0 in 9-10 dpf, consistent with PSS-adaptation (orange line). For the PSS adaptation, the inflow hematocrit is based on date from [10].

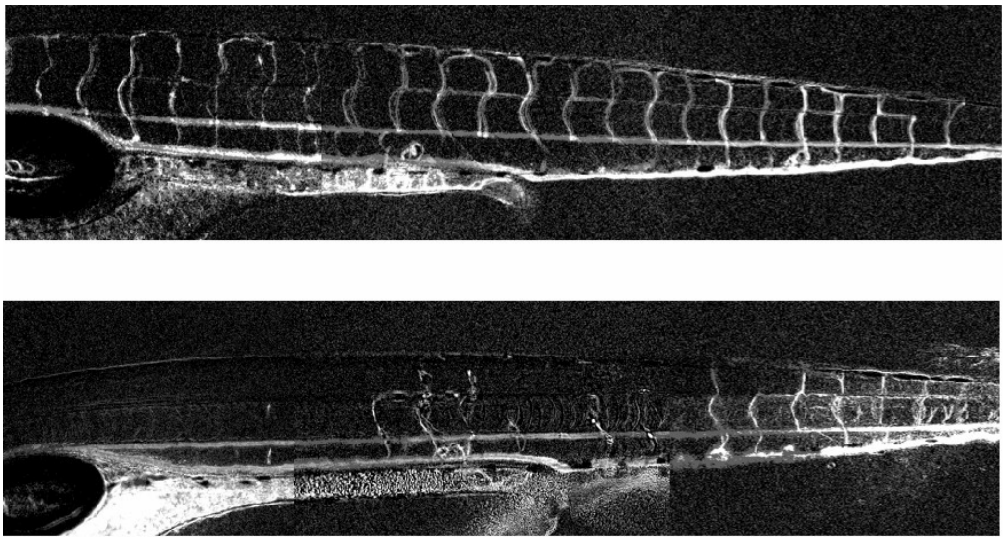

Figure 3.13: Localization of RBCs in distal vessels is observed in real zebrafish as they age from 4-12 dpf, during which hematocrit decreases 2.1-fold [10]. I superimpose a 30s sequence of phase contrast images (captured at 20fps) of 5 dpf (upper) and a 9 dpf (lower) fish, with mean intensity subtracted to remove the vessel background. RBC fluxes across RBCs are uniform at 5 dpf. At 9 dpf, fluxes are eliminated in rostral SeAs, but remain uniform in a subset of 7 caudal Se vessels.

into each SeA. The DA and PCV are connected directly at the zebrafish tail (Fig .1.3, C). Arteriovenous anastomoses (also called shunts) occur throughout the microcirculatory system; in the previous analysis of mouse cortical microvasculature based on data of [8], I found that 12 out of 27 arterioles in a $2mm^3$ volume of sensory cortex, directly connected to venules [86]. Arteriovenous anastomoses have been hypothesized to contribute to pressure regulation and flow partitioning [87], and in the skin, in thermoregulation [88]. In the zebrafish embryo, sprouts from the DA-PCV loop develop into intersegmental vessels at 2 dpf [2] and into caudal fin vascular plexus from 20-40 dpf [89], and it may not have a specific function in intermediate aged fish. Nonetheless, it diverts many ($\approx 28\%$) of RBCs that pass through the trunk away from intersegmental vessels. I tested the hypothesis that the DA-PCV anastomosis contributes to flow uniformity across SeAs, by experimentally amputating the zebrafish tail (following the methods described in [90], and by running simulations of Eqn. 3.6 with different radii of the DA-PCV anastomosis (including no anastomosis).

In my numerical study, the presence of the DA-PCV anastomosis alone, when assigned a radius consistent with experimental measurements ensured a more uniform RBC flux across SeAs than occurs in the absence of the anastomosis, and vessel radius adaptation almost perfectly equalized fluxes across RBCs (Fig .3.14, blue dashed line and green line show fluxes before and after adaptation). However, amputating the tail disrupts flow uniformity, and leads to a great increase in flow in the most distal unamputated SeA. Allowing vessel radii to adapt to the new flows actually worsens flow localization to the tail (Fig .3.14, contrasting red solid and orange dashed curves). RBCs are reluctant to enter SeAs, so SeA hematocrits are generally much smaller than the hematocrit of the DA segments that supply them (the Zweifach-Fung effect). However, this effect can occur only where the DA offers RBCs an alternative path through the trunk that avoids entering SeAs. RBCs reaching the last SeA must enter that vessel, so hematocrit in the last SeA matches that of the DA, endowing it with a much greater hematocrit and thus flow rate), than other SeAs. Suppression of the Zweifach-Fung effect leads to a sharp increase of hematocrit, and thus RBC flux in the last SeA (3.14, orange dashed line). Radius adaptation then exacerbates flow localization, since a large fraction of the SeA is PSS activated, leading this last SeA to increase its radius from $2.56\mu m$ to $2.92\mu m$, further increasing the portion of trunk RBC flow that the last SeA receives (3.14, red solid line).

Experimental observations of post-amputation flows support my quantitative predictions. Waiting 1 day post amputation to allow bleeding to end and inflammation diminish, I observed RBC flows far from and close to the amputation site (a long exposure image is shown by red fluorescence in Fig. 3.15). Hematocrit in the SeA closest to the amputation site is 3-10 fold larger than in more rostral SeAs.

When decreasing the radius of the DA-PCV anastomosis from equal to the DA radius, to equal to the last SeA radius (equivalence of tail amputation), the hematocrit in the last SeA would get higher and higher, as a result the head to tail RBC flux ratio decreases (Fig. 3.16, blue line), and there is an optimal anastomosis radius that makes head to tail BC flux

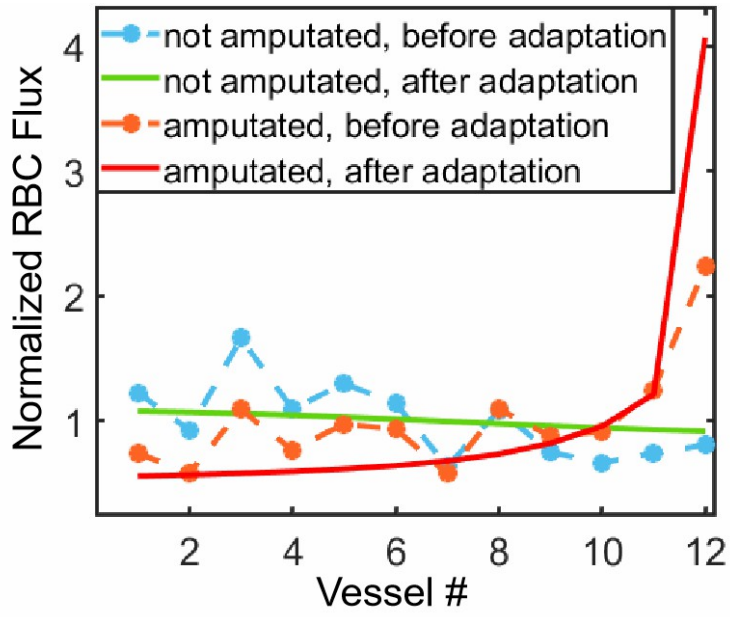

Figure 3.14: Given random initial radii (taken from Fig. 3.9B), RBC fluxes (normalized to median is 1) is simulated under adaptation of vessel radii, with and without the DA-PCV anastomosis. If anastomosis is present, adaptation uniformizes flow (compare green and blue curves). Removal of the tail causes a sharp spike in flux in the distal SeA (orange dashed curve), that is increased by adaptation (red solid curve).

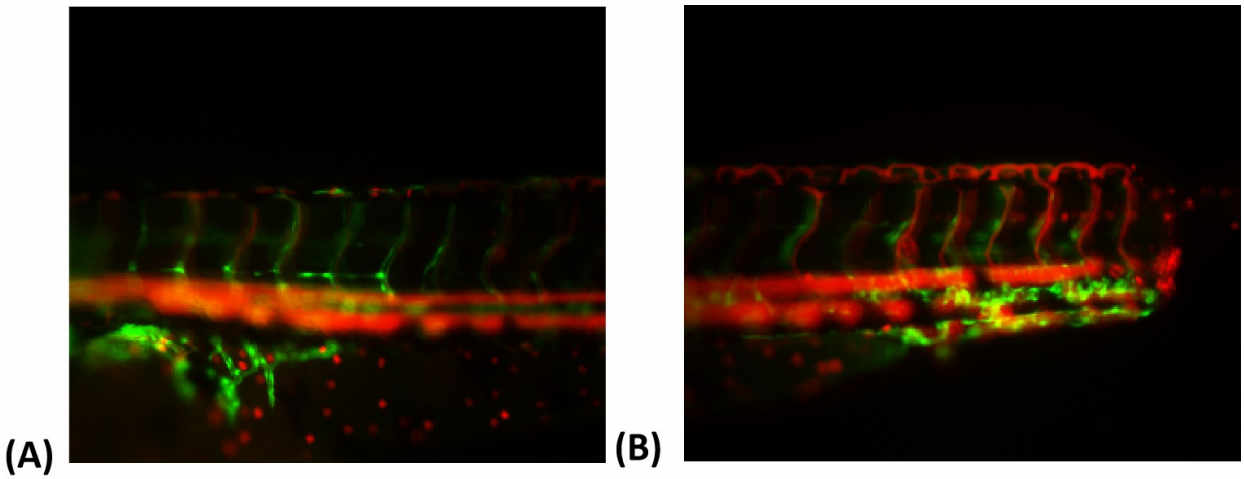

Figure 3.15: Localization of blood flow is seen in a 5dpf transgenic *Tg(fli1:eGFP; Gata1:dsred)* zebrafish, 1 day post amputation (methods from [11]). GFP-labelled endothelial cells visualize microvessels. DsRed channel data from 60s of images is superimposed, captured at a frame rate of 33fps. Distal SeAs (B) have far greater RBC flux that rostral SeAs (A), due to a 1.87-fold increase in hematocrit.

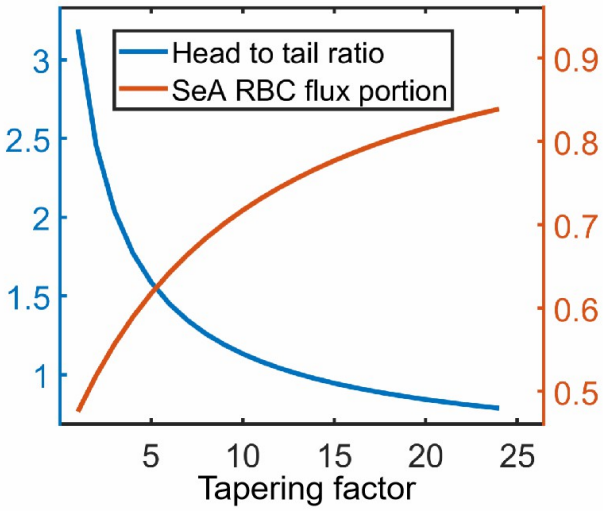

Figure 3.16: As the tapering factor (the ratio of conductance between a DA segment and the DA-PCV anastomosis) increases, even though more portion of RBC flux goes into the SeA vessels instead of being shunted by the anastomosis (orange line), the head to tail red blood cell flux ratio would decrease (blue line). The ratio is closest to 1 when the tapering factor is 13.

ratio closest to 1. This radius (tapering factor = 13) is close to what I have been using in the PSS model (tapering factor = 10).

3.3 Discussion

My focus on Peak Shear Stress regulated growth is motivated by 1. the challenge of explaining how endothelial cell responses to shear stress may be sufficient to create stable networks of vessels, and 2. estimates of endothelial cell stresses that show that only peak shear stresses, occurring when an RBC transits through the vessel, exceed typical values given for shear stress set points. The model for peak shear stress activated vessel radius adaptation stably converges on model networks, and leads to uniform perfusion of intersegmental vessels when used to model the zebrafish trunk microvasculature. PSS activation does not require that vessels be supplied with additional information, e.g., due to their glucose or oxygen supply, but it does mean that vessel remodeling is triggered in response to changes in hematocrit,

consistently with my observations in 4-7 dpf zebrafish. Indeed, since mean shear stresses in a vessel are controlled by the pressure drop along the vessel, and cardiac activity is maintained from 4-7 dpf [91], it would be expected pressure drops and therefore mean stresses to be preserved, precluding the type of vessel remodeling and flow redistribution predicted by my model and seen in real zebrafish.

Modeling of the zebrafish trunk shows that a direct connection between DA and PCV is indispensable to achieving uniform perfusion, and in the absence of the anastomosis, flows would be severely localized to the most distal SeAs, which is confirmed by amputation experiments. The DA-PCV anastomosis plays a future role in the development of the caudal fin vascular plexus, so this insight does not necessarily explain its presence in the 4 dpf zebrafish. Yet with more than a quarter of RBCs that pass through the trunk not entering the finest vessels, the assumption that vascular networks minimize the cost of transport is likely to not be borne out at this scale. The analogous topology of vessels in the zebrafish hindbrain may provide additional evidence that anastomoses are necessary for hemodynamic regulation of vessel radii. The zebrafish hindbrain is topologically similar to the trunk vasculature, with the Basilar Artery supplying a rung-like system of vertebral arteries. Like the DA-PCV connection, the Basilar Artery anastomoses directly with the rostral intersegmental vessels, allowing RBCs to circumvent the vertebral arteries. Interestingly, the anastomosis is not a vestige of angiogenesis: the Basilar Artery forms from sprouts that develop from the Primordial Hind Brain Channels, and thus, is capable of carrying flow even before its anastomosis with the intersegmental vessels.

Although I use amputation here to explore the hemodynamic effect of the DA-PCV anastomosis, localization of blood flow to SeAs proximal to the amputation site hints at one possible resolution for how hemodynamic stresses can increase following damage to a vascular network, since the damage is expected to reduce flows [90].

Other than the hematocrit, the activation fraction of vessels is also affected by other features of blood's complex rheology – most obviously the Fahraeus effect (which influences

wall-cell spacings). My model phenomenologically incorporates the effect, which is incompletely understood, despite a lot of investigation [92, 93, 94, 95, 96, 97]. However, the model could still produce qualitatively correct results and provide intuitive physical explanations for different hemodynamic phenomena.

My model provides theoretical guidance on creating microvascular networks with uniform flows, using only hemodynamic cues, as demonstrated by its stability in idealized networks, and in a model of the real zebrafish trunk. Fundamental experiments on blood flow and mathematical modeling have illuminated the mechanics of red blood cell-vessel wall near contacts, and the mechanics of red blood cells dividing at vessel branching points. These data do not exist for the zebrafish microcirculation, and ongoing efforts to collect them will likely lead to a revision of the quantitative details of my models. In particular, the model makes definitive predictions about the role played by the rostral-caudal gradient of hematocrit in the DA, predictions that are qualitatively supported by my observational data (Fig. 3.9 C), and in quantitative accord with hematocrit gradient measurements in other organisms [98, 99]. However, high-speed imaging of the DA would provide a quantitative test of the role it plays in uniformizing perfusion. I also note that in my images of the caudal DA, red blood cells appear closely packed (Fig. 3.9 C, insets). For some choices of parameters, the model predicts hematocrits within the DA that reach, and are capped by, the maximum close packing hematocrit, disrupting uniformity of perfusion. Avoiding close packing may provide an alternative explanation of the minimum radius of the anastomosis.

Finally, I note that although my model has been tested on the zebrafish microvascular network, uniformity of perfusion has emerged as an organizing principle in more topologically complex networks, such as the cortical vasculature [8, 86]. Future studies will reveal whether hemodynamics are sufficient to explain new data streams on vessel radii in these geometrically and physiologically rich networks. Importantly, in constructing networks, each Se-vessel is assigned the same activation set point $\bar{f}$. In fact, shear stress set points can be minutely controlled via VEGFR3 expression levels. Whether, where, and how this additional degree

of freedom is used, will become clear when the model is used on emerging streams of data on microvascular network geometries and flows. It would be highly interesting to see whether the same target fraction tuning is possible or needed in other parts of the zebrafish's circulatory system. In topologically complex networks, such as the brain [8], physiological demands such as for oxygen or glucose may tune the target activation fraction [16].

CHAPTER 4

Summary and Significance

As the seat of consciousness, our brain may be the most mysterious and captivating organ. Although many of us are aware of the complex synaptic circuits that provide the seat to the brain's computational powers, it is rather less well appreciated that it is also a hydraulic organ that must be kept minutely perfused with blood to sustain its constant demand for oxygen and glucose, since it lacks any ability to store glucose. In the cortex, this supply is maintained by parallel arterioles and venules. Shortfalls in perfusion are increasingly implicated in disease and aging-related damage.

How efficient is this vasculature of such significance to perfuse blood flow, and how well can it control the change of demand in blood flow? Specifically, how does the specific structure, i.e., parallel arterioles and venules with consistent arterio-venous ratio (or the inverse) across different mammalian cortices, affect the perfusion efficiency? In order to highlight the function of parallel penetrating vessels – capillary bed structure, and in the meantime, simplify the calculation process, I model cerebral vasculature by a slender-body approximation that discretely represents higher-level network elements including venules and arterioles, while treating the capillary bed between these elements as a continuum. My model provides appropriate resolution for many complex microvascular networks, where capillary level data may be incomplete or of uncertain resolution.

Although the novelty of this study is rooted in the modeling framework, the central result is quite simply stated: between any pair of arterioles, or any pair of venules, there must be a 'dead zone' where flows almost cancel, and the perfusive efficiency is constrained

by the existence of these low flow regions in the cortical vasculature. These regions can be kept small by carefully arranging vessels in regular, ordered lattices. However, in the real brain, penetrating vessels form all at once, and from a disordered surface network, having no luxury of making a regular penetrating network. Absent this control, the low flow regions can be controlled only by optimizing the ratio of arterioles to venules (or its converse), and different animals, mice, men, and monkeys, show remarkable conformance to this optimal ratio. The low flow regions depend on the geometrical arrangement of penetrating arterioles and venules, as well as their conductances. As a result, the low flow regions are shaped in complex ways by changes in vascular conductance, creating geometric challenges for the hydraulic control of cortical perfusion.

The cerebral vasculature is modeled as a steady state without changing its topology or hydraulic conductance, which simplifies reality. Hundreds to billions of capillaries enable red blood cells to deliver oxygen throughout the body; instead of maintaining their radii after vessel formation, capillaries' growth is a dynamic process, and vessel radii constantly tune themselves by responding to blood flow shear stresses. However, an adaptation model for a vascular network on cerebral scale has yet been proposed; in fact, an adaptation method for tuning vessel radii is lacking for any realistic vascular system with loops. Considering it would be extremely computationally expensive, and lacking experimental data, if the cerebral vasculature was used to study the adaptation principles of the microvascular networks, I use a more accessible animal model – zebrafish trunk vasculature.

The development of vessels is known to be conditional on blood flow characteristics, especially blood flow shear stresses ([9]), as experiments in mice and zebrafish demonstrated. However, past numerical models of shear-stress mechanotransduction based on the mean shear stress set point method could produce tree networks, but have been mathematically proven to create unstable networks which prune the network to simple paths, and it has therefore become widely accepted that shear stresses alone are insufficient to produce the complex, loopy networks seen in real animals ([16]). This has in fact led to a division

between biologists who gave focus on the role of wall shear stress in setting vessel radii, and physicists and applied mathematicians who have regarded steady shear stresses as providing insufficient information to regulate vessel growth, and have sought to resolve this paradox by adding addition cues, such as oxygen cues, or unsteady flows, for which there is, at present scant supporting biological data. This study shows that blood flow hydrodynamics alone is sufficient information for the endothelial cells to adapt the vessel radius and generate stable networks.

A model that peak shear stresses regulate the adaptation is used, which I show allows the stable growth of realistic networks with loops. Since shear stresses peak when a red blood cell passes, the model is sensitive to the hematocrit level, thus with the combination of the Zweifach-Fung effect, which forms a hematocrit gradient throughout the vasculature, it is able to modulate vessel radii accordingly, and creates a zebrafish microvascular network that produces uniform red blood cell flux at 4 day post fertilization (dpf), while predicts a localized distribution of red blood cell flux at 12 dpf when the hematocrit reduced by half, which was unexplained previously. The model also reveals a new purpose of the artery-vein anastomosis, without which the red blood cells would be congesting the most distal intersegmental vessel. All modeled patterns of red blood cell flux distribution are supported by my experimental observations. By not enforcing a global optimization goal, such as optimizing uniformity, the network is able to adapt under different circumstances and show realistic shifts in the distribution of red blood cell flux.

My studies on cerebral vasculature structure and zebrafish trunk vessel adaptation have provided new tools to model these systems with stable convergence and reasonable computation time, but replicating reality with complicated models that consider every detail is not the purpose. Instead, models that emphasize key characteristics, and are, in afterthought, intuitive, are used to reveal fundamental principles of network structure and vessel adaptation and, in turn, explain phenomenons those confused biologists for decades.

ACKNOWLEDGMENTS

I acknowledge financial support from National Institute of General Medical Sciences under award 5R01GM126556.

The research on the mammalian cerebral micovasculature is published under PNAS ([86]), and the study of zebrafish embryo trunk microvasculature adaptation is currently under peer review through PNAS.

REFERENCES

[1] Steven A Vokes and Paul A Krieg. Molecular vascular embryology. In *Pan Vascular Medicine*, pages 18–35. Springer, 2002.

[2] Sumio Isogai, Masaharu Horiguchi, and Brant M Weinstein. The vascular anatomy of the developing zebrafish: an atlas of embryonic and early larval development. *Developmental biology*, 230(2):278–301, 2001.

[3] Andreas Linninger, Grant Hartung, Shoale Badr, and Ryan Morley. Mathematical synthesis of the cortical circulation for the whole mouse brain-part i. theory and image integration. *Computers in biology and medicine*, 110:265–275, 2019.

[4] Wahbi K El-Bouri and Stephen J Payne. A statistical model of the penetrating arterioles and venules in the human cerebral cortex. *Microcirculation*, 23(7):580–590, 2016.

[5] Daniel L Adams, Valentina Piserchia, John R Economides, and Jonathan C Horton. Vascular supply of the cerebral cortex is specialized for cell layers but not columns. *Cerebral Cortex*, 25(10):3673–3681, 2015.

[6] Andy Y Shih, Pablo Blinder, Philbert S Tsai, Beth Friedman, Geoffrey Stanley, Patrick D Lyden, and David Kleinfeld. The smallest stroke: occlusion of one penetrating vessel leads to infarction and a cognitive deficit. *Nature neuroscience*, 16(1):55, 2013.

[7] John Nguyen, Nozomi Nishimura, Robert N Fetcho, Costantino Iadecola, and Chris B Schaffer. Occlusion of cortical ascending venules causes blood flow decreases, reversals in flow direction, and vessel dilation in upstream capillaries. *Journal of Cerebral Blood Flow & Metabolism*, 31(11):2243–2254, 2011.

[8] Pablo Blinder, Philbert S Tsai, John P Kaufhold, Per M Knutsen, Harry Suhl, and David Kleinfeld. The cortical angiome: an interconnected vascular network with noncolumnar patterns of blood flow. *Nature neuroscience*, 16(7):889, 2013.

[9] Nicolas Baeyens, Stefania Nicoli, Brian G Coon, Tyler D Ross, Koen Van den Dries, Jinah Han, Holly M Lauridsen, Cecile O Mejean, Anne Eichmann, Jean-Leon Thomas, et al. Vascular remodeling is governed by a vegfr3-dependent fluid shear stress set point. *Elife*, 4:e04645, 2015.

[10] Thorsten Schwerte, Dietmar Überbacher, and Bernd Pelster. Non-invasive imaging of blood cell concentration and blood distribution in zebrafish danio rerio incubated in hypoxic conditions in vivo. *Journal of Experimental Biology*, 206(8):1299–1307, 2003.

[11] Mehrdad Roustaei, Kyung In Baek, Zhaoqiang Wang, Susana Cavallero, Sandro Satta, Angela Lai, Ryan O'Donnell, Vijay Vedula, Yichen Ding, Alison Lesley Marsden, et al.

Computational simulations of the 4-d micro-circulatory network in zebrafish tail amputation and regeneration. *bioRxiv*, 2021.

[12] Lia Papadopoulos, Pablo Blinder, Henrik Ronellenfitsch, Florian Klimm, Eleni Katifori, David Kleinfeld, and Danielle S Bassett. Comparing two classes of biological distribution systems using network analysis. *PLoS computational biology*, 14(9):e1006428, 2018.

[13] Pablo Blinder, Andy Y Shih, Christopher Rafie, and David Kleinfeld. Topological basis for the robust distribution of blood to rodent neocortex. *Proceedings of the National Academy of Sciences*, 107(28):12670–12675, 2010.

[14] Chris B Schaffer, Beth Friedman, Nozomi Nishimura, Lee F Schroeder, Philbert S Tsai, Ford F Ebner, Patrick D Lyden, and David Kleinfeld. Two-photon imaging of cortical surface microvessels reveals a robust redistribution in blood flow after vascular occlusion. *PLoS biology*, 4(2):e22, 2006.

[15] Keiichiro Maeda, Ryuji Hata, Michael Bader, Thomas Walther, and Konstantin-Alexander Hossmann. Larger anastomoses in angiotensinogen-knockout mice attenuate early metabolic disturbances after middle cerebral artery occlusion. *Journal of Cerebral Blood Flow & Metabolism*, 19(10):1092–1098, 1999.

[16] AR Pries, TW Secomb, and P Gaehtgens. Structural adaptation and stability of microvascular networks: theory and simulations. *American Journal of Physiology-Heart and Circulatory Physiology*, 275(2):H349–H360, 1998.

[17] Dan Hu and David Cai. Adaptation and optimization of biological transport networks. *Physical review letters*, 111(13):138701, 2013.

[18] Yi Jin, Lars Muhl, Mikhail Burmakin, Yixin Wang, Anne-Claire Duchez, Christer Betsholtz, Helen M Arthur, and Lars Jakobsson. Endoglin prevents vascular malformation by regulating flow-induced cell migration and specification through vegfr2 signalling. *Nature cell biology*, 19(6):639–652, 2017.

[19] Wade W Sugden, Robert Meissner, Tinri Aegerter-Wilmsen, Roman Tsaryk, Elvin V Leonard, Jeroen Bussmann, Mailin J Hamm, Wiebke Herzog, Yi Jin, Lars Jakobsson, et al. Endoglin controls blood vessel diameter through endothelial cell shape changes in response to haemodynamic cues. *Nature cell biology*, 19(6):653–665, 2017.

[20] Nicolas Baeyens, Chirosree Bandyopadhyay, Brian G Coon, Sanguk Yun, and Martin A Schwartz. Endothelial fluid shear stress sensing in vascular health and disease. *The Journal of clinical investigation*, 126(3):821–828, 2016.

[21] Simon Rodbard. Vascular caliber. *Cardiology*, 60(1):4–49, 1975.

[22] Peter Lennie. The cost of cortical computation. *Current biology*, 13(6):493–497, 2003.

[23] Jeremy M Berg. Biochemistry 5th edition, 2006.

[24] Gerald A Dienel. Brain glucose metabolism: integration of energetics with function. *Physiological reviews*, 99(1):949–1045, 2019.

[25] ZiMian Wang, Zhiliang Ying, Anja Bosy-Westphal, Junyi Zhang, Britta Schautz, Wiebke Later, Steven B Heymsfield, and Manfred J Müller. Specific metabolic rates of major organs and tissues across adulthood: evaluation by mechanistic model of resting energy expenditure. *The American journal of clinical nutrition*, 92(6):1369–1377, 2010.

[26] Eleni Katifori, Gergely J Szöllősi, and Marcelo O Magnasco. Damage and fluctuations induce loops in optimal transport networks. *Physical review letters*, 104(4):048704, 2010.

[27] Francis Corson. Fluctuations and redundancy in optimal transport networks. *Physical Review Letters*, 104(4):048703, 2010.

[28] Marc Durand. Structure of optimal transport networks subject to a global constraint. *Physical Review Letters*, 98(8):088701, 2007.

[29] Thierry Savin, MM Bandi, and L Mahadevan. Pressure-driven occlusive flow of a confined red blood cell. *Soft matter*, 12(2):562–573, 2016.

[30] Ilse Geudens, Baptiste Coxam, Silvanus Alt, Véronique Gebala, Anne-Clémence Vion, Katja Meier, Andre Rosa, and Holger Gerhardt. Artery-vein specification in the zebrafish trunk is pre-patterned by heterogeneous notch activity and balanced by flow-mediated fine-tuning. *Development*, 146(16):dev181024, 2019.

[31] Qi Chen, Luan Jiang, Chun Li, Dan Hu, Ji-wen Bu, David Cai, and Jiu-lin Du. Haemodynamics-driven developmental pruning of brain vasculature in zebrafish. 2012.

[32] Eva Kochhan, Anna Lenard, Elin Ellertsdottir, Lukas Herwig, Markus Affolter, Heinz-Georg Belting, and Arndt F Siekmann. Blood flow changes coincide with cellular rearrangements during blood vessel pruning in zebrafish embryos. *PloS one*, 8(10):e75060, 2013.

[33] Kyung In Baek, Shyr-Shea Chang, Chih-Chiang Chang, Mehrdad Roustaei, Yichen Ding, Yixuan Wang, Justin Chen, Ryan O'Donnell, Hong Chen, Julianne W Ashby, Xiaolei Xu, Julia J Mack, Susana Cavallero, Marcus Roper, and Tzung Hsiai. Vascular injury remodels vessel topology to partition blood flow for peak wall shear stress to restore embryonic circular network. to appear in Front. cardiovasc. med, 2022.

[34] Ferdinand Le Noble, Delphine Moyon, Luc Pardanaud, Li Yuan, Valentin Djonov, Robert Matthijsen, Christiane Bréant, Vincent Fleury, and Anne Eichmann. Flow regulates arterial-venous differentiation in the chick embryo yolk sac. 2004.

[35] Nathan D Lawson and Brant M Weinstein. In vivo imaging of embryonic vascular development using transgenic zebrafish. *Developmental biology*, 248(2):307–318, 2002.

[36] Shyr-Shea Chang, Shenyinying Tu, Kyung In Baek, Andrew Pietersen, Yu-Hsiu Liu, Van M Savage, Sheng-Ping L Hwang, Tzung K Hsiai, and Marcus Roper. Optimal occlusion uniformly partitions red blood cells fluxes within a microvascular network. *PLoS computational biology*, 13(12):e1005892, 2017.

[37] Shyr-Shea Chang and Marcus Roper. A gradient descent method for optimization of model microvascular networks. *arXiv preprint arXiv:1709.09340*, 2017.

[38] Derek B Ingham and Ioan Pop. *Transport phenomena in porous media*. Elsevier, 1998.

[39] Sylvie Lorthois and Francis Cassot. Fractal analysis of vascular networks: insights from morphogenesis. *Journal of theoretical biology*, 262(4):614–633, 2010.

[40] Felix J Meigel and Karen Alim. Flow rate of transport network controls uniform metabolite supply to tissue. *Journal of The Royal Society Interface*, 15(142):20180075, 2018.

[41] GK Batchelor. Slender-body theory for particles of arbitrary cross-section in stokes flow. *Journal of Fluid Mechanics*, 44(3):419–440, 1970.

[42] Joseph B Keller and Sol I Rubinow. Slender-body theory for slow viscous flow. *Journal of Fluid Mechanics*, 75(4):705–714, 1976.

[43] Timothy W Secomb. A green's function method for simulation of time-dependent solute transport and reaction in realistic microvascular geometries. *Mathematical medicine and biology: a journal of the IMA*, 33(4):475–494, 2016.

[44] Ettore Vidotto, Timo Koch, Tobias Köppl, Rainer Helmig, and Barbara Wohlmuth. Hybrid models for simulating blood flow in microvascular networks. *Multiscale Modeling & Simulation*, 17(3):1076–1102, 2019.

[45] Dominic Jordan, Peter Smith, and Peter Smith. *Nonlinear ordinary differential equations: an introduction for scientists and engineers*, volume 10. Oxford University Press on Demand, 2007.

[46] FY Zhuang, MRT Yen, YC Fung, and SS Sobin. How many pulmonary alveoli are supplied by a single arteriole and drained by a single venule? *Microvascular research*, 29(1):18–31, 1985.

[47] David A Greenberg and Kunlin Jin. From angiogenesis to neuropathology. *Nature*, 438(7070):954–959, 2005.

[48] Alexander Norup Nielsen and Martin Lauritzen. Coupling and uncoupling of activity-dependent increases of neuronal activity and blood flow in rat somatosensory cortex. *The Journal of physiology*, 533(3):773–785, 2001.

[49] Emmanuelle Chaigneau, Pascale Tiret, Jérôme Lecoq, Mathieu Ducros, Thomas Knöpfel, and Serge Charpak. The relationship between blood flow and neuronal activity in the rodent olfactory bulb. *Journal of Neuroscience*, 27(24):6452–6460, 2007.

[50] Mark A Mintun, Brian N Lundstrom, Abraham Z Snyder, Andrei G Vlassenko, Gordon L Shulman, and Marcus E Raichle. Blood flow and oxygen delivery to human brain during functional activity: theoretical modeling and experimental data. *Proceedings of the National Academy of Sciences*, 98(12):6859–6864, 2001.

[51] Louis Gagnon, Amy F Smith, David A Boas, Anna Devor, Timothy W Secomb, and Sava Sakadžić. Modeling of cerebral oxygen transport based on in vivo microscopic imaging of microvascular network structure, blood flow, and oxygenation. *Frontiers in computational neuroscience*, 10:82, 2016.

[52] Patrick J Drew, Andy Y Shih, and David Kleinfeld. Fluctuating and sensory-induced vasodynamics in rodent cortex extend arteriole capacity. *Proceedings of the National Academy of Sciences*, 108(20):8473–8478, 2011.

[53] Philip O'Herron, Pratik Y Chhatbar, Manuel Levy, Zhiming Shen, Adrien E Schramm, Zhongyang Lu, and Prakash Kara. Neural correlates of single-vessel haemodynamic responses in vivo. *Nature*, 534(7607):378–382, 2016.

[54] Catherine N Hall, Clare Reynell, Bodil Gesslein, Nicola B Hamilton, Anusha Mishra, Brad A Sutherland, Fergus M O'Farrell, Alastair M Buchan, Martin Lauritzen, and David Attwell. Capillary pericytes regulate cerebral blood flow in health and disease. *Nature*, 508(7494):55–60, 2014.

[55] Changsi Cai, Jonas C Fordsmann, Sofie H Jensen, Bodil Gesslein, Micael Lønstrup, Bjørn O Hald, Stefan A Zambach, Birger Brodin, and Martin J Lauritzen. Stimulation-induced increases in cerebral blood flow and local capillary vasoconstriction depend on conducted vascular responses. *Proceedings of the National Academy of Sciences*, 115(25):E5796–E5804, 2018.

[56] Felix J Meigel, Peter Cha, Michael P Brenner, and Karen Alim. Robust increase in supply by vessel dilation in globally coupled microvasculature. *Physical Review Letters*, 123(22):228103, 2019.

[57] Patrick J Drew, Andy Y Shih, Jonathan D Driscoll, Per Magne Knutsen, Pablo Blinder, Dimitrios Davalos, Katerina Akassoglou, Philbert S Tsai, and David Kleinfeld. Chronic optical access through a polished and reinforced thinned skull. *Nature methods*, 7(12):981–984, 2010.

[58] Benyi Xiong, Anan Li, Yang Lou, Shangbin Chen, Ben Long, Jie Peng, Zhongqin Yang, Tonghui Xu, Xiaoquan Yang, Xiangning Li, et al. Precise cerebral vascular atlas in stereotaxic coordinates of whole mouse brain. *Frontiers in neuroanatomy*, 11:128, 2017.

[59] Ricardo Cortez. The method of regularized stokeslets. *SIAM Journal on Scientific Computing*, 23(4):1204–1225, 2001.

[60] Ricardo Cortez, Lisa Fauci, and Alexei Medovikov. The method of regularized stokeslets in three dimensions: analysis, validation, and application to helical swimming. *Physics of Fluids*, 17(3):031504, 2005.

[61] Timothy W Secomb, R Hsu, NB Beamer, and Bruce M Coull. Theoretical simulation of oxygen transport to brain by networks of microvessels: effects of oxygen supply and demand on tissue hypoxia. *Microcirculation*, 7(4):237–247, 2000.

[62] Nozomi Nishimura, Chris B Schaffer, Beth Friedman, Patrick D Lyden, and David Kleinfeld. Penetrating arterioles are a bottleneck in the perfusion of neocortex. *Proceedings of the National Academy of Sciences*, 104(1):365–370, 2007.

[63] Jozien Goense, Yvette Bohraus, and Nikos K Logothetis. fmri at high spatial resolution: implications for bold-models. *Frontiers in computational neuroscience*, 10:66, 2016.

[64] Feilim Mac Gabhann and Shayn M Peirce. Collateral capillary arterialization following arteriolar ligation in murine skeletal muscle. *Microcirculation*, 17(5):333–347, 2010.

[65] Sudeshna A Chatterjee, Emily Fox, Janis J Daly, Dorian Kay Rose, Samuel Wu, Evangelos A Christou, Kelly Hawkins, Dana Otzel, Katie Butera, Jared Skinner, et al. Interpreting prefrontal recruitment during walking after stroke: influence of individual differences in mobility and cognitive function. *Frontiers in Human Neuroscience*, 13:194, 2019.

[66] Melanie D Sweeney, Kassandra Kisler, Axel Montagne, Arthur W Toga, and Berislav V Zlokovic. The role of brain vasculature in neurodegenerative disorders. *Nature neuroscience*, 21(10):1318–1331, 2018.

[67] Arno Villringer, Andreas Them, Ute Lindauer, K Einhäupl, and Ulrich Dirnagl. Capillary perfusion of the rat brain cortex. an in vivo confocal microscopy study. *Circulation research*, 75(1):55–62, 1994.

[68] Antal G Hudetz. Blood flow in the cerebral capillary network: a review emphasizing observations with intravital microscopy. *Microcirculation*, 4(2):233–252, 1997.

[69] Sune N Jespersen and Leif Østergaard. The roles of cerebral blood flow, capillary transit time heterogeneity, and oxygen tension in brain oxygenation and metabolism. *Journal of cerebral blood flow & metabolism*, 32(2):264–277, 2012.

[70] Adrien Lücker, Timothy W Secomb, Bruno Weber, and Patrick Jenny. The relation between capillary transit times and hemoglobin saturation heterogeneity. part 1: theoretical models. *Frontiers in physiology*, 9:420, 2018.

[71] Joseph Fenstermacher, Hiroyuki Nakata, Atsushi Tajima, Shinn-Zong Lin, Tadahiro Otsuka, Virgil Acuff, Ling Wei, and Daniel Bereczki. Functional variations in parenchymal microvascular systems within the brain. *Magnetic resonance in medicine*, 19(2):217–220, 1991.

[72] Mohammad A Yaseen, Vivek J Srinivasan, Sava Sakadžić, Harsha Radhakrishnan, Iwona Gorczynska, Weicheng Wu, James G Fujimoto, and David A Boas. Microvascular oxygen tension and flow measurements in rodent cerebral cortex during baseline conditions and functional activation. *Journal of Cerebral Blood Flow & Metabolism*, 31(4):1051–1063, 2011.

[73] Tomasz Zygmunt, Sean Trzaska, Laura Edelstein, Johnathon Walls, Saathyaki Rajamani, Nicholas Gale, Laura Daroles, Craig Ramírez, Florian Ulrich, and Jesús Torres-Vázquez. 'in parallel'interconnectivity of the dorsal longitudinal anastomotic vessels requires both vegf signaling and circulatory flow. *Journal of cell science*, 125(21):5159–5167, 2012.

[74] Henrik Ronellenfitsch and Eleni Katifori. Global optimization, local adaptation and the role of growth in distribution networks. *arXiv preprint arXiv:1606.00331*, 2016.

[75] Dan Hu, David Cai, and Aaditya V Rangan. Blood vessel adaptation with fluctuations in capillary flow distribution. *PloS one*, 7(9):e45444, 2012.

[76] Axel R Pries, Timothy W Secomb, P Gaehtgens, and JF Gross. Blood flow in microvascular networks. experiments and simulation. *Circulation research*, 67(4):826–834, 1990.

[77] Jay R Hove. In vivo biofluid dynamic imaging in the developing zebrafish. *Birth Defects Research Part C: Embryo Today: Reviews*, 72(3):277–289, 2004.

[78] Elizabeth AV Jones, Ferdinand le Noble, and Anne Eichmann. What determines blood vessel structure? genetic prespecification vs. hemodynamics. *Physiology*, 21(6):388–395, 2006.

[79] David J Acheson. *Elementary fluid dynamics*. Oxford University Press, 1990.

[80] YC Fung and BW Zweifach. Microcirculation: mechanics of blood flow in capillaries. *Annual Review of Fluid Mechanics*, 3(1):189–210, 1971.

[81] TW Secomb, R Hsu, and AR Pries. Motion of red blood cells in a capillary with an endothelial surface layer: effect of flow velocity. *American Journal of Physiology-Heart and Circulatory Physiology*, 281(2):H629–H636, 2001.

[82] Norman Hu, David Sedmera, H Joseph Yost, and Edward B Clark. Structure and function of the developing zebrafish heart. *The Anatomical Record: An Official Publication of the American Association of Anatomists*, 260(2):148–157, 2000.

[83] Axel R Pries and Timothy W Secomb. Blood flow in microvascular networks. In *Microcirculation*, pages 3–36. Elsevier, 2008.

[84] Nicolas Baeyens, Mary Jo Mulligan-Kehoe, Federico Corti, David D Simon, Tyler D Ross, John M Rhodes, Thomas Z Wang, Cecile O Mejean, Michael Simons, Jay Humphrey, et al. Syndecan 4 is required for endothelial alignment in flow and atheroprotective signaling. *Proceedings of the National Academy of Sciences*, 111(48):17308–17313, 2014.

[85] Brant M Weinstein, Alexander F Schier, Salim Abdelilah, Jarema Malicki, Lilliana Solnica-Krezel, Derek L Stemple, DY Stainier, Fried Zwartkruis, Wolfgang Driever, and Mark C Fishman. Hematopoietic mutations in the zebrafish. *Development*, 123(1):303–309, 1996.

[86] Yujia Qi and Marcus Roper. Control of low flow regions in the cortical vasculature determines optimal arterio-venous ratios. *Proceedings of the National Academy of Sciences*, 118(34), 2021.

[87] Jacques L Sherman Jr. Normal arteriovenous anastomoses. *Medicine*, 42(4):247–268, 1963.

[88] Lars Walløe. Arterio-venous anastomoses in the human skin and their role in temperature control. *Temperature*, 3(1):92–103, 2016.

[89] Cheng-chen Huang, Tai-Chuan Wang, Bo-Hung Lin, Yi-Wen Wang, Stephen L Johnson, and John Yu. Collagen ix is required for the integrity of collagen ii fibrils and the regulation of vascular plexus formation in zebrafish caudal fins. *Developmental biology*, 332(2):360–370, 2009.

[90] Kyung In Baek, Shyr-Shea Chang, Chih-Chiang Chang, Mehrdad Roustaei, Yichen Ding, Yixuan Wang, Justin Chen, Ryan O'donnell, Hong Chen, Julianne W Ashby, et al. Vascular injury in the zebrafish tail modulates blood flow and peak wall shear stress to restore embryonic circular network. *Frontiers in Cardiovascular Medicine*, 9, 2022.

[91] Esther Jacob, Meinrad Drexel, Thorsten Schwerte, and Bernd Pelster. Influence of hypoxia and of hypoxemia on the development of cardiac activity in zebrafish larvae. *American Journal of Physiology-Regulatory, Integrative and Comparative Physiology*, 283(4):R911–R917, 2002.

[92] Vincent Doyeux, Thomas Podgorski, Sarah Peponas, Mourad Ismail, and Gwennou Coupier. Spheres in the vicinity of a bifurcation: elucidating the zweifach–fung effect. *Journal of Fluid Mechanics*, 674:359–388, 2011.

[93] Jared O Barber, Jonathan P Alberding, Juan M Restrepo, and Timothy W Secomb. Simulated two-dimensional red blood cell motion, deformation, and partitioning in microvessel bifurcations. *Annals of biomedical engineering*, 36(10):1690–1698, 2008.

[94] Zaiyi Shen, Gwennou Coupier, Badr Kaoui, Benoît Polack, Jens Harting, Chaouqi Misbah, and Thomas Podgorski. Inversion of hematocrit partition at microfluidic bifurcations. *Microvascular research*, 105:40–46, 2016.

[95] Francesco Clavica, Alexandra Homsy, Laure Jeandupeux, and Dominik Obrist. Red blood cell phase separation in symmetric and asymmetric microchannel networks: effect of capillary dilation and inflow velocity. *Scientific Reports*, 6, 2016.

[96] C Pozrikidis. Axisymmetric motion of a file of red blood cells through capillaries. *Physics of fluids*, 17(3):031503, 2005.

[97] Magalie Faivre, Manouk Abkarian, Kimberly Bickraj, and Howard A Stone. Geometrical focusing of cells in a microfluidic device: an approach to separate blood plasma. *Biorheology*, 43(2):147–159, 2006.

[98] Natalie D Mylniczenko, Eric W Curtis, Rachel E Wilborn, and Forrest A Young. Differences in hematocrit of blood samples obtained from two venipuncture sites in sharks. *American journal of veterinary research*, 67(11):1861–1864, 2006.

[99] Kashmiri L Arora et al. Differences in hemoglobin and packed cell volume in blood collected from different sites in japanese quail (coturnix japonica). *International Journal of Poultry Science*, 9(9):828–830, 2010.